NEW ANALYTICAL APPROACHES FOR MASS SPECTROMETRY IMAGING

A Dissertation
Presented to
The Academic Faculty

by

Rachel Bennett Stryffeler

In Partial Fulfillment
of the Requirements for the Degree
Doctor of Philosophy in the
School of Chemistry and Biochemistry

Georgia Institute of Technology
May 2015

NEW ANALYTICAL APPROACHES FOR MASS SPECTROMETRY IMAGING

Approved by:

Dr. Facundo M. Fernández, Advisor
School of Chemistry and Biochemistry
Georgia Institute of Technology

Dr. Christine K. Payne
School of Chemistry and Biochemistry
Georgia Institute of Technology

Dr. Lawrence A. Bottomley
School of Chemistry and Biochemistry
Georgia Institute of Technology

Dr. M. Cameron Sullards
School of Chemistry and Biochemistry
Georgia Institute of Technology

Dr. Hang Lu
School of Chemical and Biomolecular Engineering
Georgia Institute of Technology

Date Approved: March 25, 2015

“A heart that beats an incredible machine,
made of blood and love and hope and lust and steam”
-Jennifer Nettles and Kristian Bush, Sugarland

This dissertation is dedicated to Lynda Jolly Bennett, the woman who inspired this journey and has supported it every step along the way.

ACKNOWLEDGEMENTS

This journey has been one that is defined not only by scientific accomplishment but also the people who contributed to its success. The first of those is Dr. Facundo Fernández, who served as an excellent advisor and mentor throughout this process. I would like to thank you for your patience, encouragement, and drive to help me exceed my own expectations. You are a passionate educator, and I appreciate you making this a highly personalized experience accommodating my individual goals and needs. Under your guidance I have grown personally and professionally, and I am grateful for your support. I would also like to thank my committee members Dr. Lawrence Bottomley, Dr. Hang Lu, Dr. Christine Payne and Dr. M. Cameron Sullards for their advisement and interest in my graduate research.

Another significant scientific mentor who deserves many thanks is Dr. Paul Edmiston at The College of Wooster. You have had a profound impact on my scientific career going back to the General Chemistry classroom dropping text books. You taught me to love scientific research and be truly passionate in my pursuits. I value the relationship we have developed even after I graduated from Wooster; thank you for your continued support and friendship.

I would like to thank the Fernandez lab members that have made the day-to-day experience of doing graduate research more enjoyable. Christina Jones and Joel Keelor, you have been here for this entire journey and I am glad to have shared it with you. Thank you, Martin Paine, for your imaging wisdom, but also for sharing your wild sense of humor. Jose Perez, Martin Paine, Jay Forsythe, Eric Parker, Xiaoling Zang, David Gaul, Matthew

Bernier and Jarrett Davis, you all have been a true joy to work with and excellent office-mates with great personalities and senses of humor. Thank you for the many scientific discussions, providing expertise to guide research and troubleshoot problems. I look forward to many years of continued friendship. I would also like to thank former members of the Fernandez lab – Glenn Harris, Asiri Galhena, Manshui Zhou, Chaminda Gamage, Maria Eugenia Monge, Prahba Dwivedi, and Jennifer Pittman – for their guidance and support especially when I was just beginning my tenure at Georgia Tech. A special thanks goes out to Sue Winters, Arian Padron, Richard Bedell and the other technical support staff in the School of Chemistry and Biochemistry for making sure operations in the lab ran smoothly.

I am grateful for the collaborations I have been a part of during my graduate career. These relationships have helped expose me to a larger spectrum of scientific research and pushed the boundaries of my own. I would like to thank the Center for Chemical Evolution for financial support and giving me the opportunity to take part in highly-interdisciplinary research. As a part of the Center, I would like to thank Christine Conwell for her efforts in creating a cohesive research effort and for her valuable personal and professional support. I would like to thank Dr. Arthur Weber of the SETI Institute for his expertise in prebiotic synthesis that played a critical role in the DetectTLC project. I would also like to thank Chanchala Kaddi for her Matlab expertise and assistance in helping me maximize the value of my datacubes. I would like to thank Dr. Jake Huckaby and Ezequiel Martin for their contributions to the robotics project.

A special thanks goes out to the many friends I have made here at Georgia Tech – Chelsea Wyss, Kim Clarke, Megan Mann, Liz Schiefer, Annie Lesiak, Lauren Austin,

Hailey Bureau, Johanna Smeekens and many others. You ladies have been an excellent group of women and I am lucky to call you my friends. Thank you for the many coffee dates and conversations that took place during those times. I would also like to thank Grace Campbell for her friendship over the last nine years. Your sense of humor, values and perspective have helped to keep me grounded throughout this process. I am grateful for our Sunday afternoon phone calls, and I promise we'll get back on schedule once this dissertation is defended.

This journey would not have been possible without the love and support of my family. I would especially like to thank my parents, Tom and Lynda Bennett for their encouragement throughout this entire process, and often times being more optimistic than I was. You taught me to never give up and instilled in me a set of values I will carry with me forever. Mom, you are proof that a woman can be an excellent scientist and loving mother; thank you for being the role model I have always looked up to. Dad, I am grateful to have inherited your organizational skills. More importantly, when I have had the choice to sit it out or dance, you have helped get me out on the dance floor and give faith a fighting chance. I would also like to thank Daniel, Hannah and Terry Bennett for having the perfect line with perfect timing to put a smile on my face when I needed it most. I am looking forward to a reunion at the Bennett Beach House (and we'll see if whether we invite the parental units). Thank you to the Skowrons and Stryffelers, you have accepted me and loved me as one of your own, and I am lucky to call you my family.

Last, but not least, I would like to express my heartfelt gratitude to my loving husband, Joe. You have been my rock for the past seven years, and I am so incredibly thankful for your support throughout this journey. This has truly been a roller coaster of a

ride, and I would like to thank you for your unconditional love. Thank you for listening when I'm excited that "science worked" and for offering a hug (and glass of wine) when "science didn't work." Having you as a partner in life gives me the confidence to know that together we can do anything, and I look forward to many more wonderful years together. You make me laugh a little louder, love a little harder, and I feel alive when I'm with you…

TABLE OF CONTENTS

LIST OF TABLES

LIST OF FIGURES

LIST OF SCHEMES

LIST OF SYMBOLS

2^3S_1	helium metastable atom excited to the triplet state
α	spray head angle
β	collection angle
C	contrast
d_1	sprayer to surface distance
d_2	inlet to surface distance
d_3	sprayer to inlet distance
d_4	sprayer tip protrusion
Da	dalton
DC	direct current
eV	electron volt
i.d.	inner diameter
I	maximum intensity
I_b	background intensity
λ	wavelength
m/*z*	mass-to-charge ratio
o.d.	outer diameter
psi	pounds per square inch
V_c	compensation voltage
V_{rf}	radio frequency voltage amplitude

LIST OF ABBREVIATIONS

2D	two-dimensional
3D	three-dimensional
4-HBA	4-hydroxybenzoic acid
9-AA	9-aminoacridine
A	area
AICN	aminoimidazolecarbonitrile
AIF	all-ion fragmentation
APCI	atmospheric chemical ionization
APGD	flowing afterglow-pressure glow discharge
AP-MALDI	atmospheric pressure matrix assisted laser desorption ionization
APZ	2-aminopyrazine
Ca	convex area
CCI	controlled cortical impact
CI	chemical ionization
Co	compactness
CPCD	coupled physical and chemical dynamics
CRM	charge residue model
Δm	mass difference
DAFN	diaminofumaronitrile
DAMN	diaminomaleonitrile
DAN	1,5-diaminonapthalene
DART	direct analysis in real time

DC	direct current
DESI	desorption electrospray ionization
DHA	2,5-dihydroxybenzoic acid
DMF	N,N-dimethylformamide
DMS	differential mobility spectrometry
DTIMS	drift tube ion mobility spectrometry
EASI	easy ambient sonic-spray ionization
Ec	eccentricity
EESI	extractive electrospray
EI	electron impact
En	entropy
Er:YAG	erbium-doped yttrium aluminum garnet
ESI	electrospray ionization
Ex	extent
FAIMS	high field asymmetric waveform ion mobility
FAPA	flowing atmospheric pressure afterglow
FWHM	full width at half maximum
GIST	gas-ion-separator
GUI	graphical user interface
HCD	high-energy collision-induced dissociation
He^*	helium metastable atom
HP	high performance
IACUC	Institutional Animal Care and Use Committee
ICP	inductively coupled plasma
IEM	ion evaporation model

IR-LAMICI	infrared laser ablation-metastable-induced chemical ionization
ITO	indium tin oxide
LAESI	laser ablation-electrospray ionization
LC	liquid chromatography
LMIG	liquid metal ion gun
LMJ-SSP	liquid microjunction-surface sampling probe
LMMA	laser microprobe mass analyzer
μXRF	micro x-ray fluorescence
MALDESI	matrix assisted laser desorption electrospray ionization
MeCN	acetonitrile
MeOH	methanol
MS	mass spectrometry
MSI	mass spectrometry imaging
Nano-DESI	nanospray desorption electrospray ionization
Nano-ESI	nanospray electrospray ionization
Nd:YAG	neodymium-doped yttrium aluminum garnet
NH_4Form	ammonium formate
NMF	non-negative matrix factorization
OCN	oscillating capillary nebulizer
OCT	optimal cutting temperature polymer
PC	phosphatidylcholine
PCA	principle component analysis
PCL	point cloud library
PE	phosphatidylethanolamine
PESI	probe electrospray ionization

PI	phosphatidylinositol
PS	phosphatidylserine
PzNA	pyrazine nucleic acid
PZO	pyrazine-2-one
Q-TOF	quadrupole-time of flight
Re	number of connected regions
RF	radio frequency
ROI	region of interest
RoPPI	robotic plasma probe ionization
ROS	robot operating system
S	solidity
S/N	signal-to-noise ratio
SIMS	secondary ion mass spectrometry
ST	sulfatide
TBI	traumatic brain injury
TLC	thin layer chromatography sprayer
TOF	time of flight
TWIMS	traveling wave ion mobility spectrometry
UPLC	ultra-high performance liquid chromatography
XRD	x-ray diffraction

SUMMARY

Chemical imaging by mass spectrometry is a powerful approach by which to map spatial distributions of molecules to better understand their function in the system of interest. Over the last thirty years, mass spectrometry imaging (MSI) has evolved into a very powerful analytical tool for the investigation of chemically-complex samples including biological tissues, catalytic surfaces and thin layer chromatography plates, among many others. The work in this dissertation aimed to characterize existing MSI methods, while also developing novel instrumentation able to overcome the challenges found in a variety of applications. These contributions to the field of MSI have significant potential as they enable untargeted and targeted modes of imaging, greater flexibility in the type of sample that may be analyzed and automated screening for more complete and efficient interpretation of datasets.

Advances in instrumentation have made mass spectrometry imaging a very diverse field with a variety of ionization methods capable of direct surface sampling. These techniques vary in their spatial resolution, chemical information and ease of use. A history and state of the art in MSI research is presented in Chapter 1. Various methods currently in practice are introduced along with their figures of merit, reported applications, and practical experimental considerations.

The respective advantages and disadvantages of each MSI technique makes them suitable for unique specialized applications. Chapter 2 presents the first direct and unbiased comparison between desorption electrospray ionization (DESI) and matrix assisted laser desorption ionization (MALDI) of lipids in brain tissues, specifically related to traumatic

brain injury models. These techniques and their related experimental protocols were investigated to maximize chemical coverage in a quasi-targeted study of lipid species. Tissue washing can reduce spectral complexity and increase sensitivity by up to four fold, and DESI and MALDI were found to be complimentary to each other with respect to lipid detection.

While the direct analysis of a surface by MSI is highly desirable, the lack of chemical separation can result in ion suppression, loss in sensitivity and limit the ability to confidently identify analytes detected. Chapter 3 reports the incorporation of a nested separation within a DESI-MSI system to overcome sensitivity and selectivity challenges in MSI. In this work, DESI DM-MSI experiments on biological tissue samples such as sea algae and rat brain tissue sections were conducted using fixed DMS compensation voltages that selectively transferred one or a class of targeted compounds. By reducing chemical noise, the signal-to-noise ratio was improved tenfold as well as doubling the image contrast, effectively increasing image quality. This was the first report of incorporation of DM filtering to MSI.

Existing MSI techniques are restricted to the imaging of flat surfaces, dictated by strict source geometry and in some cases by vacuum restrictions. Chapters 4-5 present the development imaging capabilities for bulky and irregular samples. Chapter 4 employs DESI-MSI to investigate mineral-catalyzed surface reactions on large, but flat, granite samples demonstrating the ability to apply DESI to porous surfaces. Direct investigation of reactive mineral surfaces by DESI-MSI gives a new perspective on the important role of the mineral surface in the formation of reaction products in the model prebiotic reaction of the thermal decomposition of formamide. Whereas Chapter 5 presents an entirely novel

approach to three-dimensional surface imaging of irregular samples named Robotic Plasma Probe Ionization (RoPPI). By coupling robotic sampling with MSI, irregular surfaces may be imaged directly without altering the native state of the sample; i.e. the sample does not need to be made planar for imaging purposes. The current RoPPI system enables surface imaging with spatial resolution of 1 mm, and future plans aim to improve the resolution such that it is more competitive in the field.

Finally, MSI experiments produce a vast amount of data and extraction of meaningful chemical information is thus crucial in maximizing its value. Chapter 6 presents an example of software development that facilitates the automated screening of large MSI datasets produced from imaging of thin layer chromatography (TLC) separations with many unique components. The program, DetectTLC, automatically screens MSI datasets for spot-like ion images that would correspond to reaction components separated on a TLC plate. When combined with high mass accuracy and multi-modal fragmentation data acquisition, DetectTLC also automates the analyte identification process. Given the large datasets generated during a MSI experiment, this software reduces data processing times from days to minutes and facilitates comprehensive identification of reaction mixture components that might not otherwise be detected manually. Employing desorption electrospray ionization mass spectrometry (DESI-MS) as the ambient sampling method in conjunction with DetectTLC, we were able to identify and characterize previously unknown products of an abiotic pyrazine nucleic acid synthesis products. This nucleic acid synthesis is of great interest to prebiotic chemists and the origin of life community but the DetectTLC software package is also expected to be extremely useful for any application that benefits from fast TLC separations or for reaction monitoring purposes.

CHAPTER 1. INTRODUCTION TO MASS SPECTROMETRY IMAGING

1.1 Abstract

Chemical imaging by mass spectrometry is a powerful approach by which to map spatial distributions of molecules to better understand their function and alterations in the environment of interest. Mass spectrometry imaging (MSI) can be used for untargeted analysis without the need for chemical labeling and facilitates the acquisition of chemical information for discovery and hypothesis-generating applications. Additionally, targeted imaging of a known analyte of class of analytes can facilitate increased sensitivity and selectivity through the development of specific methods. Several ionization techniques capable of localized surface analysis may be used in an imaging modality; common ionization techniques used in MSI include secondary ion mass spectrometry (SIMS), matrix assisted laser desorption ionization (MALDI) and desorption electrospray ionization (DESI), among others. Each offers unique strengths and weaknesses, with the appropriate method being selected based on desired (1) operating conditions, (2) diversity of chemical information, (3) spatial resolution, and (4) sensitivity. Advances in the field of MSI have significantly improved its practical value and made it widely applicable to the study of microelectronics, biological tissues, reactive surfaces, and as a general surface characterization tool. This chapter presents an introduction to MSI, including the evolution of the field, emphasizing principles of operation that most directly affect image quality.

1.2 Basic Principles of Mass Spectrometry Imaging

Analytical imaging techniques capture snapshots of chemical and/or physical properties of materials creating a deeper understanding of the system and how it interacts with its surroundings. Mass spectrometry (MS) is an example of an analytical tool capable of imaging samples in a comprehensive and chemically specific way. Although MS is not

generally thought of as a spatially-resolved technique, advances in the field over the last thirty years have not only made this possible, but also a very powerful analytical tool. The combination of untargeted molecular mass analysis and spatial information afforded by mass spectrometry imaging (MSI) makes the technique invaluable for the investigation of chemically-complex samples.

In its most simple form, a mass spectrometer is comprised of three primary modular components: the ion source, the mass analyzer, and the detector. Traditionally, all three of these components have required vacuum conditions for operation, including the ion source. Early ion sources used for routine bulk mass analysis such as electron impact (EI) and chemical ionization (CI) operate in vacuo to ionize volatile analytes already in the gas phase. To transform mass spectrometry into a spatially-resolved analytical technique, the instrumentation had to be adapted for localized desorption of analytes directly from the sample. This is done using a primary beam in the form of an ion beam, laser pulse or liquid jet that impacts the sample surface generating a secondary plume of ions, neutrals and molecular clusters. Alternatively, a combination of techniques may be used for distinct desorption and ionization events for mass spectral detection. Recent advances in the field have not only enabled this process to take place under vacuum conditions, but also at atmospheric pressure open to the ambient surrounding. As mass spectrometry is only capable of detecting ionized molecules, the choice of desorption/ionization process is crucial for the quality of chemical information attainable. To generate a chemical image by any of these approaches, the primary beam is rastered across the sample surface while continually acquiring mass spectral data and correlating it to the spatial information (Figure 1.1). This technique is known as "microprobe" mode MSI, and is the mostly widely used approach in the field. Under these operating conditions, the selection of primary desorption beam (Figure 1.1a) also affects the spatial resolution based on the ability to focus the beam. As the beam is focused to a smaller impact spot area, chemical information may be acquired in smaller pixels.

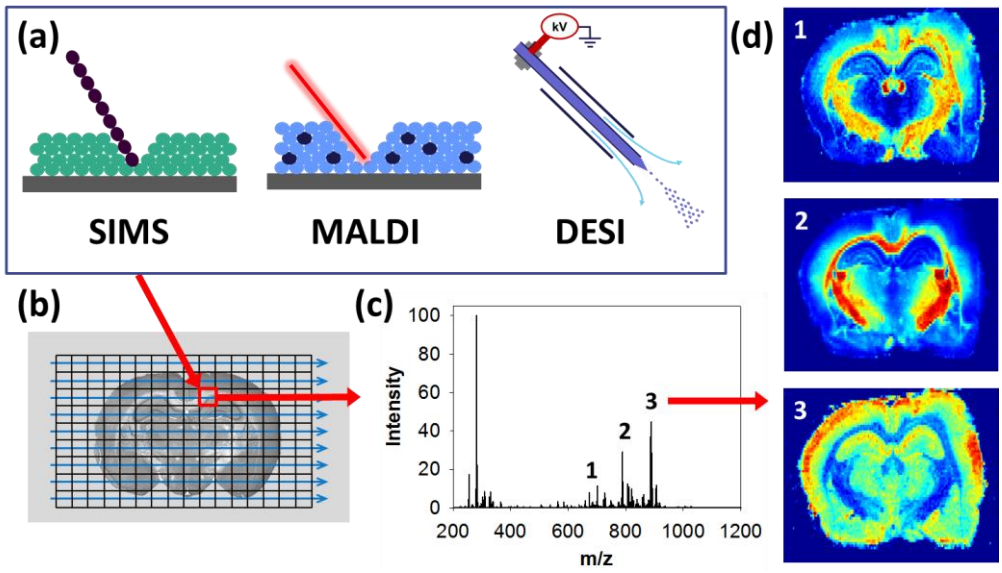

Figure 1.1. Common ion sources used for MSI, including SIMS, MALDI and DESI (a) that are rastered across the sample surface in uni-directional line scans (b) generating mass spectra that correspond to specific X-Y coordinates (c). Ion abundances are then mapped across the sampled area generating chemical images corresponding to select analytes (d).

Imaging by mass spectrometry was first reported in 1962 by Castaing and Slodzian using secondary ion mass spectrometry (SIMS) in a configuration with an electrostatic collection system that mimicked the lens in a light microscope.[1] This gave rise to the field of ion microscopy, still dominated by SIMS instrumentation through the 1990s until softer ionization sources became more widespread for intact molecular imaging. Generally, instrumentation advances in MSI have focused on improving the following elements of analysis: (a) observable chemical diversity, (b) spatial resolution and image contrast, (c) sensitivity, (d) minimized sample alteration, and (e) data interpretation. The Holy Grail of MSI techniques would have all five parameters optimized, but improvements in one aspect generally come at the cost of another. For example, as the spatial resolution is increased (i.e. smaller area sampled by primary beam) the absolute amount of sample available for ionization is reduced, resulting in poorer signal to noise and detection challenges. However,

key advances in instrumentation have significantly improved the capabilities and wealth of information attainable via MSI, as described below.

1.3 Origins of Mass Spectrometry Imaging: Secondary Ion Mass Spectrometry

Secondary ion mass spectrometry was among the first ionization methods that enabled the mass analysis of nonvolatile and thermally labile analytes directly from sample surfaces. In SIMS, a primary ion beam usually composed on Ga^+, Cs^+, Ar^+ with energies in the 5-25 keV range bombards the sample surface. These primary ions deposit energy into the surface layers resulting in a collision cascade that ultimately ejects material from the sample, a process known as "sputtering". The majority of the sputtered material are neutral molecules or fragments, but approximately 1% are charged particles – the secondary ions – that undergo mass analysis and detection. The high energy deposited by the primary ion beam can cause severe molecular fragmentation, limiting detection to elemental and low molecular weight analytes (< 1000 Da, depending on primary beam composition and energy).

Early imaging experiments used an ion-optical collection system analogous to the lens of an optical microscope to preserve the spatial distributions of the ions from a single bombardment.[1] In this early configuration, spatial resolution was on the order of tens of microns. Alternatively, the primary ion beam may be also rastered across the surface in microprobe mode resulting in improved spatial resolution on the order of 50 nm, limited by the focus of the primary beam rather than the detector properties.[2-3] By scanning the primary beam (or rastering the sample beneath the primary beam) limitations in ion optics are reduced, also allowing for mass analyzers such as a time-of-flight (TOF) to be incorporated for larger mass ranges and spectral resolution.[4]

To date, imaging SIMS provides the highest spatial resolution of all MSI techniques, with typical operating spatial resolution ranging from 50 nm – 10 μm depending on the primary ion beam used.[5-6] The Ga^+ liquid metal ion gun (LMIG)

currently proved the highest spatial resolution with a probe size < 10 nm, but it yields little molecular information.[5] TOF-SIMS still suffers several drawbacks, the most significant of which is the considerable analyte fragmentation that occurs during the harsh impact of the primary ion beam. To overcome this weakness, Benninghoven developed the static SIMS method in which the primary ion dose is kept below certain limits ($<10^{13}$ ions cm^{-2})[7] to facilitate detection of intact elemental and molecular species.[8] However, his early static SIMS experiments using an Ar^+ primary ion beam, 2.5 – 5 kV, ~10^{-9} A cm^{-2}, still only detected analytes up to m/z ~ 300 including aminobenzoic acid ($[M + Ag]^+$, m/z 244),[9] several amino acids (i.e. cysteine, m/z 241),[10] and drugs (i.e. atropine, m/z 290).[11] Further advances in the form of cluster ion sources (i.e. C_{60}^+, Bi_3^+, Au_3^+, and SF_5^+) have enabled the successful imaging of larger molecules, including lipids in biological tissues by TOF-SIMS, but detection is generally limited to species of up to ~1000 Da.[6, 12] The use of cluster ion sources also limits spatial resolution due to restricted beam focusing, but still allows for imaging on the low micron (<10 μm) scale.

The high spatial resolution afforded by TOF-SIMS makes the technique amenable to a variety of applications, especially microelectronics,[13] self-assembled monolayers[14] and the study of materials where surface features are in the nanometer range.[15-16] The technique is also growing in popularity for the study of biological samples at the cellular and subcellular level.[17-19]

1.4 Matrix Assisted Laser Desorption Ionization

Instead of using highly-energetic ions as the primary beam, a laser beam may also be used for analyte desorption and ionization as in laser microprobe mass analyzer (LMMA),[20] a technique designed specifically with biological tissue imaging in mind. The addition of energy-absorbing matrix molecules, usually a small organic acid as in matrix assisted laser desorption ionization (MALDI)[21], further softens the desorption process enabling the analysis of large intact biological molecules. Hillenkamp and Karas were the

first to coin the term MALDI and show that embedding the analytes in a matrix led to better ionization.[21] However, the first report of using MALDI in the analysis of large biomolecules (~100,000 Da) was by Tanaka in 1988[22] earning him the Nobel Prize in 2002. The strength of MALDI in the analysis of biological samples was further demonstrated with the direct imaging of biological tissues by Caprioli in 1997.[23] Under routine operating conditions, typical spatial resolution attainable in a MALDI-MSI experiment is on the order of ~100 μm. This spatial resolution together with the ability to ionize many biological molecules including lipids, peptides and intact proteins make MALDI an ideal tool for imaging of biological tissues.[7]

In regular MALDI analysis, the matrix is combined with the sample and serves to absorb the majority of the laser energy upon irradiation (Figure 1.2). In MALDI-MSI, where a solid sample is present, the analytes must be extracted from the surface into the matrix in situ for the formation of matrix-analyte crystals.[24] The sample is then irradiated with an ultraviolet (UV) or infrared (IR) laser pulse under vacuum conditions (~10^{-6} torr) resulting in a phase explosion and desorption of analyte and matrix clusters with minimal fragmentation.[25-26] Ions are not generated below a threshold laser fluence, which depends on the matrix used as well as the analyte-matrix ratio; at this threshold, a sharp onset of desorption/ionization occurs.[27] Ions generated in the desorption plume are extracted by a potential difference between the sample plate and an extraction grid after which they are focused by ion optics for mass analysis and detection. Similar to SIMS, the pulsed nature of the laser used in MALDI makes TOF mass analysis an ideal pairing. A successful MALDI experiment depends on a number of parameters that must be optimized for target analytes and sensitivity. Many extensive reviews have been published on fundamental principles related to MALDI analysis,[26, 28-29] but this overview will focus on the variables that most directly influence MSI capabilities.

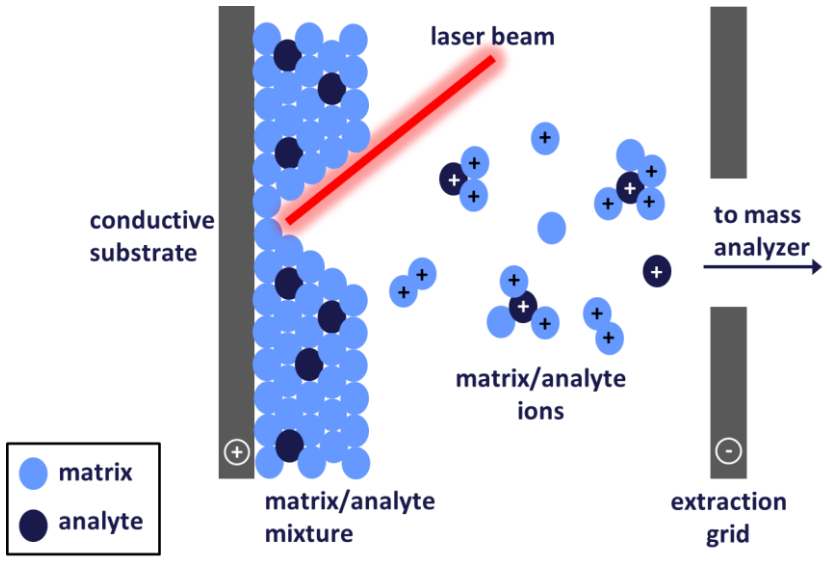

Figure 1.2. Schematic of MALDI desorption and ionization region.

1.4.1 Matrix Selection: Desorption and Ionization

An effective MALDI matrix must be capable of strongly absorbing the energy from the laser pulse to promote desorption and subsequent ionization. State of the art lasers used for MALDI include nitrogen (N_2, 337 nm) and neodymium-doped yttrium aluminum garnet (Nd:YAG, 355 nm) for UV irradiation. Carbon dioxide (CO_2, 10.6 μm) and erbium-doped yttrium aluminum garnet (Er:YAG, 2.94 μm) have been implemented for IR irradiation, but are less common due to lower matrix absorption.[28] To maximize absorption of these laser energies, MALDI matrices are generally derivatives of benzoic or cinnamic acid or other aromatic acids that strongly absorb in the UV region.[28] After laser absorption, the majority of excess energy is converted to heat. However, if the matrix is unable to dissipate this heat quickly enough, thermal confinement causes a "phase explosion" leading to ejection of matrix and analyte from the surface.[26] Table 1.1 includes examples of commonly used MALDI matrices and their optimal analytes. Recent developments in matrix chemistry have also shown solid/liquid ionic matrices to be effective for imaging,

and have resulted in increases sensitivity for select analytes, but these matrices are not as widely used.[30]

Table 1.1. Commonly-used MALDI matrices

Structure	Name	Exact Mass	Laser λ (nm)	Application
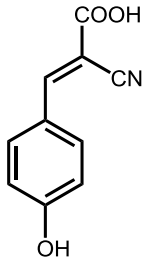	α-cyano-4-hydroxyl-cinnamic acid	189.0426	266, 355, 337	peptides, lipids
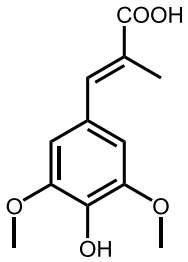	sinnapic acid	238.0841	266, 355, 337, 2.94 μm, 2.79 μm, 10.6 μm	proteins
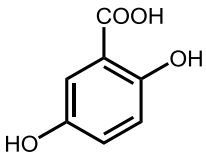	2,5 dihydroxy-benzoic acid	154.0266	266, 355, 337, 2.94 μm, 2.79 μm, 10.6 μm	lipids
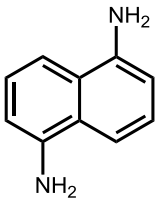	1,5-diaminonapthalene	158.0844	330-360	lipids

Subsequent analyte ionization cannot be explained by a single mechanism due to the variety of ionized species detected, but the processes in MALDI ionization may be summarized by two models: the cluster or "lucky survivor" model,[31] and the coupled

physical and chemical dynamics (CPCD, also known as gas phase protonation or excited-state proton transfer)[32-34] model. In the lucky survivor model, analytes are believed to retain their initial charges when crystallized with the matrix.[31] Upon laser irradiation, desorbed clusters break up and some analyte ions are neutralized by counterions. Analyte ions that retain their charge, typically singly charged, are considered the lucky survivors and detected by mass spectrometry. In this model, the matrix plays the most crucial role in the desorption process, and therefore it is selected based primarily on its ability to absorb the laser energy upon irradiation. The lucky survivor model more accurately describes liquid samples in which analyte ions are more easily solvated rather than in solid samples in their original state. In contrast, the CPCD model proposes that neutral analyte molecules are ejected in the desorption plume. Photoionization and subsequent intermolecular matrix reactions within the plume result in protonated and deprotonated matrix ions that go on to ionize analyte molecules via proton transfer, cationization or electron capture.[35] In this model, because the matrix is directly involved in the ionization process, chemical properties of the matrix such as its ionization energy, proton affinity and electron affinity must be considered with respect to the analyte in order for the analyte to be successfully ionized. For example, if the proton affinity of the matrix is higher than that of the analyte, the matrix will retain the proton making it nearly impossible to ionize the analyte of interest. This results in low sensitivity, but also high chemical background in the spectra corresponding to matrix ions in the low mass region. In both models the matrix plays a crucial role in desorption and ionization processes, respectively, and must be selected with the target analyte in mind. It is also important to note that because the laser irradiation is neutral, both positive and negative ions may be formed during desorption and ionization process. However the voltages applied to the sample plate and extraction gird dictate which ions are transmitted to the mass analyzer for separation and detection.

An additional challenge related to matrix selection posed by imaging experiments is the time required to conduct such an experiment, often taking upwards of several hours

to conduct. Therefore, when conducting a MALDI-MSI experiment the user must also be careful in selecting a matrix that will not degrade or sublime under the high vacuum conditions of the sample chamber over the course of analysis. For example, dihydroxyacetophenone (DHA), a matrix used in MALDI analysis of ceramides and gangliosides, presents challenges in imaging studies of brain tissue of those analytes due to the rapid rate of sublimation under vacuum.[36]

1.4.2 Matrix Application for Imaging

Effective ionization depends on the co-crystallization of the matrix with the analyte, and therefore the way in which they are mixed is crucial for mass spectral analysis and imaging. In imaging, samples are in the solid state and the matrix deposition method must be able to extract analytes from their native environment up into the matrix crystal layer. Organic solvents are often used to assist in this two-phase extraction, but the deposition method must ensure localized mixing in such a way that it does not disturb original spatial distributions of analytes. If the matrix is too dry when it reaches the sample there is little opportunity for extraction, but if it is too wet or humid a thin film will form leading to surface diffusion.[24]

The matrix deposition must also be homogeneous and reproducible across the entire sample, and between different samples, because interpretation of MSI data relies on the comparison of a species' relative abundance with respect to spatial distribution. Variations in matrix concentration on the surface can lead to variations in desorption and ionization efficiency and effective abundance.[37] Uniform, small crystal formation is ideal for imaging as crystal size also plays a role in maximum spatial resolution attainable. Larger matrix crystals have been shown to provide higher signal-to-noise ratios, but it means that the diffusion of analytes into such crystals limits the effective resolution in MALDI-MSI. To balance sensitivity and resolution, MALDI imaging experiments are typically conducted with a laser spot size ≥ 25 μm with matrix crystals equal or smaller in size.[38]

In traditional MALDI, a bulk liquid sample is combined with an excess of matrix in a mutually compatible organic solvent, then deposited on the MALDI sample plate in what is known as the "dried droplet" method.[7] However, this method is impractical for imaging applications as it does not meet the requirements mentioned above – excess solvent leads to lateral analyte diffusion and uneven crystalization. Common solvent-based matrix deposition methods employ pneumatic nebulization (i.e. airbursh or thin layer chromatography (TLC) sprayer)[24] or oscillating capillary nebulizer (OCN)[39] that produce small matrix droplets for localized extraction and rapid solvent evaporation. By controlling the configuration of these devices, the solvent content in the matrix droplets as well as their size may be finely controlled to reduce analyte migration and enhance co-crystallization. When used manually, matrix application by pneumatic nebulization or OCN results in uneven and irreproducible coating, but continuous and automated motion of the sample under the spray has been shown to produce evenly distributed and small (0.5-20 μm) crystals.[39] These crystal sizes compare well with typical laser beam focus diameters and spatial resolution under typical MALDI-MSI operating conditions.

Conversely, dry matrix deposition by subliming the matrix under low pressure and high temperature then condensing it onto the sample has been shown to provide in homogeneous coating for imaging applications.[40] Matrix deposition by sublimation presents two key benefits: (1) elimination of analyte diffusion because no solvent is used and (2) enhanced purity of matrix applied to the sample.[24] Although small volumes of organic solvent may be mixed with the matrix during sublimation to assist in the extraction of analytes into the matrix crystals, it is not necessary.[7, 41] The conditions under which a particular molecule undergoes the solid-gas phase transition in sublimation is an inherent property of that molecule and, in a process similar to distillation, can also serve to purify the sample or matrix in this case.[40] Because the presence of salts and other contaminants can interfere with crystal formation, the enhanced purity of the matrix deposited results in formation of smaller crystals.[42]

1.4.3 MALDI Instrumentation for Imaging

During a MALDI-MSI experiment, the surface of the matrix-covered sample is rastered underneath the focused laser beam. The ability to focus the laser beam as well as the maximum repetition rates of the laser significantly affect the practicality of conducting an imaging experiment.

Because matrix crystals are typically formed in the low micron to nanometer size, the limiting factor for spatial resolution in MALDI-MSI is the ability to focus the laser beam to a small spot size. However, as the spot size is decreased, the amount of sample being desorbed also decreases, thus a loss in signal-to-noise is observed. In an effort to overcome sensitivity challenges, higher laser fluence may be applied, but this often leads to analyte fragmentation.[26] Therefore, typical laser spot sizes used in MALDI-MSI range from 20-100 μm in diameter, but advances in instrumentation have shown spot sizes down to 7 μm[43] and even sub-micron[44] sizes as being possible.[45]

Alternative means of improving effective spatial resolution in MALDI-MSI datasets includes a technique known as "oversampling".[46] In this approach, the sample is stepped a distance smaller than the spot size of the laser beam when it is rastered. Snel and Fuller demonstrated effective spatial resolution of ~15 μm using a laser beam ~150 μm in diameter for the imaging of glucosylceramides in Gaucher disease model tissues.[47] Microscope mode MSI using MALDI has also been shown to deliver pixels down to 600 nm in size using a 200 μm laser spot,[48-49] but limitations in detection speed and spectral resolution limit the practicality of this approach.[45]

As the spatial resolution of a MSI method increases, so does the number of spots probed, which also increases the analysis time and data size. Commercially available N_2 and Nd:YAG lasers are capable of operating with repetition rates of 200 – 1000 Hz with typical pulse lengths of 3 ns or less.[38] Under these conditions, with raster steps of ~100 μm, imaging of a coronal mouse brain section by MALDI-MSI takes on the order of three hours.

1.5 Desorption Electrospray Ionization Mass Spectrometry Imaging

Ionization techniques such SIMS and MALDI enabled imaging mass analysis, but are still limited by the demand for vacuum conditions for ionization. An ionization approach capable of operating at atmospheric pressure opens the door to flexible interfacing of a variety of analytical methods with mass spectrometry including liquid separations and direct surface sampling with reduced sample preparation. With the development of the soft, liquid-based ESI, and later sparked by the appearance of DESI, the field of ambient ionization for rapid and surface analysis has taken off. Of these ambient techniques those capable of localized, direct surface sampling have quickly become popular for MSI experiments because they allow for imaging under conditions that more closely resemble the sample's native state. As the pioneer in ambient mass spectrometry and with many years of refinement, DESI is by far the most popular ambient technique for mass spectrometry imaging.

1.5.1 Electrospray Ionization

Driven by the need to study high-molecular weight species and couple liquid chromatography (LC), ESI was first presented by Dole in 1968 for the analysis of synthetic polymers.[50] Though it wasn't until 1974 when LC was coupled to mass spectrometry via atmospheric pressure chemical ionization (APCI) by Horning et al.,[51] and then by ESI as reported by Whitehouse and coworkers in 1985.[52] The major breakthrough that enabled widespread application of atmospheric pressure ionization with ESI was when Fenn and coworkers successfully ionized large biomolecules with molecular weights up to 130,000 in 1989 (detected as multiply charged ions at m/z ~1500).[53]

Electrospray ionization is a soft ionization technique that operates at atmospheric pressure and effectively transfers solution-phase analytes into the gas phase as intact ions for mass spectral detection. ESI is characterized as a soft ionization mechanism based on

internal energies of ions generated which range from 1.79-1.9 eV,[54] compared to those in MALDI which range from 3-5 eV depending on matrix and laser fluence,[55] and even higher energies in SIMS. This allows for ionization of large molecules with little or no fragmentation. Sample solutions are prepared by dissolving low concentration (~10^{-6} – 10^{-4} M) of analyte in a volatile polar organic solvent such as methanol or acetonitrile (or in aqueous mixtures) with a small amount of weak organic acid (i.e. formic, acetic acid, etc). The sample may also be in the form of the eluent from a LC separation continuously flowing through the ESI source. In conventional ESI, the analyte solution is infused through a narrow (inner diameter ~ 10 μm) metal capillary that has a potential of 0-5 kV applied. The inlet of the mass spectrometer serves as the counter electrode creating a high electric field near the tip of the capillary. Charge separation is induced in the solution, resulting in a charge build up at the tip of the capillary forming a Taylor cone and forcible ejection of charged droplets.[56] A concurrent (or countercurrent in the apparatus used by Yamashita and Fenn)[57] flow of N_2 evaporates solvent from the droplets until the Rayleigh limit is reached and Coulombic explosions yield smaller microdroplets.[56] This cascade continues until droplets reach a size from which desolvated ions may be generated via two primary mechanisms: (1) ion evaporation model (IEM), or (2) charge residue model (CRM).[58]

Iribarne and Thomsom did not use electrospray to produce small droplets, but were the first to propose the ion evaporation model of formation of gas-phase ions from charged droplets.[59-60] Under the ion evaporation model, when the repulsive forces on the droplet are high enough to overcome surface tension, species that started out as solution-phase ions are ejected directly into the gas phase.[60] This model most accurately describes the ionization of small molecules or pre-charged ions. The charge residue model, on the other hand, more accurately describes the ionization of large globular species, such as folded proteins. In this model, the solvent shell evaporates, and the charge remains in the droplet until complete evaporation takes place leaving the analyte carrying the charge as a gas-

phase ion. Under these dynamics, it is possible, and especially common for proteins, to generate multiply-charged analyte ions by ESI. Protonated and deprotonated ions are very common in positive and negative mode ESI, respectively, but the presence of salts makes the formation of adducts (i.e. NH_4^+, Na^+, K^+, CH_3COO^-, etc.) very common as well. Regardless of precise ionization mechanism, it is undeniable that the solvent and chemistry present in the droplets plays a key role in the resulting ionic species.

Effective generation of gas-phase analyte ions depends heavily on the size of droplets generated and their ability to become desolvated. One approach to aide in desolvation was first introduced by Henion and coworkers who implemented a coaxial flow of inert gas (N_2) around the spray capillary to nebulize the liquid stream.[61] This pneumatically-assisted ESI has become the most widely used configuration for electrospray because it can tolerate higher liquid flow rates and water content and still generate smaller droplets from the spray. Additionally, smaller droplets have been shown to have higher ionization efficiency because fewer coulombic explosions are required to generate gas phase ions. Miniaturization of the ESI to narrower capillaries on the order of 1 μm using flow rates on the order of nL min^{-1} produces smaller microdropets in what is known as nanoelectrospray.[62] Not only does nanoelectrospray reduce droplet size, thus increasing sensitivity, it offers the practical advantage of low sample consumption for long analysis time or small sample volumes.

1.5.2 Emergence of Ambient Ionization Mass Spectrometry

Techniques such as ESI and APCI opened the door to ion formation from liquid samples at atmospheric pressures and made a significant step towards analyzing samples in their native states. The field of ambient ionization MS has significantly advanced analytical chemistry capabilities starting with the introduction of desorption electrospray ionization (DESI)[63] in 2004 and direct analysis in real time (DART)[64] in 2005. These and other ambient ionization techniques allow for in situ analysis of samples and surfaces in

the open air with little or no sample preparation while still maintaining high-throughput analysis for an wide range of potential applications.

The large number of unique ambient ionization techniques[65-67] makes it difficult to categorize all methods in a simple manner, but the majority can be broadly classified into two categories based on desorption/ionization mechanisms: (1) spray and solid-liquid extraction-based techniques that generally involve ESI-like ionization and (2) plasma-based techniques that involve gas-phase chemical ionization mechanisms. Multimodal sources combining elements from both of these classes and the coupling of laser desorption/ablation methods to either set-up has generated an even greater number of techniques for ambient ionization. To be considered an ambient ionization technique, it should operate in the open air or ambient environment without an enclosure like those typically found in ESI, APCI or atmospheric pressure-MALDI (AP-MALDI) sources. Furthermore, the ambient ionization technique should allow for direct ionization with minimum sample pre-treatment such as chromatographic separation, etc.

Some examples of the liquid-based desorption/ionization techniques include DESI and easy ambient sonic-spray ionization (EASI),[68] and the liquid microjunction-surface sampling probe (LMJ-SSP),[69] among others. In these type of ambient ionization, a solvent flow is directed at a surface to extract and desorb analytes into a secondary flow of solvent or droplets that undergo ESI-like ionization processes.[56] Plasma-based techniques include, but are not limited to flowing atmospheric pressure afterglow (FAPA; first reported as flowing afterglow-atmospheric pressure glow discharge, APGD),[70-71] DART,[64] and microplasmas.[72] These specific techniques employ plasma ionization sources often in conjunction with a heated gas flow for thermal desorption. One example of a two-step desorption/ionization technique used for surface sampling is laser ablation-ESI (LAESI),[73] but laser ablation coupled to plasma ionization is also becoming more widespread.[74-75]

Rapid growth in the field has led to many one-of-a-kind ambient ionization techniques defined by desorption and ionization mechanisms resulting in an “alphabet

soup" of acronyms.[65-67] Each of these techniques offers specific analytical advantages and disadvantages, but this introduction will focus on the most common techniques used for localized surface sampling and mass spectrometry imaging.

1.5.3 DESI: Principles of Operation

Since it was first reported in 2004,[63] there have been over 700 publications related to DESI, one third of which have been related to imaging. DESI has become a widespread ambient ionization technique and has been applied to the analysis of explosives,[76] forensics,[77] pharmaceuticals,[78-79] biological tissues[80-87] and MSI,[88-89] among many others.[90] In DESI, a pneumatically-assisted charged solvent spray, similar to that used in ESI, is directed at the sample surface to desorb and ionize analytes. In contrast to ESI, the sample is not dissolved in the solution passing through the ion source, rather is present on the sampling surface. The general instrumental design of DESI is shown in Figure 1.3 along with configuration variables.

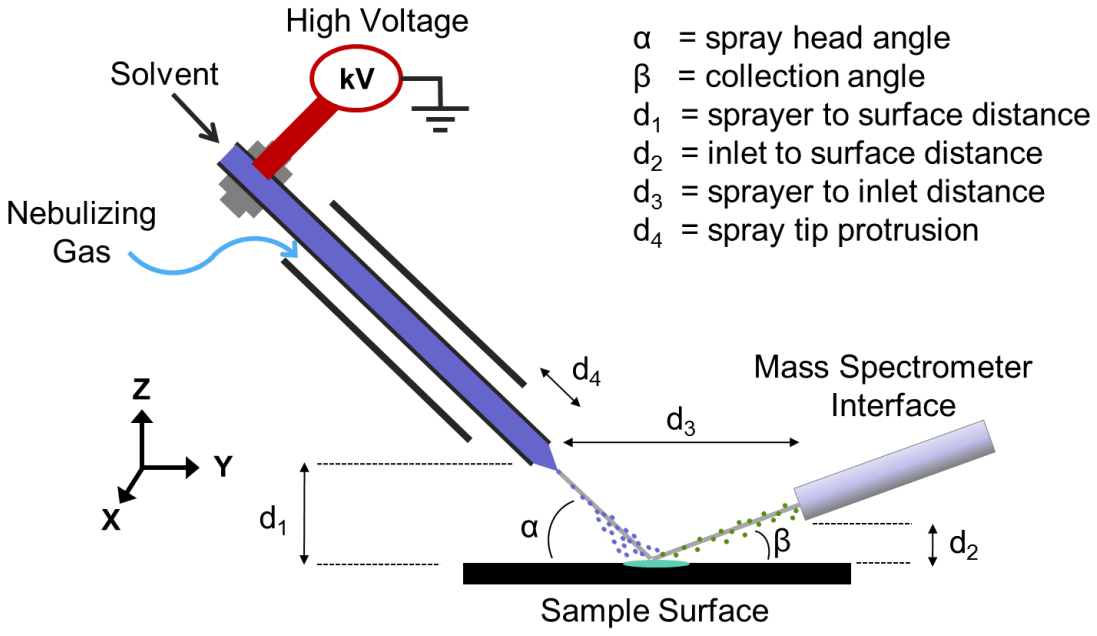

Figure 1.3. Schematic of DESI-MS set-up showing key source-sample-inlet geometry variables that affect both sensitivity and spatial resolution.

Early mechanistic studies proposed that ionization in DESI took place via chemical sputtering, shockwave models or evaporation and gas-phase ionization.[90] However, over time these models have become less likely and the working model for desorption and subsequent ionization by DESI is known as the "droplet pick-up" model.[91] The analysis process begins with the formation of charged primary solvent droplets by the DESI source propelled towards the surface with a high-pressure gas. The droplets emitted from the source are ~2-4 μm in diameter and initially have very high velocities, but this speed can vary greatly.[91] The collision of these droplets with the surface results in the wetting of the surface and a thin film is formed in which the analyte is dissolved by a solid-liquid microextraction mechanism. Evidence for surface wetting is seen in the form of a "solvation delay" of several seconds between switching on the DESI source and observing a sharp increase in ion intensities; this delay corresponds to the time necessary to wet the surface for effective analyte extraction.[92]

Subsequent droplet collisions result in momentum transfer and takeoff of secondary charged droplets containing material from the extracted from the surface.[93-94] These secondary droplets depart at a range of speeds and angles relative the surface, but all are smaller and slower than the primary droplets exiting the ion source. Droplets scattered at larger angles have lower velocities and larger droplet diameters, whereas smaller droplets with higher velocities depart at a smaller angle and are carried by the gas flow that generally flows along the sample surface.[91] The analytes contained in the secondary droplets then undergo the same ionization processes as in ESI (ion evaporation or charge residue models), ultimately forming gas-phase ions.[91, 93-94] One key argument supporting the similarity in ionization mechanism in ESI and DESI is that both produce similar mass spectra. Additionally, ESI and DESI both generate ions with similar internal energies as measured by the "survival yield" method.[54]

The primary variables that affect the overall performance of a DESI experiment are (1) source settings – spray solvent composition and flow, gas flow, high voltage, (2) source-

sample-inlet geometry – variables diagramed in Figure 1.3, and (3) sample stage motion parameters – scan speed, direction and line step height. These particular conditions all play a key role in desorption and ionization of the sample surface. Furthermore, when these variables are carefully controlled, DESI may be used for highly reproducible sample[95-96] screening and also mass spectrometry imaging.[80, 88]

1.5.4 DESI: Source Configuration and Solvent Considerations

In the choice of solvent composition for DESI the user must consider (1) spray impact spot size, which is related to the volatility of the solvent, (2) analyte solubility and (3) ability to ionize target analytes. Common spray solvents include volatile polar organic solvents like those typically used in ESI, as well as mixtures with water in variable volume fractions. These solvent compositions are used for many of the same practical reasons they are used in ESI such as smaller droplet size, but also several other DESI-specific reasons discussed below. Organic solvents with lower vapor pressure have been shown to produce smaller DESI impact spot likely due to solvent evaporation at the periphery of the jet.[97] This conclusion also holds true for organic-water mixtures in which a higher organic content also results in a smaller impact spot. Lower solvent flow rates (< 2 μL min^{-1}) and higher gas pressures (> 125 psi) also reduce the size of the impact spot, while at the same time sufficient solvent must be delivered to wet the surface and ensure analyte extraction. A smaller impact spot from the DESI spray means a smaller area of the surface is sampled, which can present sensitivity challenges based on absolute abundances of analytes. However, a smaller spot is highly beneficial for MSI experiments as it allows for higher spatial resolution.

The ionization efficiency in DESI is strongly dependent upon the solubility of the analyte in the spray solvent as desorption relies on the localized microextraction of analyte from the sampling surface. In fact, DESI efficiency is linearly related to analyte solubility.[97] Non-aqueous solvent systems[98] or the use of additives (i.e. surfactants)[99]

therefore offer a practical value in the analysis of hydrophobic analytes.[98] Alternatively, solvent additives may be used to enhance ionization of a target analyte in such a way that increases sensitivity[76, 78, 100] and/or selectivity.[76, 101] This technique known as "reactive DESI" takes advantage of the thin film deposited on the sample surface where heterogeneous chemical reactions take place between reagents and analytes. The products of these reactions are then transported in the secondary DESI droplets and detected by the mass spectrometry. The additive may be as simple as an ionic species in the form of a salt (i.e. NH_4^+, Cl^-, Br^-, etc.) that enhance adduct formation and ionization or as complex as reagent that forms a covalent complex with the target analyte.[78] This technique has been successful in the detection of explosives,[76, 102] active pharmaceutical ingredients and natural products,[78, 100] cis-diol functional groups,[101] and cholesterol,[103] among others.[104]

1.5.5 DESI: Geometry

The DESI source is typically mounted on an X-Y-Z translational stages with fine motion control for manual alignment of the system. To interface the set-up with a mass spectrometer, an extended transfer capillary is used to collect desorbed secondary microdroplets and ions for mass analysis. The sample is then mounted on a moveable stage whose motion may be automated for improved reproducibility and imaging capabilities. The configuration of these three components play a key role in DESI behavior, reproducibility and imaging capabilities. The experimental variables related to geometry and alignment are diagrammed in Figure 1.3 and should be optimized for each experiment.

The DESI source is typically positioned 1-5 mm above the sample (d_1) at an angle of 40-65° relative to the surface (α). Due to the dispersion of the primary solvent droplets, a smaller sprayer-to-surface distance results in a smaller area impacting the sample. Upon exit from the DESI source, primary droplets slow due to drag forces and collisions with ambient air.[91] Therefore the smaller sprayer-to-surface distance also means faster droplets impact the surface imparting a greater force for more effective momentum transfer and

desorption. As the angle of the sprayer decreases (approaching the sample surface) signal increases linearly down to ~30°, presumably due to greater momentum transfer in the direction of the mass spectrometer inlet.[95] However at smaller angles, the shape of the elliptical impact spot becomes more elongated and an increase in splashing onto the surrounding sample surface is observed. The most effective desorption occurs at the back of the impact spot in the area closest to the DESI source, and splashing is greatest away from the source towards the mass spectrometer inlet (along the Y dimension of analysis).[94, 105] The elongation of the impact spot is detrimental for spatial resolution, particularly in the Y dimension of the image, but the splashing is even more undesirable as it disrupts the native environment of the sample and will affect signal observed for adjacent areas imaged.

Taking into account the dynamics of secondary droplets generated during the DESI process,[91, 93-94] the mass spectrometer inlet position can be adjusted for maximum ion droplet collection depending on the size of droplets produced by the specific DESI source. Typical placement of the transfer capillary inlet is close to the sample surface (< 1 mm, but not actually touching) at an angle of 10-30° relative to the surface (β) and a distance of 3-8 mm between the sprayer and inlet (d_3). However, the more crucial factor in the sprayer-inlet separation is the distance between the impact zone of the DESI spray and the inlet, for which significant increases in signal are observed when this distance is 3-4 mm.[106]

1.5.6 DESI: Imaging Capabilities

In order for DESI to become a widely adopted analytical tool, it must not only efficiently analyze products on surfaces, but it must also be reproducible. This is especially true for imaging experiments, where consistent performance is necessary to form accurate chemical conclusions from relative abundances observed. The repeatability of experiments performed using DESI depends mostly on source geometries and flow stability. After optimization of sprayer-surface-inlet geometry, the DESI source is typically fixed during surface imaging. However these distances may change if the sample surface is not perfectly

level or is irregular in nature. In MALDI and SIMS, the instrumentation housing the sample stage and ion sources are generally fixed and enclosed in a vacuum chamber, therefore variability in these parameters is usually negligible. However, changes in the DESI source orientation (specific variables schematically shown in Figure 1.3) will affect the size of the surface area sampled and ion transport to the mass spectrometer.[95, 107]

Whereas MALDI and SIMS use a pulsed primary beam, DESI employs a continuous solvent spray throughout analysis. For imaging applications, the DESI spray is rastered in uni-directional line scans using a software-controlled stage while continuously acquiring mass spectra. Through the time domain, m/*z* information is correlated with the chemical species' spatial distribution. Due to solvent splashing/washing in the impact region in the direction of the mass spectrometer inlet as previously discussed, the direction of motion of the sample underneath the DESI surface plays a key role in the image quality. Therefore when imaging, the sample should be moved in such a way that the areas closest to the mass spectrometer are sampled first, then line stepping "backwards" so that the integrity of the sample is maintained throughout the experiment. Splashing in the X-dimension, though less significant than in the Y-dimension should also be considered when selecting motion parameters for a DESI-MSI experiment. When a rastering motion is used to scan the sample surface below the DESI source (each row in the X dimension is scanned using opposite directions of motion, i.e. left-to-right then right-to-left), an offset in spatial assignment for m/*z* signals is observed.[107] However, this offset is negligible when using uni-directional line scans (i.e. left-to-right scans only). This is primarily attributed to washing of the sample in the direction of motion, and when scanning in one direction, the whole surface is affected uniformly resulting in a better representation of the sample. As previously mentioned, lower solvent flow rates reduce the impact spot size and degree of splashing, but the splashing phenomenon cannot be completely avoided.

The spatial resolution in a DESI-MSI experiment is ultimately defined by the size of the impact spot, which is ~200 μm under typical operation conditions. Pixel sizes are

determined based on the speed of the stage motion and acquisition rate of the mass spectrometer. Spatial resolutions of 100 μm are attainable by DESI with fine control of the alignment and geometry variables, and to date the highest spatial resolution reported is 35 μm.[108] Standard DESI ion sources use a solvent capillary made of fused silica with an inner diameter (i.d.) of ~50 μm, and outer capillaries carrying the spray gas with an i.d. of ~180 μm. The reduction of the inner diameters of the inner solvent capillary (~20 μm) in the DESI ion source significantly reduce the size of the impact spot, thus improving spatial resolution, but it quickly reaches a limit where signal-to-noise becomes inadequate.[109] Similar to MALDI, oversampling has also proven to be effective for DESI imaging by moving the sample at a speed significantly slower than the mass spectral acquisition rate. An additional benefit of oversampling in DESI-MSI is improved signal to noise as the slow motion of the spray allows more time for wetting the sample surface and subsequent analyte extraction for desorption and ionization.[109]

1.5.7 Additional Techniques Used in Ambient Ionization Mass Spectrometry Imaging

Other techniques used for ambient MSI still require localized surface sampling, which typically involves liquid extraction or laser desorption/ablation. Variations to the DESI ion source, such as EASI, in which no high voltage is applied to the pneumatic spray may also be used for MSI.[68, 110-111] Another variation of DESI is Nanospray-DESI (Nano-DESI) in which two capillaries are used to form a solvent bridge across the sample surface.[112] One capillary supplies the solvent, and the second capillary transports dissolved analyte from the bridge into the mass spectrometer for detection.[112] Nano-DESI has been successfully applied to tissue imaging with spatial resolution better than 12 μm,[113-115] but the fragile nature of the solvent bridge has prevented its widespread aplication A more unique liquid-based extraction method using a LMP-SSP[69] developed by the Van Berkel group has also been used for imaging applications.[116-117] The LMP-SSP consists of two small coaxial capillaries (inner i.d.: 125 μm, outer i.d.: 230 μm), with the outer capillary

delivering solvent to the sample surface and the inner capillary drawing the liquid from the surface back up and into an ESI source thereby using a two-step desorption-ionization process. When the probe is placed within ~50 μm of the sample surface, analyte extraction takes place, and by moving the probe along the surface a chemical image may be generated. However the need for precise alignment of the probe with respect to the surface is challenging preventing this technique from becoming widely applicable. Furthermore, it may only be applied to hydrophobic surfaces such as reverse-phase thin layer chromatography plates; hydrophilic and wettable surfaces resulted in radial diffusion of the liquid that moved the sampling area beyond the probe.[69]

In contrast to the liquid-based ambient desorption/ionization methods used for MSI, alternative two-step desorption via laser ablation/desorption followed by a separate ionization step are growing in popularity. Coupling of laser ablation to inductively coupled plasma (ICP),[118] APCI,[119-121] plasma ionization sources,[74-75] and ESI[73, 122-124] or AP-MALDI[125] take advantage of the small impact spot generated by the focused laser pulse for higher spatial resolution in MSI. For effective analyte desorption, the sample must absorb the laser energy (as discussed with the selection of MALDI matrix). For this reason, UV (λ = 337 nm) or IR (λ =10.6 μm) lasers may be used depending on the sample under investigation or desired desorption properties. Even so, samples suitable for these conditions are typically limited to those with high water content that strongly absorbs the 10.6 μm irradiation or a matrix is used to enhance desorption (as in matrix assisted laser desorption electrospray ionization, MALDESI)[126].

The methods involving ICP, APCI and MALDI ionization, often still require the presence of a sample enclosure to ensure effective analyte transport and ionization making them not truly ambient techniques. Challenges in coupling laser ablation with a separate ionization source at ambient pressure while maintaining high sensitivity have significantly limited the widespread application of these techniques for imaging.

1.6 Conclusion

Advances in instrumentation have made mass spectrometry imaging a very diverse field with a variety of ionization methods capable of direct surface sampling. These techniques vary in the spatial resolution, chemical information and ease of use they allow. The advantages and disadvantages have made each suitable for unique specialized applications, yet the field faces a number of challenges. While the direct analysis of a surface is highly desirable, the lack of chemical separation can result in ion suppression and limit the ability to confidently identify analytes detected. Therefore, some form of nested acquisition (tandem MS, ion mobility-based separation), though it does not correct for ion suppression, can assist in the selectivity of the analysis. Another such limitation is that existing techniques are restricted to the imaging of flat surfaces, dictated by strict source geometry and vacuum restrictions. Finally, MSI experiments produce a vast amount of data and chemical information. Even still, efficient processing of such datasets supported by multivariate analysis can lead to significant scientific advances from this powerful analytical tool.

CHAPTER 2. INCREASING CHEMICAL COVEREAGE OF LIPID SPECIES BY DESI AND MALDI MASS SPECTROMETRY IMAGING

Adapted with permission from

Bennett, R. V.; Gamage, C. M.; Fernandez, F. M., Imaging of Biological Tissues by Desorption Electrospray Ionization Mass Spectrometry. JoVE 2013, (77), e50575.

Bennett, R. V.; Paine, M. R. L.; Hogan, S. R.; LaPlaca, M. C.; Fernandez, F. M., Increasing Chemical Coverage of Lipid Species by DESI and MALDI Mass Spectrometry Imaging to Study Traumatic Brain Injury, In Preparation.

2.1 Abstract

Mass spectrometry imaging (MSI) provides untargeted molecular information with high specificity and spatial resolution for investigating biological tissues at the hundreds to tens of microns scale. This makes it an invaluable tool in the localized search for biomarkers of traumatic brain injury (TBI), especially lipid species that may undergo peroxidation resulting from the injury. The desorption/ionization technique selected used to perform MSI is critical in determining the observable chemical diversity as well as the specific spatial features within a tissue. The two most commonly-used MSI methods for tissue imaging are desorption electrospray ionization (DESI), an ambient spray-based ionization tool, and matrix assisted laser desorption ionization (MALDI), a vacuum laser-based ionization technique. The unique chemical conditions under which analytes are desorbed and ionized from the tissue section will inevitably affect the types of molecules sampled for mass spectrometric detection. Previous literature reports using MSI to investigate TBI have shown somewhat contradictory results depending on the ionization

source chosen and data processing workflows used. Therefore, an unbiased comparison of the sample preparation, ionization, and data processing methods as it relates to visualization of lipid species significant for TBI was performed. In this study, rats were injured by controlled cortical impact and tissue sections were imaged by both DESI and MALDI-MSI in both positive and negative ion modes, with different tissue preparation methods. Results indicate that each approach offers unique benefits thus making both valuable complementary techniques for imaging of lipid species in biological tissues.

2.2 Introduction

Arguably, the most common application of mass spectrometry imaging (MSI) has been to the investigation of biological tissues.[7, 127-129] MSI has several advantages over other tissue imaging techniques (microscopy, magnetic resonance imaging, etc.) because it does not require a target-specific label and has the capability of monitoring thousands of molecules in a single experiment. Biomolecules such as proteins,[23, 130] peptides,[131] and metabolites, endogenous and exogenous, such as lipids[6, 132-134] or drugs[117, 135-137] have all been imaged successfully by MSI in a wide range of tissue types.[6, 132, 138-139]

MSI is frequently performed on tissues using matrix assisted laser desorption ionization (MALDI),[23] secondary ion mass spectrometry (SIMS),[5] and ambient ionization techniques, including desorption electrospray ionization (DESI),[80] laser ablation-electrospray ionization (LAESI),[73, 124] and liquid micro-junction-surface sampling probe (LMJ-SSP).[117] As previously discussed, the selection of ionization technique used for MSI is crucial in determining the attainable spatial resolution and detectable mass range (Figure 2.1). SIMS offers the highest spatial resolution, but is limited to smaller analytes due to the high energy of the primary ion beam, whereas MALDI offers high spatial resolution and a

broader mass range that includes intact proteins. Alternatively, DESI allows for moderate spatial resolution imaging of analytes < 2000 Da. However, the selection of the appropriate MSI tool for any given application is much more complex that these two figures of merit. Factors such as chemical diversity, ease of use, and sample compatibility must also be considered.

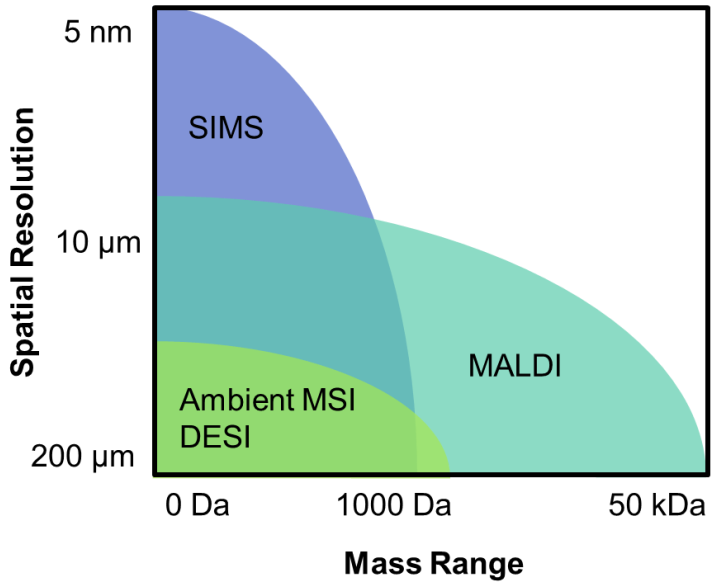

Figure 2.1. Comparative spatial resolution and mass rage attainable by SIMS, MALDI and DESI/Ambient MSI techniques.

Untargeted imaging by mass spectrometry facilitates the acquisition of chemical information for discovery and hypothesis-generating applications. In a quasi-targeted mode, when a specific class of analyte is targeted, the chemical coverage afforded by the MSI technique is crucial for the complete understanding of the biological process under investigation; it is difficult to form conclusions about the system when you cannot detect the majority analytes in the first place. Targeted imaging of a known chemical of interest,

on the other hand, can facilitate increased sensitivity and selectivity through specific method development.

Lipids are a common class of analyte targeted in MSI due to their essential role in cellular function including the self-assembly to form the membrane bilayer of every living cell.[140] In addition to their role as structural components of all cell membranes, such as the blood brain barrier, membrane lipids also play a role in signal transduction as well.[141] Lipids have been implicated in many diseases including, but not limited to Down's Syndrome,[142] Tay-Sachs/Sandhoff disease,[39] Alzheimer's disease,[143] traumatic brain injury (TBI),[144-145] and various cancers.[86, 146] Up 50% of the dry weight of the brain is made up of lipids. They may be generally classified into three categories: cholesterol, sphingolipids, and glycerophospholipids. In positive ion mode, the mass spectrum is dominated by phosphatidyl cholines (PCs) due to the positively charged quarternary ammonium group present in the choline head. However, a greater diversity of lipids may be detected in negative ion mode including phosphatidylethanolamine (PE), phosphatidylserine (PS), phosphatidylinositol (PI), sulfatide (ST), and many others. Almost all types of ionization techniques used for MSI have been successfully applied to the field of lipid imaging,[147] including SIMS,[12] MALDI[132, 134, 148-151] and DESI.[80, 85] High lipid diversity and/or sensitivity in MSI depends heavily upon the sample preparation method, and involves tissue handling, sample treatment, and efficient analyte extraction.

First, the tissue should be prepared to minimize analyte loss or contamination. In standard practice for MSI, fresh-frozen tissues are directly sectioned using a cryomicrotome without the use of an embedding medium. Common embedding media used for histological purposes, such as optimal cutting temperature polymer (OCT), are not

recommended as they significantly suppress analyte ion signals.[24] Alternative MSI-friendly media such as gelatin[152] or carboxymethylcellulose[153] may be used for small or fragile samples.

Next, tissue sections may be specially treated to enhance sensitivity for target analytes or compound classes. For MALDI-MSI, tissues are commonly washed to remove unwanted molecules or salts from the tissues.[154] For proteins and peptides, this wash step typically involves an organic solvent mixture to fix the tissue to the target and remove lipid species that suppress protein signal.[154] Alternatively, an aqueous pH-neutral buffer wash has shown to enhance sensitivity of lipid species in both positive and negative ion mode.[155] The wash step removes salts from the sample, which results in a simplified spectrum observed in positive ion mode as the formation of salt adducts is reduced and the primary species observed are protonated ions. In negative ion mode, it is suggested that the wash step removes analytes that might cause ion suppression resulting in an increase in signal for lipid species.[155] This washing step has yet to be applied to DESI-MSI, but would presumably show in similar improvements. Reactive DESI-MSI has also shown to be a powerful tool for enhancing detection of low-molecular weight metabolites in tissues or increasing ionization efficiency of target analytes.[76, 78, 100, 156]

The final step in sample preparation for MSI that significantly affects sensitivity and chemical coverage of the method involves analyte extraction for ionization. In MALDI, this is determined by the matrix compound selected and the method by which it is deposited on the tissue. Common matrices used for lipid imaging include 2,5-dihydroxybenzoic acid (DHB, the most popular),[140] 1,5-diaminonapthalene (DAN),[157] or 9-aminoacridine (9-AA),[158-160] in addition to matrices designed for specific lipid targets.[36,

[161] Successful analyte ionization depends heavily on the ability of the analytes to be extracted into the matrix crystals, making chemical compatibility crucial. This extraction process occurs in situ during matrix deposition, therefore the deposition method chosen will inherently affect chemical coverage and sensitivity. Matrix deposition is typically performed using small matrix droplets, as in pneumatic nebulization[24] or using an oscillating capillary nebulizer (OCN)[39] for localized extraction aided by the presence of a solvent. Alternatively, matrix deposition by sublimation, with or without a solvent present, can produce a homogeneous matrix coating with reduced impurities introduced into the matrix layer.[40] In DESI-MSI, the extraction of analytes into the ionization space is heavily dependent on the spray solvent selected; the analyte must be able to dissolve in the solvent during the microextraction process for effective desorption and ionization.[97] Therefore, common solvent systems for imaging of lipid species in biological tissues generally include high amounts of organic solvents such as methanol, acetonitrile or N,N-dimethylformamide (DMF) that are compatible with lipids.[83]

For this study, lipid detection was of particular interest as they relate to TBI.[144, 162] TBI is a major public health concern, and recent media attention has led to heightened awareness of the growing concussion problem among other forms of TBI.[163] The membrane lipids in the brain are highly enriched in polyunsaturated fatty acids such as arachidonic acid, and are susceptible to oxidative damage resulting from reactive oxygen species generated from TBI.[144, 164] Most research focuses on measuring oxidative damage to membrane lipids which result in alterations in abundance and distributions within the injured tissue. MSI is therefore a suitable technique by which to measure these changes as it is capable mapping spatial distributions of lipids with high chemical specificity. Previous

MSI studies of brain injury have suggested increased formation of lyso-PCs resulting from lipid breakdown,[165-167] as well as changes in relative salt concentrations within the tissue (Na, K).[115, 168] Salt fluxes in injured tissue are widely accepted, but the methods by which the changes have been characterized, particularly as lipid adducts, are hotly contested.[115] Anionic lipid species including cardiolipins[145, 169] in addition to select PS and PI species have also been found to undergo lipid peroxidation.[144] Additional products of the lipid peroxidation include fatty acids and diacylglycerols, which have been shown to increase in injured spinal cord tissues.[156] Finally, several MSI studies have found an increase in ganglioside abundance in several types of TBI.[36, 170] Ultimately, an understanding of all of these metabolic changes is necessary to understand TBI for diagnostic and treatment purposes. Therefore this study was designed to optimize both DESI and MALDI-MSI protocols for maximum chemical coverage in order to better characterize lipid alteration in TBI in a unified manner. DESI and MALDI have been characterized as complementary MSI techniques, with DESI being suitable for small-molecule imaging and MALDI suitable for large-molecule imaging. To my knowledge, there has yet to be a direct investigation of their respective abilities to detect and image lipid species in an unbiased manner, therefore, this investigation also sought to qualitatively compare the two techniques in this regard. Scheme 2.1 provides an overview of the sample preparation steps that were investigated in this study as they relate to chemical coverage in both positive and negative ion mode.

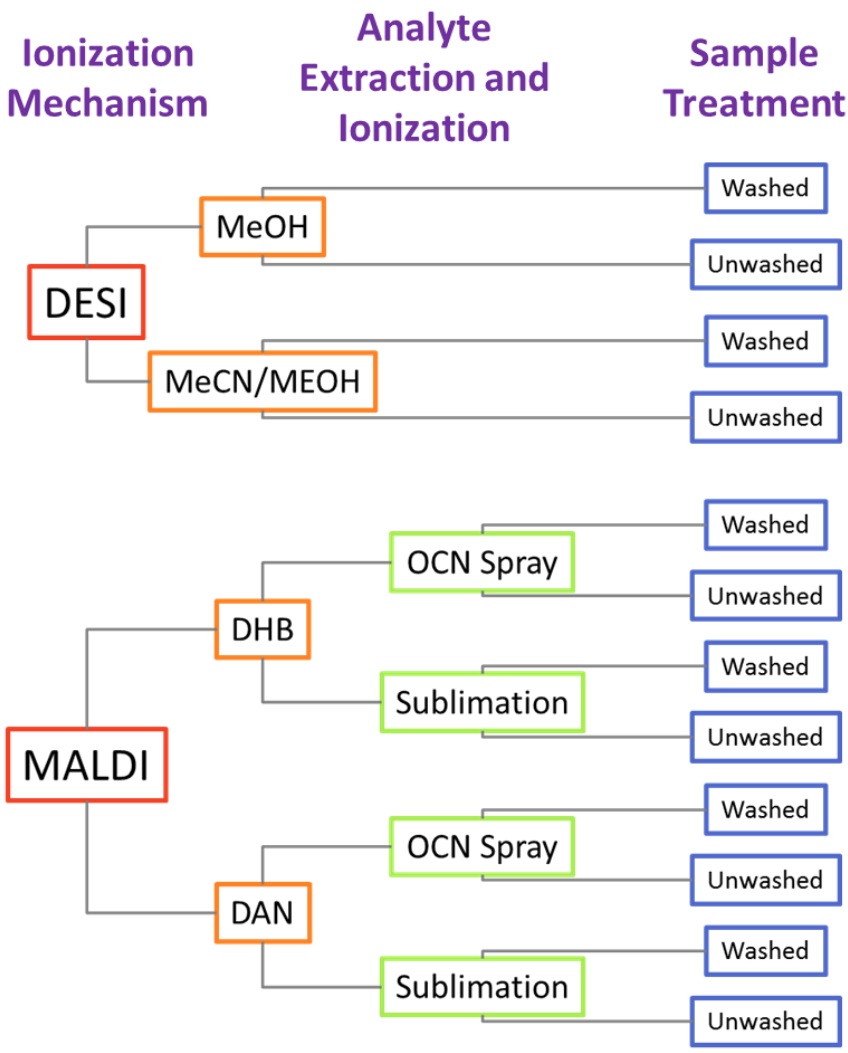

Scheme 2.1. Overview of experimental variables examined in this study for maximum lipid diversity and sensitivity including ionization technique, DESI spray solvent, MALDI matrix composition and deposition method, and tissue pretreatment approach.

2.3 Experimental Details

2.3.1. Traumatic Brain Injury and Sample Collection

Rat brain tissues were collected and handled with the approval of the Georgia Tech Institutional Animal Care and Use Committee (IACUC). Male Sprague-Dawley rats (Charles River) weighing 200g-300g were injured using a Controlled Cortical Impact

(CCI) device (Pittsburgh Precision Instruments). A 6mm craniectomy was performed, exposing the brain lateral to the sagittal suture, between lambda and bregma. The blunt impact injury was applied to the cerebral cortex by an air-driven piston with a flat 5 mm diameter impact tip, to a depth of 2 mm and at a speed of 3m s^{-1}. The incision was sutured closed and the animals were allowed to recover for 24 hours at which point they were sacrificed and the brain was dissected. The brain specimens were flash-frozen in an isopentane-liquid nitrogen mixture and stored at -80° C until they were sectioned. The flash-frozen tissues were sectioned using a CryoStar* NX70 Cryostat (Thermo Scientific, Kalamazoo, MI, USA) with a sample temperature of -30 °C and a blade temperature of -25 °C. Tissues were sectioned with a thickness of 14 μm and were thaw-mounted on glass microscope slides (VWR, Radnor, PA, USA) for DESI-MSI or indium tin oxide (ITO)-coated glass slides (Bruker Daltonik GmbH, Bremen, Germany) for MALDI-MSI. Two tissue sections were mounted on each slide, one to be washed and one to remain unwashed. Slides were stored at –80 ^{0}C until the time of analysis, at which point, tissues were allowed to thaw at room temperature inside a vacuum desiccator (Vacuum Sample Saver^{TM}, VWR, Radnor, PA, USA) for 20 minutes.

2.3.2. Materials and Chemicals

Ammonium formate (NH_4Form, >99%), dihydroxybenzoic acid (DHB) and diaminonapthalene (DAN) were acquired from Sigma Aldrich (St. Louis, MO, USA). Acetonitrile and methanol were LC-MS grade from EMD Millipore (Billerica, MA, USA).

2.3.3. Sample Treatment by Washing

The aqueous buffer of 50 mM ammonium formate (NH_4Form, pH 6.5) was prepared fresh in ultrapure water (18 MΩ cm) and chilled to 4°C for each sample. Tissue sections were washed by submerging one tissue section in the NH_4Form buffer for 5 seconds; the second tissue on the slide was left unwashed. This was repeated a total of three times in fresh buffer solutions, and excess NH_4Form was removed from the back of the slide and around the tissue section using a laboratory tissue (VWR, Radnor, PA, USA) after each step. Special care was taken not to agitate the mounted sample during washing. After washing, the sample was placed back in the vacuum desiccator to dry for 20 minutes.

2.3.4. Oscillating Capillary Nebulizer Matrix Deposition for MALDI-MSI

The design of the oscillating capillary nebulizer (OCN) unit is described elsewhere,[39] but briefly, consists of two coaxial capillaries delivering the matrix solution through the inner capillary (i.d. 50 μm, o.d. 150 μm) and nebulizing N_2 gas through the outer capillary (i.d. 250 μm, o.d. μm). The inner capillary tip extended ~1 mm beyond the outer capillary and the OCN unit was positioned ~10 cm above the sample. The DHB matrix solution was a 30 mg mL^{-1} solution in acetonitrile:water (1:1) with 0.1% trifluoroacetic acid (TFA) and delivered at a flow rate of 40 μL min^{-1} and a nebulizing gas (N_2) pressure of 50 psi. The DAN matrix solution was prepared as a saturated (25 mg mL^{-1}) solution in acetonitrile:water (1:1) with 0.1% TFA and delivered at a flow rate of 40 μL min^{-1} and a nebulizing gas (N_2) pressure of 50 psi. It should be noted that DAN is a nonpolar matrix substance, and other solvent systems with higher organic content were

tested for enhanced solubility, but these resulted in matrix crystallization at the tip of the OCN sprayer that prevented consistent delivery.

Matrix droplets were deposited on the tissue samples my moving the sample continuously under the OCN sprayer using a in a circular motion at a speed of 5 mm s^{-1} for 15 minutes for DHB deposition and 5 minutes for DAN deposition. Each tissue section was coated individually immediately prior to MALDI-MSI analysis; to ensure only one tissue section was coated at a time, the second tissue was covered using a glass Petri dish during matrix application to the first tissue. Then the second tissue was subsequently coated prior to imaging.

2.3.4. Sublimation of Matrix for MALDI-MSI

MALDI matrix application by sublimation was performed using a system similar to the one described by Hankin et al.[40] and is shown in Figure 2.2. The sample slide was mounted on the underside of a flat-bottom condenser that was filled with ice water. Solid matrix powder (100 mg) was placed in a Petri dish in the bottom of the vacuum apparatus. The two pieces were assembled with an O-ring seal connected to a vacuum pump (Edwards RV12 two-stage rotary vane pump). Based on the specifications of the vacuum pump used in this study, the reduced pressure in the vacuum chamber is estimated to be on the order of 10^{-3} Torr. After 15 minutes at reduced pressure, heat was applied to the base of the sublimator by a heating plate. Sublimation of the solid matrix sufficiently coated the sample surface after 15 minutes at which point the sample was removed from the vacuum chamber and imaged by MALDI-MSI. The sublimation conditions were optimized for the specific matrix compounds used with this particular system and precise measurement of the temperature of pressure would be necessary to different sublimation systems.

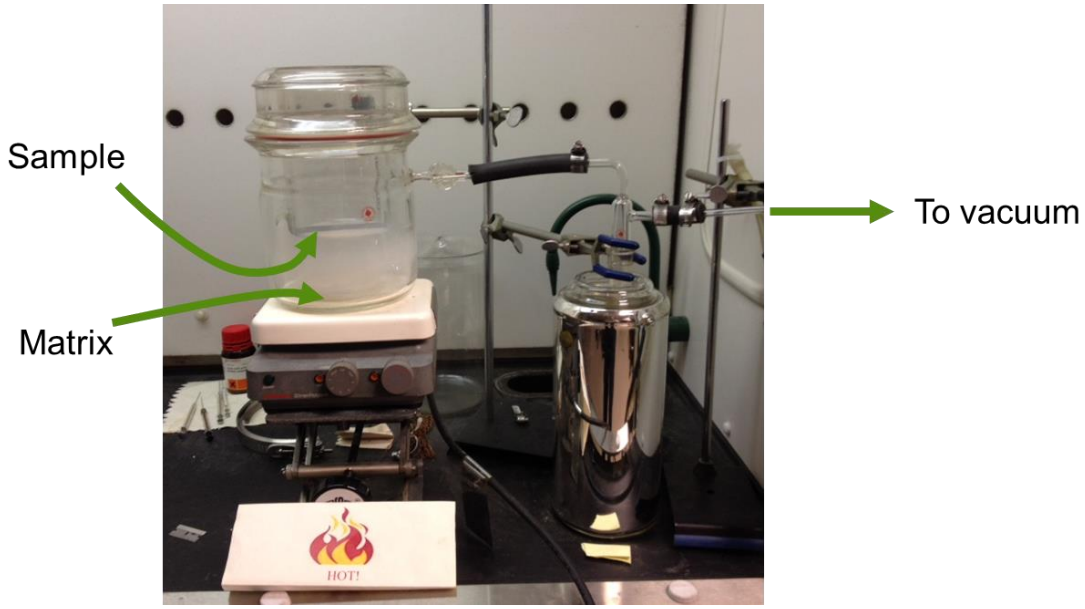

Figure 2.2. Sublimation apparatus for MALDI matrix deposition.

2.3.5. MALDI-MSI of Tissue Sections

MALDI-MSI of the matrix-coated tissue sections was performed using an Autoflex III MALDI-TOF/TOF mass spectrometer (Bruker). ITO slides were mounted in the MTP Slide Adapter II (Bruker). Mass spectra were acquired in positive and negative ion mode for m/z 200-1800. The laser was fired at a frequency of 200 Hz for 100 shots at each sample point, and a raster step of 100 μm in the x and y-dimensions. The laser power was optimized for each matrix and polarity for signal-to-noise and mass resolution; a minimum laser energy was required to obtain signal, and further increase in power increased sensitivity, but at the cost of mass resolution. The laser spot size was estimated to be ~80 μm in diameter given the laser power and focus used.

2.3.6. DESI-MSI of Tissue Sections

DESI-MSI was performed using an an OmniSpray DESI probe (Prosolia Inc., Indianapolis, IN) spraying methanol or methanol-acetonitrile (1:1) at a flow rate of 5 μL min^{-1} and a N_2 nebulising gas pressure of 140 psi. Other organic solvent systems were tested in preliminary experiments, but these two showed the best performance and are therefore the focus of this report. The DESI source geometry was optimized prior to each experiment for maximum sensitivity and minimal impact spot size. Typical source geometry employed a sprayer-surface distance of ~3 mm at an angle of 55° and a sprayer-inlet distance of ~5mm. The sample was rastered using a motorized microscope stage (OptiScan II, Prior Scientific Inc., Rockland, MA) controlled by a Labview VI described elsewhere[171-172] moving at a speed of 160 μm s^{-1} with a line step of 200 μm. Mass spectra were acquired on an Exactive Plus mass spectrometer (Thermo Scientific, San Jose, CA) with mass resolution set to 35,000 and a mass window of 150-1800 Da at a rate of 2.5 scans s^{-1}.

2.3.7. MSI Data Visualization

MALDI-MSI data was exported in the Analyze 7.5 format for visualization. RAW files acquired from DESI-MSI experiments were converted to the .mzxml format using "msconvert" and processed with the position and time information of the microscope stage to correlate MS data with spatial position. All data was visualized using omniSpect.[171] The image data cubes (.mat format) generated by omniSpect were downloaded and used for further processing in Matlab. All ion images presented here show normalized ion intensities relative to the total ion intensity count within each respective pixel. This normalization

helps to correct for inhomogeneity in matrix deposition or inconsistent DESI spray delivery that might affect ion intensities during imaging. To compare fold-changes of different lipid species between injured and contralateral tissues, regions of interest (ROI) were generated in Matlab for the different tissue types and average mass spectra were calculated from the respective ROIs. Changes in ion intensity between injured and contralateral tissue were calculated from these averaged spectra.

2.4 Results and Discussion

2.4.1. MALDI Matrix Selection and Deposition Method

For MALDI-MSI, two matrices (DHB and DAN) were tested in both positive and negative ion mode to study the observable lipid diversity with each. This comparison was carried out using the OCN sprayer matrix deposition method. Representative mass spectra averaged across the entire tissue section are shown for positive (Figure 2.3a) and negative (Figure 2.3b) ion modes. Chemical background or matrix ion peaks were labeled as such based on higher ion intensity beyond the edges of the tissue area. In positive ion mode, DHB enabled detection of a greater number of peaks in the 700-900 m/*z* range, the range in which many phospholipids and sphingolipids are detected, also with greater signal to noise. Signal-to-noise is more significant than absolute intensities as it ultimately affects image contrast in MSI, but the absolute intensities indicated in Figure 2.3 also serve as a reference for comparative purposes. In negative ion mode, DAN facilitated the detection of more lipid species in the 700-900 m/*z* range with significantly higher signal-to-noise than DHB. Furthermore, the low-mass range of the DAN spectrum (< 600 Da) also exhibited reduced chemical background originating from matrix ions, enabling detection

of what may be fatty acids or diacylglycerols that may be altered following TBI. Moving forward, DHB was selected as the optimal matrix for positive ion mode analysis, whereas DAN was selected for additional negative ion mode analysis.

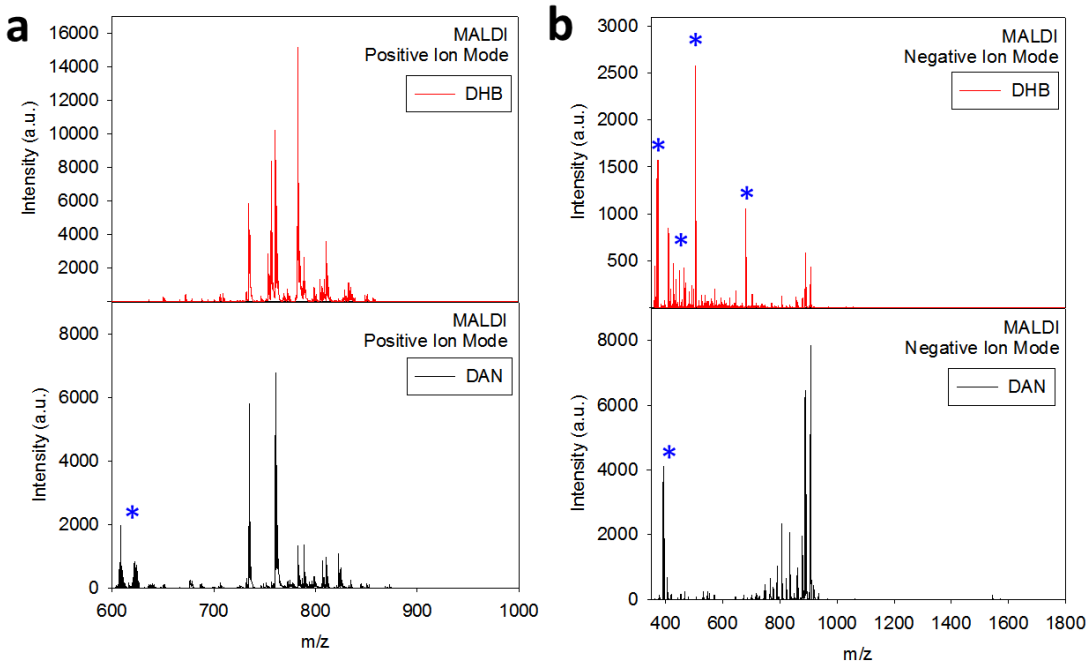

Figure 2.3. Average spectra obtained by MALDI-MSI across entire brain tissue sections acquired in positive (a) and negative (b) ion modes with two matrices: DHB and DAN to determine which enables detection of greater lipid diversity. Peaks indicated with (*) are attributed to matrix or background ions not from the tissue sample itself.

Next, the method by which the matrix was applied was investigated using two application methods: OCN spray deposition and sublimation. The effect of matrix deposition method on sensitivity and image quality was found to be heavily compound dependent. Figure 2.4 shows sample ion images generated for two lipid species using the two matrix deposition methods. One lipid imaged in negative ion mode, PS 40:6 (m/z 834.5440), showed an order of magnitude higher intensity using OCN spray deposition of DAN compared to sublimation (Figure 2.4 a-b). The identity of this particular lipid was

confirmed by tandem MS imaging directly on the tissue and mapping spatial distributions of unique fragments, which showed similar spatial distributions. ST d18:1/c20:0 is isobaric with PS 40:6 in negative ion mode with m/*z* = 834.5766, but characteristic ST fragments showed different distributions than the PS fragments allowing for the differentiation of the two species. Not only is signal intensity important to evaluate a MSI procedure, the effect on image contrast is also of particular interest as it affects the ability to discern spatial features within the sample. Therefore the contrast of this species was calculated between the stratum radiatum (the fine structure observed within the hippocampus) compared to the corpus callosum using five rows from each image and Weber's definition of contrast:[173]

$$C = \frac{I - I_b}{I_b}$$

where C is image contrast, I is the maximum intensity and I_b is the background intensity. Because PS 40:6 is showed significantly reduced abundance in the corpus callosum, this tissue region was used as the background signal. The contrast calculated for sublimation-based images was found to be 188473 compared to 1755 for the OCN image. Although sublimation quantitatively yields higher contrast, the normalized ion intensities were over an order of magnitude lower than the in the OCN image. The features within the hippocampus are still easily discernable in the OCN-based image, and together with the increased signal intensity may be considered the ideal matrix deposition method for the detection of PS 40:6. The second lipid image shown (Figure 2.4 c-d) as a comparison between OCN and sublimation deposition is for a positive ion mode signal, m/*z* 806.5425, tentatively as the protonated ion of PC 38:6 (Δm = 7.3 mDa, 9 ppm). In this case sublimation resulted in a five-fold increase in ion intensity and three-fold increase in image contrast compared to OCN deposition. Generally OCN spray deposition demonstrated

better signal-to-noise and facilitated detection of a greater number of lipid species, but this advantage was highly compound-specific and in some cases sublimation was superior. Therefore a specific matrix deposition method may be chosen if the target lipid species is known, however the sensitivity afforded by OCN spray is preferable for untargeted lipid imaging.

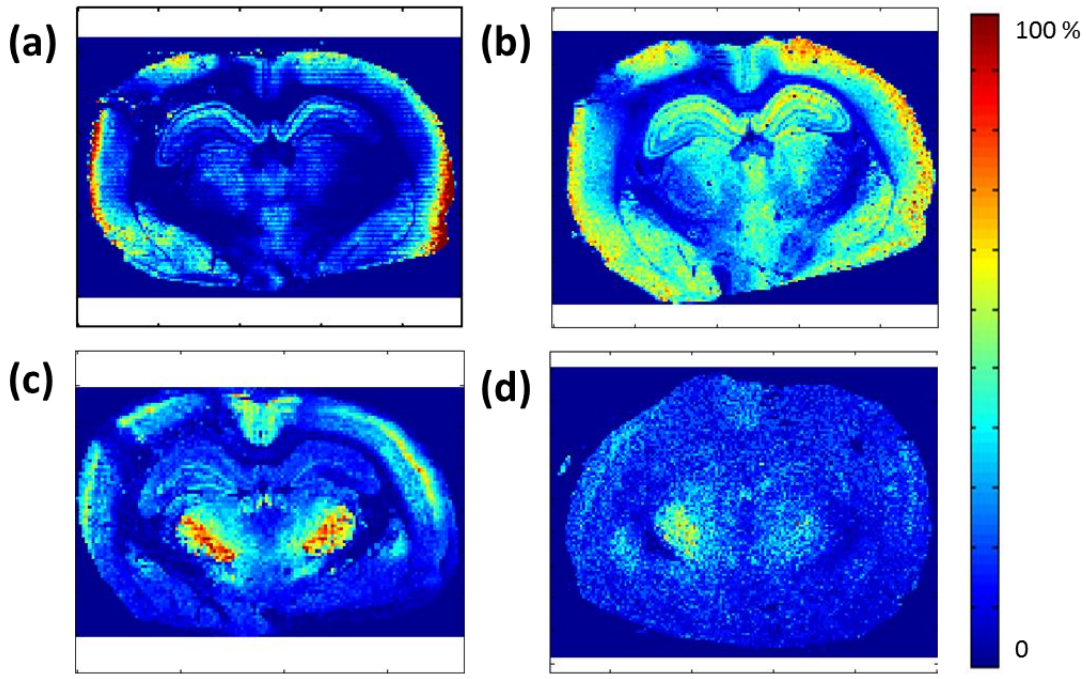

Figure 2.4. Ion images of PS 40:6, m/z 834.5440, (a-b) and PC 38:6, m/z 806.5452 (c-d) acquired by MALDI-MSI using two matrix deposition methods: sublimation (a and c), or OCN spray deposition (b and d).

2.4.2. DESI Solvent Selection

In contrast to MALDI-MSI, DESI-MSI does not require a matrix for analyte ionization, which provides an advantage in reduced sample preparation steps. Rather, ionization in DESI occurs via solid-liquid microextraction followed by ESI-like ionization

mechanisms.[91, 93-94] Therefore various solvent systems were tested for their ability to increase observable chemical diversity in DESI-MSI experiments through improved extraction. The top-performing solvent systems were found to be methanol and a 1:1 mixture of methanol-acetonitrile. High organic content in the DESI solvent spray has been advantageous in previous reports for analysis of hydrophobic substances, including lipids.[97-98, 133] In this study, these two methanol-based solvent systems performed well in positive ion mode, with comparable sensitivity, chemical coverage and image contrast (Figure 2.5), but showed subtle differences in ion "hot spots" within the images. This is presumably due to differences in extraction capabilities from various tissue matrices by the solvent systems. The pure methanol solvent system produced less chemical background from ionized solvent molecules or contaminants compared to the methanol-acetonitrile mixture.[174] The chemical background produced by the methanol-acetonitrile solvent system in negative ion mode dominated the spectra and suppressed all lipid signal such that imaging was nearly impossible in that mode. Therefore, all subsequent DESI-MSI optimization used 100% methanol as the spray solvent for both polarities.

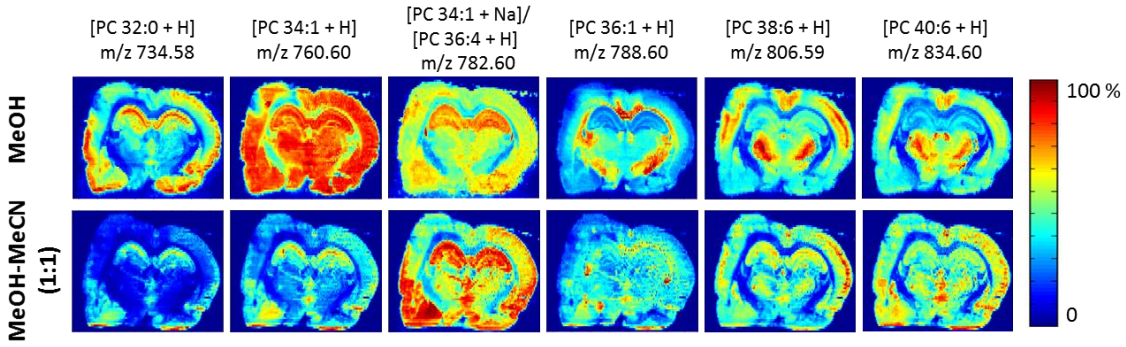

Figure 2.5. Select ion images acquired by DESI-MSI using methanol (MeOH) or methanol-acetonitrile (MeOH-MeCN) solvent systems. Each ion image intensity pseudo-color scale is defined individually with respect to the maximum ion intensity within each image.

2.4.3. Effect of Tissue Washing on Lipid Detection by MALDI- and DESI-MSI

As previously mentioned, sample washing has become common practice for tissue imaging in MALDI-MSI, and when performed carefully may enhance sensitivity while maintaining spatial integrity of the sample.[154-155] In this study, an ammonium formate buffer was chosen for tissue washing based on previous literature reports demonstrating its effectiveness. Ammonium acetate was also tested in preliminary experiments, but the NH_4Form buffer was superior in terms of lipid sensitivity. Serial tissue sections were imaged using optimized matrix (MALDI) or solvent (DESI) conditions, with alternating sections undergoing the washing procedure described in section 2.3.3 and the other tissues remaining unwashed. Washing with an aqueous buffer is an effective means by which to de-salt the tissue, ultimately reducing the formation of $[M + Na]^+$ and $[M + K]^+$ ions in positive mode and favoring the formation of $[M + H]^+$ ions.[165] This is highly beneficial for lipid imaging to simplify interpretation of the mass spectra eliminating sodiated ions that are isobaric with other protonated lipid signatures. As an example of this shift towards the formation protonated ions, Figure 2.6 shows images acquired by MALDI and DESI in positive ion mode for the lipid tentatively identified as PC 38:6 and its corresponding adducts. The relatively high mass errors in the mass measurements are attributed to possible overlap from isobaric phospholipids not resolved by the mass spectrometer. Observed potassiated adducts show the highest intensity in the unwashed samples, whereas the protonated species are the primary species detected in the washed tissues. This trend was true for all PC adducts observed in positive ion mode.

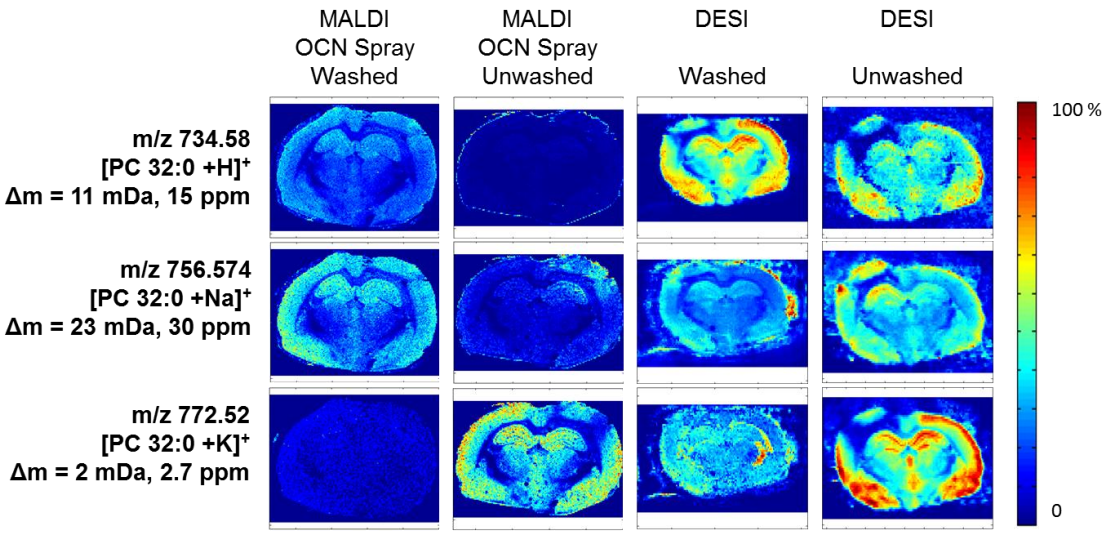

Figure 2.6. Ion images of PC 32:0 detected as various adducts – protonated, sodiated, and potassiated – by MALDI and DESI-MSI for washed and unwashed tissues. For both techniques, the formation of $[M + H]^+$ ions is favored after washing the tissue with NH_4Form. Intensity scales for each ion image are scaled linearly for the maximum observed signal for the respective ions.

In negative ion mode, washing did not result in a shift of adduct formation, rather similar lipid features were detected, but at much higher intensities after washing. This is in good agreement with previous reports that have suggested that this phenomenon is due to the removal of endogenous species that interfere with lipid ionization.[155] Additionally, I propose that the aqueous buffer wash step results in surface wetting that enhances analyte extraction into the MALDI matrix layer or the DESI solvent film. After washing, samples were dried in a vacuum desiccator for 15-20 minutes to dry out excess buffer. However the altered water content in the wetted tissue section will inevitably affect the kinetic mass transfer of analytes into the ionizable layer of the sample. The time allowed for this drying step is a balance between evaporation of excess buffer and tissue degradation after extended periods of time. Longer drying times may dry out additional buffer and return the

tissue closer to its original state, but a number of biomolecules present in the tissues would degrade on that time scale thus ruining the chemical integrity of the sample.[175] The drying time used in this study was also deemed adequate for removal of excess buffer based on lack of ammonium or formate adducts detected in positive and negative modes, respectively.

2.4.4. Comparison of Chemical Coverage Afforded by DESI and MALDI

The sample treatment and analyte extraction methods presented here ultimately affect the observable chemistry by MALDI- and DESI-MSI. Therefore a qualitative comparison between optimized MALDI and DESI protocols for tissue imaging was performed to investigate detectable lipid species using the optimized protocols. Beginning with positive ion mode, Figure 2.7a shows representative spectra acquired by MALDI and DESI across an entire tissue section; normalized ion intensities were used for the comparison as the data were acquired using different ion sources and mass spectrometers preventing a direct comparison of absolute intensity. Tissues were washed in both experiments; the DESI spray solvent was methanol and MALDI data shown was acquired with DHB applied using OCN spray deposition.

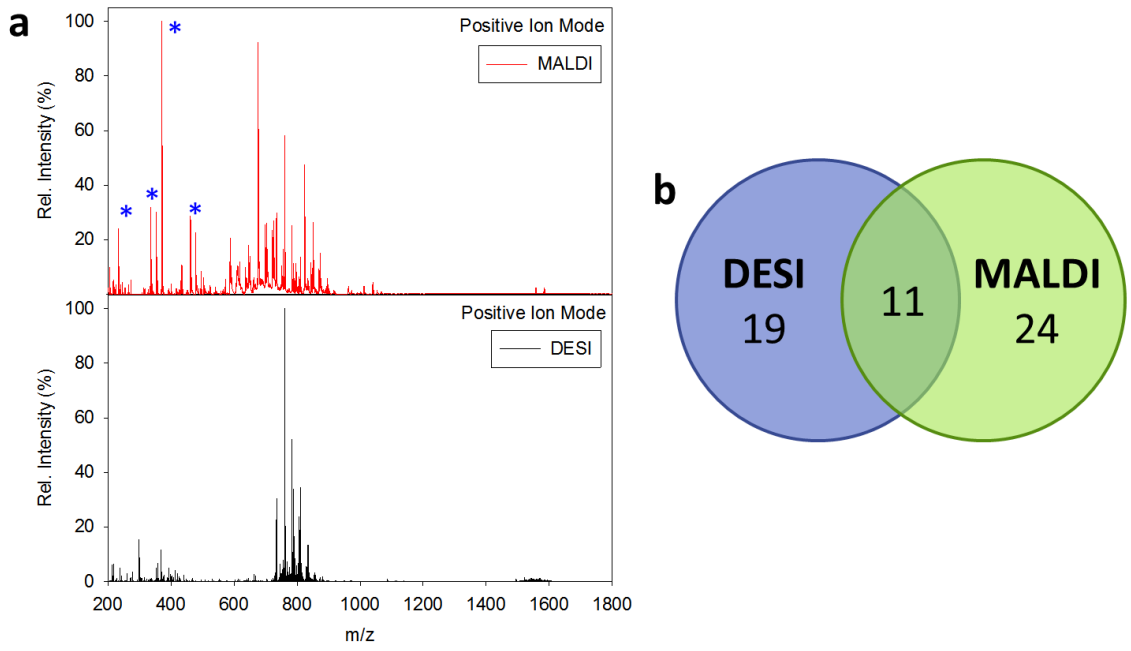

Figure 2.7. Representative spectra averaged across an entire tissue section in positive ion mode by MALDI- and DESI-MSI (a). Peaks corresponding to matrix clusters or chemical background are indicated with "*". A Venn diagram demonstrates the number of peaks detected exclusively by each imaging method and also the number of species detected for both MALDI and DESI (b).

The majority of the peaks detected in the low mass range by MALDI are known matrix clusters or background ions, but there are also a number of peaks in the 500-700 Da range that are exclusively detected by MALDI. These peaks were tentatively identified as lyso-PCs, ceramides or other sphingolipid species. The species detected in the 700-900 Da range were tentatively identified based on accurate mass and literature reports as PC and PE lipids;[82, 85, 148-150] these two lipids are among the most abundant phospholipids in the brain[176] and the amine group present in each makes them readily ionizable in positive ion mode. Full tandem MS to confirm these identities was restricted by the need for full MS/MS imaging of the entire tissue to discern overlapping signals and the limited number of tissue samples available. DESI-MSI exclusively detected a cluster of peaks in the 1500-

1600 Da range, which are likely phospholipid dimers. However, the signal-to-noise ratio prevented further characterization and ion images were too noisy to determine any specific spatial distributions. Ultimately, DESI facilitated detection of 19 unique spectral features, likely PCs and PEs in the 700-900 Da range, and MALDI detected 24 unique peaks (mostly with the 500-700 Da range), and 11 peaks were detected by both methods, all PCs (Figure 2.7b) which were confirmed by fragmentation and detection of the choline head group fragment.

In negative ion mode, DESI facilitated the detection of a much higher number of unique lipid species compared to MALDI (Figure 2.8). The spectra were acquired from washed tissues using methanol as the spray solvent for DESI-MSI and DAN applied by OCN spray deposition. Many phospholipids and sulfatides were detected by both MALDI and DESI, but DESI enabled the detection of various fatty acids (m/*z* 200-400) as well as possible diacylglycerols and phosphatidic acids (m/*z* 500-700). Again, lipid identifications were tentative and primarily based on database and literature searches.[148-150] The matrix peaks in MALDI and the fatty acid peaks in DESI (<400 Da) dominated the respective spectra, therefore the ion intensities observed in the 600-1000 Da mass window were scaled to better discern their presence.

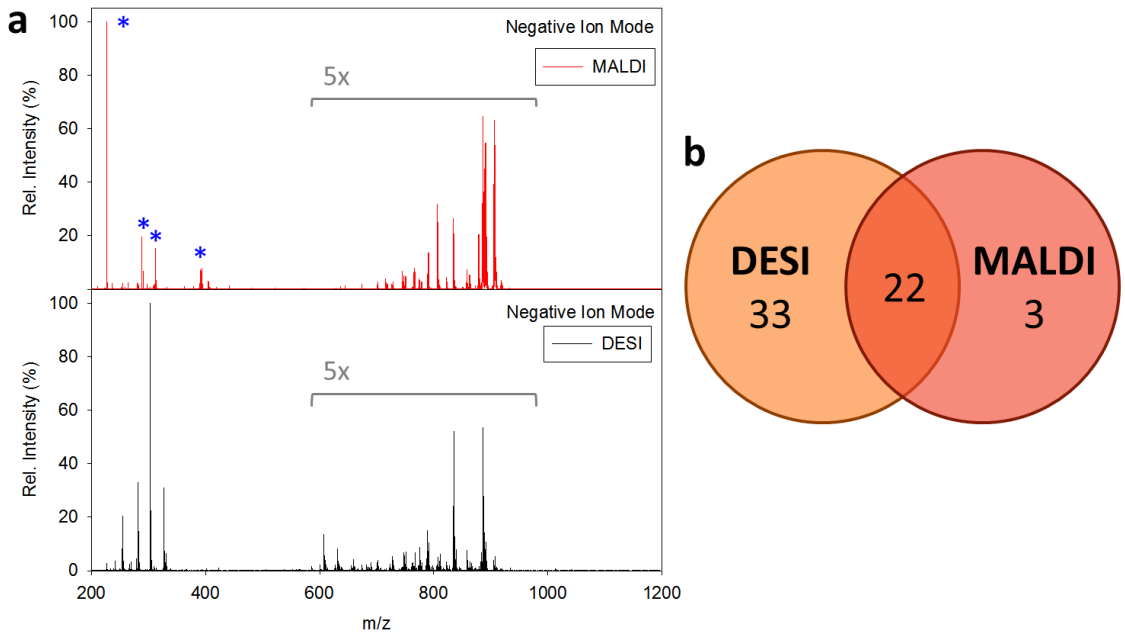

Figure 2.8. Average mass spectra acquired across entire brain tissue by MALDI- and DESI-MSI in negative ion mode (a). Peaks identified as matrix clusters or chemical background are indicated with "*". Ion intensities for m/z 600-1000 were multiplied by a factor of five to better visualize these significant lipid peaks. A Venn diagram demonstrates the number of peaks detected exclusively by each imaging method and also the number of species detected for both MALDI and DESI (b).

A surprisingly low number of unique peaks were detected by MALDI in negative ion mode (Figure 2.8b). To verify that this was not a consequence of tissue washing eliminating species more ionizable by MALDI, the peaks detected in the unwashed tissue section were also compared to DESI spectra. Several lipids detected by MALDI changed between washed and unwashed tissues, but additional peaks detected in the unwashed tissue were also detected by DESI. Therefore, for maximum chemical coverage, the washed tissues provide a greater number of unique lipid signatures.

These differences in lipid detection by MALDI and DESI may also be seen in selected ion images acquired on serial tissue sections shown in Figure 2.9. The pseudo-color scale in each ion image were set individually based on maximum intensity observed

for each ion. From these images, the advantage of DESI in its ability to detect and image fatty acids and phosphatidic acids is even more apparent. These particular species have been implicated in TBI and other types of injury from lipid peroxidation pathways,[156, 166] therefore DESI could become a powerful tool for the imaging of lipid peroxidation in TBI studies. In these experiments, the rat brain was injured by CCI in the upper left area of each ion image, and the observed changes in ion abundances are discussed below.

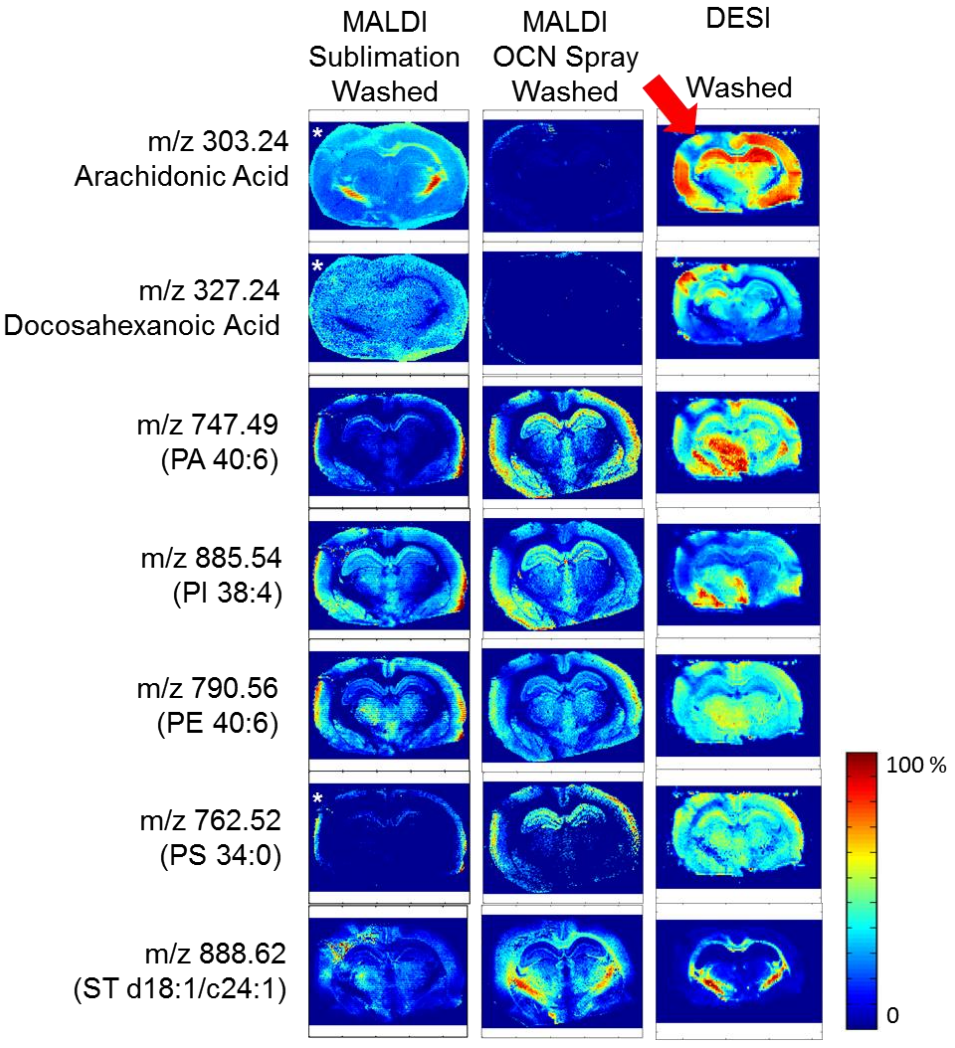

Figure 2.9. Select ion images acquired in negative ion mode by MALDI- and DESI-MSI. For comparative purposes, MALDI-MSI images are included following sublimation or OCN spray deposition of DAN. Several species were identified as chemical background based on higher ion intensity beyond the edges of the tissue and are indicated with "*". The site of the CCI is indicated with a red arrow.

2.4.5. Implications for Traumatic Brain Injury

Several lipid species detected showed clear changes in relative intensities in the cortical region of the brain at the site of the injury induced on the tissue by CCI. As previously discussed, arachidonic acid (m/z 303.2398, Δm = 6.8 mDa, 22 ppm) and docosahexanoic acid (m/z 327.2407, Δm = 7.1 mDa, 21 ppm) were detected exclusively by DESI-MSI (Figure 2.9). Arachidonic acid showed a decrease in intensity and the injury site whereas docosahexanoic acid showed an increase. Previous reports have shown that these fatty acids play a crucial role in the inflammatory response[156, 164] and are therefore expected to play a role in TBI where inflammation has been implicated as a secondary injury cascade.[177] Additional ions that showed changes in relative intensity at the injury site are shown in Figure 2.10.

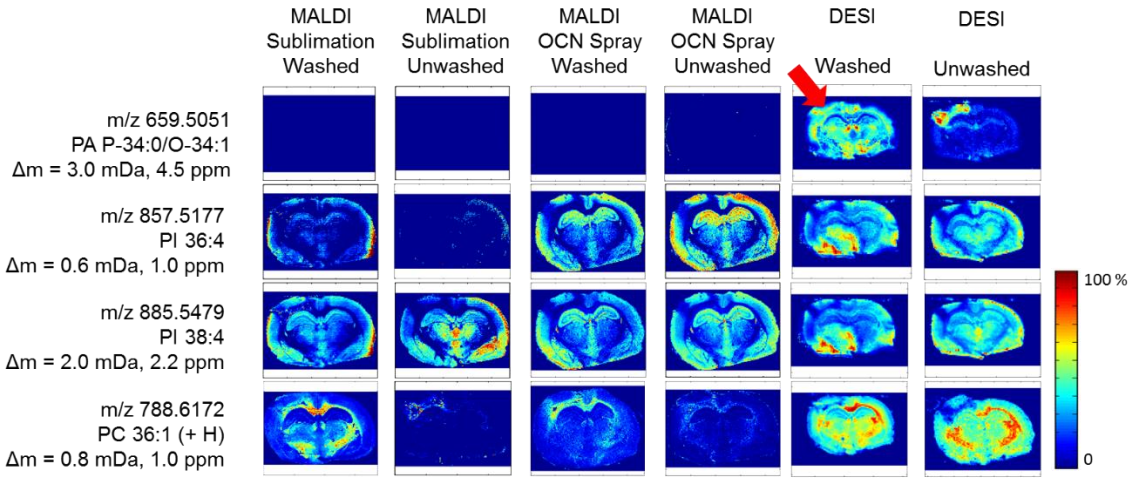

Figure 2.10. Examples of ion images that showed changes in relative intensity at the site of the TBI injury compared to the contralateral side of the tissue. Images are shown for the different sample treatment and MSI methods investigated in this study from serial sections. The site of the injury is indicated with a red arrow.

Flat impactors used in TBI studies, including this one, have been shown to cause the largest strain on the tissue and greatest damage along the impactor rim in a "fang-like" pattern.[178] This extreme damage is observed in the MSI data at the edges of the injury area and most clearly seen in the ion images for m/z 857.5177 in Figure 2.10. Extreme tissue degradation is expected in this region, therefore, only the center area of the injury was considered for the ROIs generated to compare lipid changes at the injury site; the extreme damage to this area may results in a loss of tissue that will create an artifact in fold changes because tissue densities will be different.[178]

Fold changes in ion intensity were calculated for every lipid species detected in this experiment as the average ion intensity observed in the injured tissue divided by the average intensity observed in a comparable tissue type on the contralateral side of the brain using ROI average spectra. Table 2.1 lists the fold changes for the lipid species shown in Figure 2.10; MALDI fold changes were calculated from the OCN matrix-deposited images. MALDI and DESI generally show similar increases or decreases for a particular species, except for the ion observed in positive mode with m/z 788.6172. This species was tentatively identified as PC 36:1 (Δm = 0.8 mDa, 1.0 ppm), however different spatial distributions are observed between DESI and MALDI (Figure 2.10), with DESI showing a higher relative abundance in the cerebral cortex than MALDI. The difference in spatial distributions suggests the ions detected by MALDI and DESI are unique species. Several PEs and PSs may also ionize to form species with m/z 788 in positive ion mode that inevitably complicate interpretation of the spectra. Tandem MS imaging of these precursors is necessary to discern the true identity of these species.

Table 2.1. Fold changes for select lipid species calculated from injured and contralateral tissue areas.

Tentative Identification	Average m/z	Fold Change			
		MALDI WASH	MALDI UNWASH	DESI WASH	DESI UNWASH
PA (P-34:0)/ (O 34:1)	659.5051	N/A	N/A	1.42	3.23
PI 36:4	857.5177	0.81	0.86	0.80	0.60
PI 38:4	885.5479	0.84	0.88	0.90	0.67
PC 36:1 (+ H)	788.6172	1.15	1.74	0.84	0.74

For a broader characterization of lipid changes resulting from TBI, average fold changes were calculated for multiple lipid classes, and are given in Table 2.2. At the time of this study, only one injured rat brain was available for imaging, therefore these fold changes should be considered preliminary. Therefore, additional samples would be necessary to define significant fold changes for lipid classes or individual species. In the future, we would like to acquire data for additional samples to confidently determine which lipid species are affected by TBI. Once these biomarkers have been found, complete identification of the analytes may be performed in a focused manner by MS/MSI. The conclusions made from continued investigations could then be used to guide metabolomics studies of TBI currently underway in parallel within our lab.

Table 2.2. Average fold changes observed for various lipid classes detected in this study. The combined fold change is average fold change for all tissue treatments and MSI methods.

	Average Fold Change				
Lipid Class	**MALDI Washed**	**MALDI Unwashed**	**DESI Washed**	**DESI Unwashed**	**Combined**
Phosphatidic Acid	1.15	1.64	1.73	0.95	1.37
Phosphatidylcholine	1.01	1.23	0.95	0.92	1.03
Phosphatidylethanolamine	0.77	0.82	1.10	0.86	0.89
Phosphatidylserine	1.27	1.09	0.95	0.78	1.02
Sulfatide	1.09	0.87	2.11	1.40	1.37

2.5. Conclusion

The effects of sample treatment and analyte extraction for DESI- and MALDI-MSI was investigated in order to maximize lipid coverage from brain tissues that have experienced TBI. Tissue washing with NH_4Form increased sensitivity for lipids in negative ion mode, and removed salts to shift ion formation to the protonated species in positive ion mode. When performed carefully, the integrity of the tissue is retained, which is critical for imaging purposes. Washing as a means of desalting is well characterized in the literature,[155, 165, 179] but I propose that the washing step alter the water content of the sample that ultimately affect analyte extraction for ionization. Further experiments to test this hypothesis include longer tissue drying times following washing or modeling of the mass transport between tissues wetted to different degrees.

Preliminary efforts to characterize changes in lipid species following TBI were somewhat inconclusive. MALDI and DESI showed similar fold changes for most species

investigated, but the small sample number (1) limits the conclusions that can be made. Future experiments in the study of TBI by these methods will involve imaging of more injured tissue samples as well as uninjured (sham and naïve) samples to confidently identify localized changes in biomarkers of TBI. Lipids of interest should then be characterized by tandem mass spectrometry imaging experiments to confirm molecular assignment.

MALDI and DESI have proven to complementary techniques for the detection of lipids in brain tissues. No one method stood out in terms of unique species detected, therefore in order to achieve full lipid coverage, both techniques would be required. Alternatively, based on these results, the appropriate protocol could be chosen for targeted lipid analysis.

CHAPTER 3. IMPROVING IMAGE CONTRAST IN DESORPTION ELECTROSPRAY IONIZATION MASS SPECTROMETRY IMAGING BY DIFFERENTIAL MOBILITY FILTERING

Adapted with permission from

Bennett, R. V.*; Gamage, C. M.*; Galhena, A. S.; Fernández, F. M., Contrast-Enhanced Differential Mobility-Desorption Electrospray Ionization-Mass Spectrometry Imaging of Biological Tissues. Anal. Chem. 2014, 86 (8), 3756-3763.

*equal contributing author

3.1 Abstract

Spray-based ambient MSI methods such as desorption electrospray ionization (DESI), eliminate necessary sample preparation and provide information-rich datasets, but typically suffer from lower spatial resolution and signal-to-noise than laser-based vacuum techniques. In order to fully take advantage of the benefits of ambient imaging, and to compensate for the somewhat limited figures of merit, a secondary orthogonal separation nested in the imaging scheme was implemented for more selective discriminatiob of tissue features in the spectral domain. Differential mobility spectrometry (DMS), an ion mobility-based separation that selectively transmits ions based on their high-to-low electric field mobility differences, can significantly reduce background chemical interferences allowing for increased selectivity. In this work, DESI DM-MSI experiments on biological tissue samples such as sea algae and rat brain tissue sections were conducted using fixed DMS compensation voltages that selectively transferred one or a class of targeted compounds. By reducing chemical noise, the signal-to-noise ratio was improved tenfold as well as doubling the image contrast, effectively increasing image quality.

3.2 Introduction

Both matrix desorption electrospray ionization (MALDI) and secondary ion mass spectrometry (SIMS) continue to excel in a variety of imaging applications,[129] mostly due to their high spatial resolution which is in the order of 50 μm and 5 μm, respectively. Vacuum MALDI also allows for the imaging of intact proteins, making it very appealing. However, MALDI suffers from high chemical background in the low mass region (m/z < 500) due to matrix ion signals and also requires additional sample preparation to apply the matrix. Therefore, ambient mass spectrometry imaging (MSI) methods are beginning to fill a niche where *in vivo* analysis and minimal sample preparation are desirable.

Although ambient MSI by desorption electrospray ionization (DESI) suffers from lower spatial resolution (50-200 μm) than MALDI, it still provides a convenient means to directly image complex surfaces with minimal sample preparation. If the spatial resolution afforded by DESI-MSI is sufficient for the desired application, it becomes an ideal technique for discovery purposes due high chemical diversity observed, especially for m/z < 1000 Da. DESI-MSI has shown to be a powerful tool for the imaging of exogenous drugs,[135, 180] metabolites,[139] disease biomarkers,[87] and lipids[80, 85, 133, 181] in biological tissues.

The spatial resolution of DESI images ultimately depends on the size of the solvent impact spot size.[109] It is therefore understandable that as image pixel size decreases, signal-to-noise ratio also will, as less material is desorbed and ionized. Lateral image resolution in the 100-200 μm range is routinely obtained with DESI, with the lowest reported resolution being 40 μm.[109] Attomolar detection limits have been obtained in specific cases involving DESI experiments with single-component samples on clean matrices,[92] but detection of low-abundance species in multicomponent biological systems can still be

challenging. In addition to the inherent complexity of biological samples, chemical noise stemming from the electrospray solvent, such as contaminants[174] or oxidation products, affects detection limits and spectral data. Event still, this chemical noise is still significantly less than the background observed in MALDI due to the ionization of matrix molecules and clusters. While the currently-reported DESI-MSI figures of merit are suitable for many applications without further refinement, the incorporation of nested orthogonal separation dimensions for particularly-complex samples could offer additional benefits.[182] In the context of MSI, a nested separation may provide a means by which to improve image quality in such a way that sensitivity is not sacrificed for improved image resolution and contrast.

Given the data acquisition time (0.5-1 s) required for each pixel in a DESI-MSI chemical image, any nested orthogonal separation must be rapid enough to avoid reducing analytical throughput. Ion mobility-based separations are therefore ideal for augmenting imaging experiments, as they can be achieved in the millisecond time scale. Classic ion mobility techniques such as drift tube ion mobility spectrometry (DTIMS) and traveling wave ion mobility (TWIMS)[183] have been used for MSI applications in combination with MALDI-MS, providing rapid separations prior to MS analysis.[132, 184-187] The somewhat limited resolving power of TWIMS and reduced pressure DTIMS suggest that further improvements in nested MSI techniques are further required for ambient MSI methods.

In contrast to DTIMS and TWIMS, differential mobility spectrometry (DMS) acts as an ion filter based on ion mobility differences in alternating high and low electric field conditions.[188] Ions are transported between the two plates of the DM cell (Figure 3.1) by a carrier gas (most often nitrogen) under alternating high and low electric fields generated

from the application of an asymmetric radio frequency (RF) waveform to one of the plates. The difference in ion mobility at high and low-field is compound-specific and leads to ion drifts in the y-dimension between the DM cell plates. By applying a direct current (DC) "compensation" voltage (V_c), in addition to the RF waveform, the trajectory of ions with a particular low-to-high field ion mobility ratio can be made stable so that they are selectively transmitted with no net drift; all other ion types are eliminated as they collide with cell plates.[189-191]

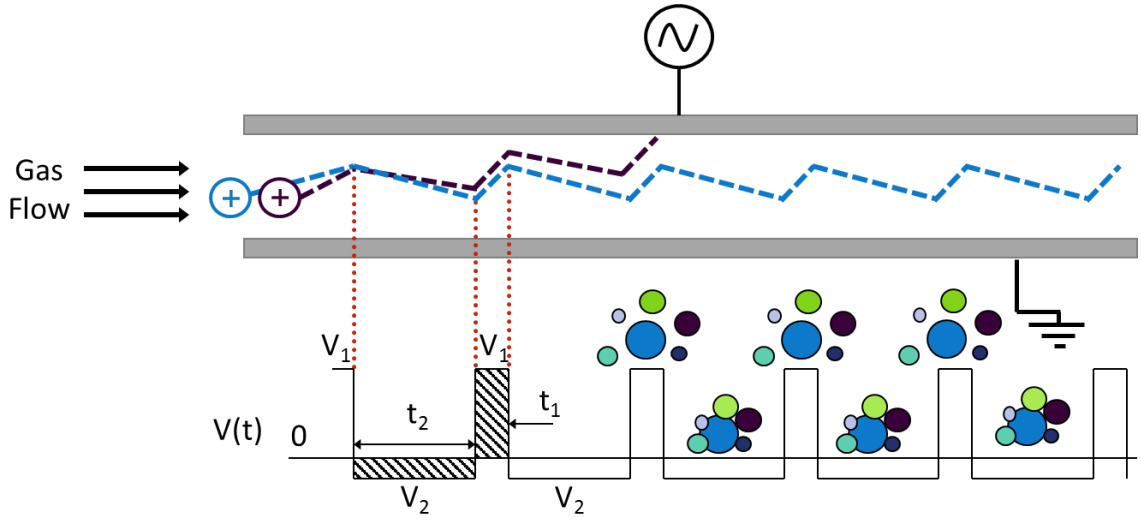

Figure 3.1. Schematic of planar differential mobility cell showing motion of ions between plates as a function of applied potential.

With a mode of operation that resembles ion selection in a quadrupole mass filter - sweeping or constant V_c - the duty cycle of DMS is significantly higher than atmospheric pressure gated ion mobility methods and can approach 100% for targeted analysis.[192] In addition to the benefit of increased duty cycle, DMS also shows a higher degree of orthogonality to MS relative to DTIMS due to its non-linear separation principles.[193]

In classical ion mobility, ions are separated based on collisional cross section as a result of collisions between the ions and neutral drift gas. These interactions are consistent

throughout the entire analysis due to the constant potential gradient applied. However, in DMS, the nature of these collisions are constantly changing as a function of the alternating high and low electric field. Several models have been proposed to explain the separation of ions under varying field strengths including the rigid sphere scattering, long-range ion-dipole attraction and clustering models.[194] The most widely accepted of these is the clustering model. The clustering model proposes that ions are clustered with neutral gas or other analyte molecules when traveling under a low electric field, and the ions become de-clustered under high field.[195] The energy involved in the formation and dissociation of the clusters is highly dependent on the chemical interactions between the ion and the neutral gas phase molecules.[194] As the degree of ion clustering changes, the effective collisional cross section of the ion changes, thus changing the nature of the collisions with the surrounding gas molecules. This amplifies the difference in mobility characteristics of an ion because it depends on not only on the collisions with the gas, but also the constantly-changing clustering. Careful control of the chemical environment can be used to tune clustering during analysis for greater separation of ions resulting in improved resolution and peak capacity.[195] For this reason, alternative gases (i.e. helium, argon, mixtures with nitrogen)[196-198] or organic modifiers[195, 199-200] are used in the carrier gas for enhanced separation.

DMS also readily operates under ambient conditions and is conveniently coupled to existing mass spectrometers and ambient ion sources. In non-imaging experiments, DM-MS has shown to improve peak capacity, increase signal-to-noise (S/N) ratios,[201-202] and significantly shift target signals away from crowded spectral regions.[199, 203] The separation power and many benefits of DM separations have been effectively leveraged for a wide

variety of applications,[204] including the separation of isotopes[205] and stereoisomers.[203] In earlier work, the Fernandez lab reported proof-of-principle results on the operation of a DESI DM-MS platform for surface sampling purposes, demonstrating the advantages of DMS filtering in ambient small-molecule analysis.[202] However, the use of DM-MS for ambient MSI of biological tissues had yet to be explored. This study was the first application of DESI DM-MS to targeted biological tissue imaging, taking advantage of the aforementioned improvements in signal-to-noise ratio leading to better image contrast, quality and detail.

3.3 Experimental Details

3.3.1 Chemicals and Samples

Acetonitrile, methanol and isopropanol (OmniSolv® LC-MS grade) were purchased from EMD Millipore Corporation (Billerica, MA, USA). Acetic acid (ACS Reagent grade, ≥ 99.7%) and 4-hydroxybenzoic acid (≥ 99%) were purchased from Sigma-Aldrich (St. Louis, MO, USA). Sea algae samples (*Halimeda -incrassata*) were collected in shallow seagrass beds adjacent to Rodriguez Key or Pickles Reef, Key Largo, Florida, USA. Flash-frozen rat brains were sectioned using a CryoStar* NX70 Cryostat (Thermo Scientific, Kalamazoo, MI, USA) with a sample and blade temperature of -25 °C. Tissues were sectioned with a thickness of 18 μm and were thaw-mounted on glass microscope slides (VWR, Radnor, PA, USA). Slides were stored at –80 °C until the time of analysis, at which point, tissues were allowed to thaw at room temperature inside a vacuum chamber (Vacuum Sample Saver™, VWR, Radnor, PA, USA) for 20 minutes.

3.3.2 DESI DM-MSI Instrument

Figure 3.2 illustrates the major components of the DESI ion source and DMS interface to the time-of-flight (TOF) mass spectrometer (JEOL AccuTOF, Tokyo, Japan). Gas phase ions were generated by a home-built DESI probe (Figure 3.2 parts 1-4)[78, 202] that consisted of a coaxial inner spray capillary (150 μm o.d., 50 μm i.d.) and outer nebulizer gas capillary (350 μm o.d., 250 μm i.d.). Both capillaries were made from fused silica tubing (Polymicro Technologies, Pheonix, AZ). A nitrogen-assisted (150 L h^{-1}, ultra-pure, Airgas, Atlanta, GA, USA) high velocity DESI spray composed of 1% acetic acid in acetonitrile was used for rat brain tissue imaging, and methanol was used for the analysis of sea algae samples. The DESI solvent was delivered at a flow rate of 5 μL min^{-1} using a syringe pump (Fusion 100, Chemyx, Inc., TX, USA). The spray probe was floated at 3.6 kV using a DC power supply (PS325 DC, Stanford Research Systems, Inc., CA, USA). Source geometry was optimized for sensitivity, with a distance of 2 mm between the spray tip and the sample surface at an angle of 55°. The separation between the source sprayer and capillary inlet of the mass spectrometer was 4 mm.

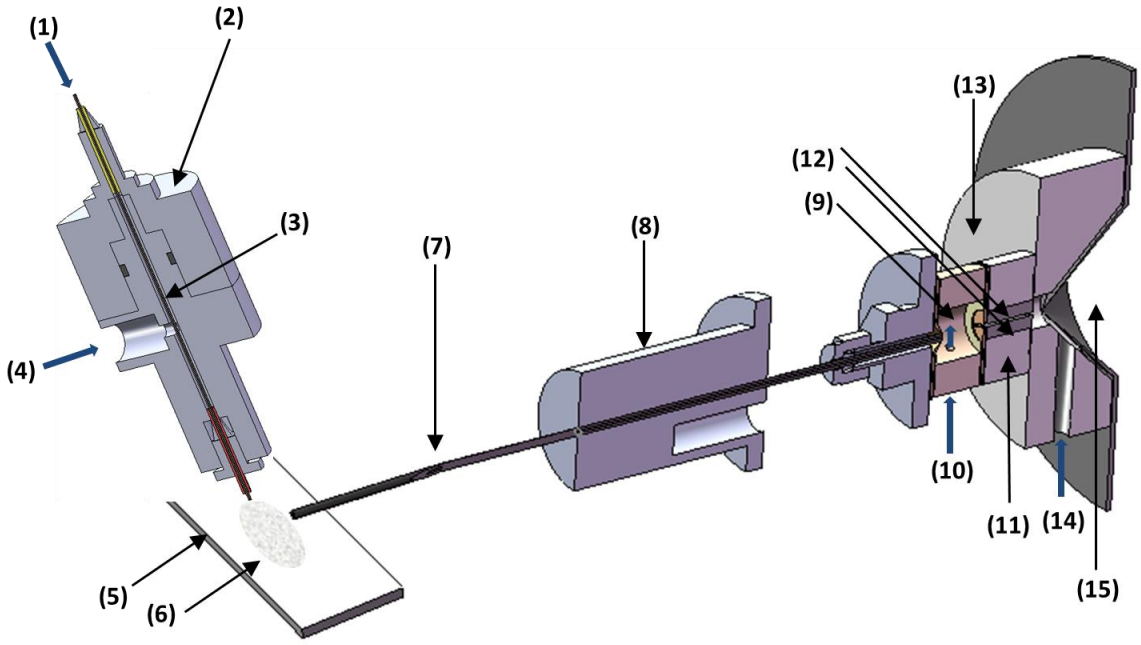

Figure 3.2. Schematic of DESI DM-MS interface used for imaging. (1) DESI solvent inlet, (2) DESI probe, (3) solvent capillary, (4) DESI gas port (N_2), (5) glass slide, (6) sample, (7) heated capillary, (8) heating block, (9) desolvation chamber, (10) DMS carrier gas (N_2) and dopant inlet port, (11) DMS electrode support, (12) DMS electrodes, (13) DMS assembly holder, (14) throttle gas port, (15) mass spectrometer orifice inlet.

Charged secondary droplets containing analyte ions resulting from the DESI microextraction process were collected by a stainless steel capillary (250 mm long, 1.58 mm o.d., 0.6 mm i.d.). The capillary was held at ground and heated to 200 $^{\circ}$C by a rope heater (OMEGALUX®, Omega, Stamford, CT, USA). Ions were introduced from the transfer capillary into the desolvation chamber through a custom-fitted brass washer. This washer controls the distance that the transfer capillary penetrates into the desolvation chamber (1 mm). Nitrogen was supplied to the desolvation chamber (0.2 L hr^{-1}), thus adding to the overall flow of DM carrier gas.

The gas stream carrying ions then enters the DMS cell through another brass washer with a slit opening aligned with the gap between the DM cell electrodes. The DM cell was

built from a modified microDMx differential mobility sensor (Sionex Corporation, Bedford, MA) comprising a rectangular gap (10 mm long x 8 mm wide x 0.5 mm spacing) created by two parallel metal plates. The PEEK DM assembly holder mounts the entire transfer capillary and DMS module to the orifice 1 plate of the TOF mass spectrometer. The assembly holder was furnished with a side port for throttle gas introduction (ultra-pure N_2, Airgas, Atlanta, GA, USA) at an optimal flow rate of 0.7 L min^{-1}. Throttle gas was necessary to offset the pull of vacuum from the mass spectrometer orifice, thus increasing ion residence time in the DM cell. All components of the DESI DM assembly were joined and sealed using Gore-Tex washers to prevent gas leaks thus enhancing ion/droplet transport through the system.

The high-frequency RF waveform was applied as a clipped sinusoidal waveform operating at a constant frequency of 1.25 MHz. The maximum applicable RF voltage amplitude (V_{rf}) was 1500 V, limited by the control system and power supplies. For sea algae images collected in negative DESI ion mode, the combination of V_{rf} = 500 V and compensation voltage (V_c) = -1.1 V was used for DM filtering. In contrast, brain tissue imaging performed in positive ion mode used V_{rf} = 1500 V and V_c= 5.3 V for filtering of lipid species. These voltages were selected based on minimum mobility peak width and maximum sensitivity for analytes of interest obtained during preliminary V_c sweeps and tuning. For comparison purposes, images were collected in both the "DM-on" and "DM-off" modes. For brain tissues, the DM-off mode was operated with the voltages on the DM electrodes turned off. For the algae tissues, higher sensitivity was observed in the control images when the DM-off mode was operated with no V_c, but with V_{rf} = 500 V. Increased ion transmission at low V_{rf} settings has been reported previously for other low-molecular

weight analytes.[206] This mode was exclusively used for comparison purposes. In order to maximize ion transmission and sensitivity, the following mass spectrometer parameters were used: orifice 1 = 95 V, ring electrode = 8 V, and orifice 2 = 8 V.

3.3.3 Imaging Procedure

Microscopic glass slides used to support tissue samples were mounted on a motorized microscope stage (OptiScan II, Prior Scientific, Inc.) controlled by an in-house written VI using LabView version 7.1. The sample stage was moved using a "comb-shaped" raster path which, briefly, consisted of unidirectional line scans with line stepping.[171] The stage moved at a speed of 160 μm s^{-1} in the x-dimension and the line step in the y-dimension was 200 μm. Mass spectra were acquired on the AccuTOF at a rate of 1 spectrum per second for the mass range of m/*z* 100-200 and 700-900 for algae and brain tissues, respectively. These motion parameters were chosen based on the DESI spray impact spot size and resulted in an overall pixel size of 160 x 200 μm. Image data were processed using omniSpect, an open-source, MATLAB-based software capable of visualizing selected m/*z* images and performing statistical analysis such as non-negative matrix factorization to identify component images.[171]

3.4 Results and Discussion

3.4.1 Sea Algae

As a first test case of the performance of the DESI DM-MS system for MSI applications, chemical images were obtained for the distribution of 4-hydroxybenzoic acid (4-HBA, M_w=138.03), a naturally occurring chemical in marine algae known to play a role

in inter-species communication, such as herbivore host plant recognition.[207-209] By studying the spatial distribution of 4-HBA on algal surfaces a better understanding of its biological role as an ecologically-relevant chemical cue can be obtained.[210-211] 4-HBA was first detected in *Halimeda incrassata* through bulk extraction and analysis by collaborators, which then prompted surface analysis by DESI-MSI. Preliminary imaging by DESI-MSI, with the DM unit in the "DM-off" mode indicated the presence of 4-HBA on the algae tissue surface. Figure 3.3a shows a sample mass spectrum obtained from the algae surface during the control experiment with no V_c applied. The peak observed at m/*z* 137.0255 corresponds to the $[M-H]^-$ ion of 4-HBA (Δm = 1.6 mDa, 11 ppm), and S/N = 8; this peak is present, but hardly noticeable above the baseline noise. Figure 3.3c shows the optical image of the algae sample analyzed and the corresponding chemical image for m/*z* 137 obtained in the DM-off mode is shown in Figure 3.3e. Faint pixel clusters indicate the presence of 4-HBA on the algae surface, however, the poor image contrast prevents the accurate assessment of the spatial distribution of this chemical of key ecological importance.

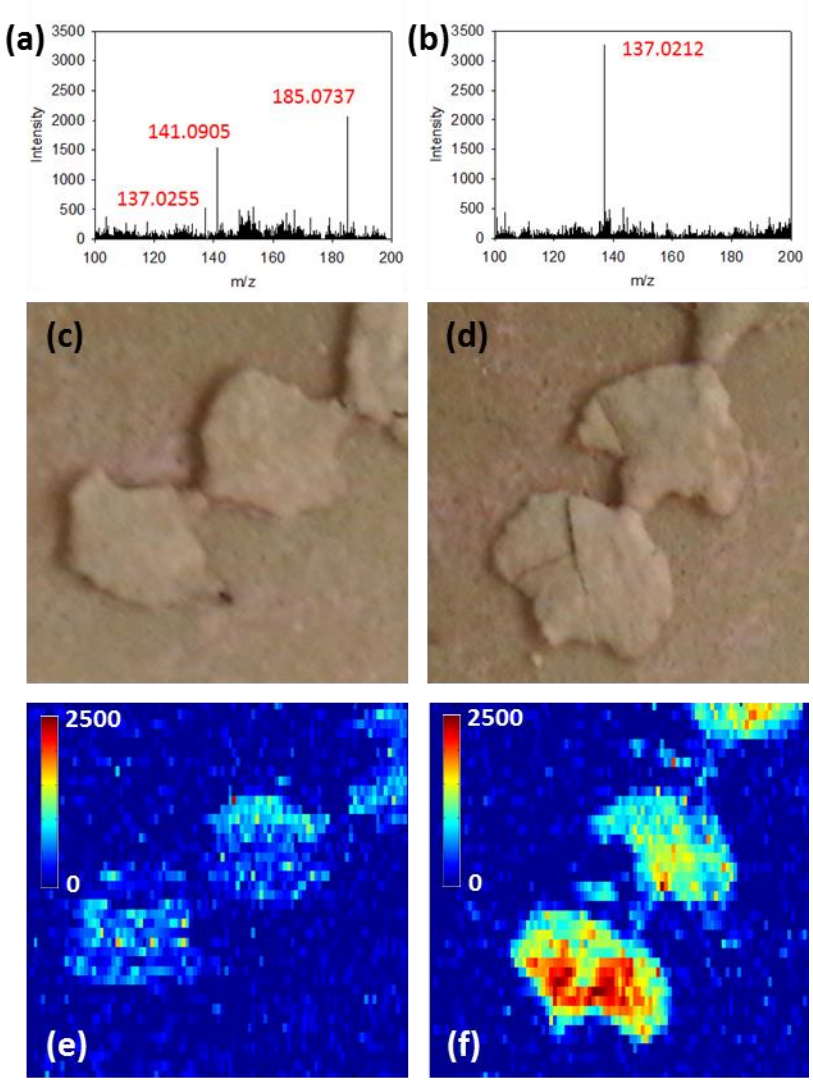

Figure 3.3. Results for targeted imaging experiments of 4-hydroxybenzoic acid ($[M-H]^-$, m/*z* = 137) on the surface of *Halimeda incrassata* tissues. DESI spectra and images were obtained with DMS voltages off (a and e) and DMS voltages on (b and f), respectively. Mass spectra (a and b) were extracted from the respective imaging experiments and represent a single pixel within the image. Optical images of the algae are shown above each chemical image (c and d) for reference purposes.

In order to enhance the detection of 4-HBA on the algae surface, the DMS unit was used to reduce chemical background signals. DMS voltages were optimized by sweeping the compensation voltage as a standard solution of 4-HBA was continuously. A compensation voltage of -1.1 V was found to most effectively filter out chemical

background and more selectively transmit the 4-HBA ion. The improvement in signal to noise for the detection of 4-HBA is best seen in the mass spectrum obtained from the algae surface during an imaging experiment with DM-on conditions (Figure 3.3b). In this scenario, 4-HBA was the only species detected above baseline by the mass spectrometer in the m/*z* window 100-200, all previously-observed extraneous signals were eliminated. The absolute spectral intensity of the $[4\text{-HBA} - H]^-$ ion was six times larger in the DM-on case. Based on our previous studies,[211] order of magnitude variance in the average metabolite surface concentration is not expected between anatomically similar regions of algal blades or fronds. Therefore, the primary factor responsible for the observed enhancement in ion transmission can be attributed to the application of the optimum V_c. The spectrum was noticeably improved with a S/N of 54 for m/*z* 137, approximately a 7-fold increase. This increase in S/N using DMS post-ionization separation translates into an increase in the contrast (from 10.75 to 31.35) observed in the chemical image for 4-HBA (Figure 3.3f). The image contrast was calculated using ten image rows across several algae leaves and the average contrast was calculated using Weber's definition.[173] This definition is most often used when the background is consistent across the multiple samples used for the calculation.[173] This is the case with the algae images because the area outside the algae is the same substrate. Not only does it become clearer that 4-HBA is present on the surface of *Halimeda incrassata*, but changes in abundance across the surface of the algae are better described, facilitating more specific correlations between spatial distribution and biological function. 4-HBA was observed on the outer-most leaf of the algae stem, where it is closest to other species for possible chemical-based signaling.

3.4.2 Brain Sections

In order to demonstrate the potential of imaging even larger biomolecules (> 500 Da) with this MSI platform, lipids, specifically phosphatidylcholines (PCs), were imaged in rat brain tissue samples. PCs observed in these tissue sections were detected with m/*z* values ranging from 700 to 900 Da. Additional tuning of the DMS unit was performed for this target lipid family directly on brain tissue. The compensation voltage was scanned from 2-10 V (V_{rf} =1500 V) in 2-minute cycles for 110 minutes while the sample stage moved continuously resulting in >6600 data points. A boxcar moving average (50 data points) was then used to smooth the data in order to account for spatial variability in ion abundance on tissues and ultimately determine optimal DMS conditions. Averaged intensities for primary PC signals as a function of V_c sweep are shown in Figure 3.4. Maximum lipid transmission of all PCs with minimal chemical noise was achieved with a V_{rf} = 1500 V and V_c = 5.3 V.

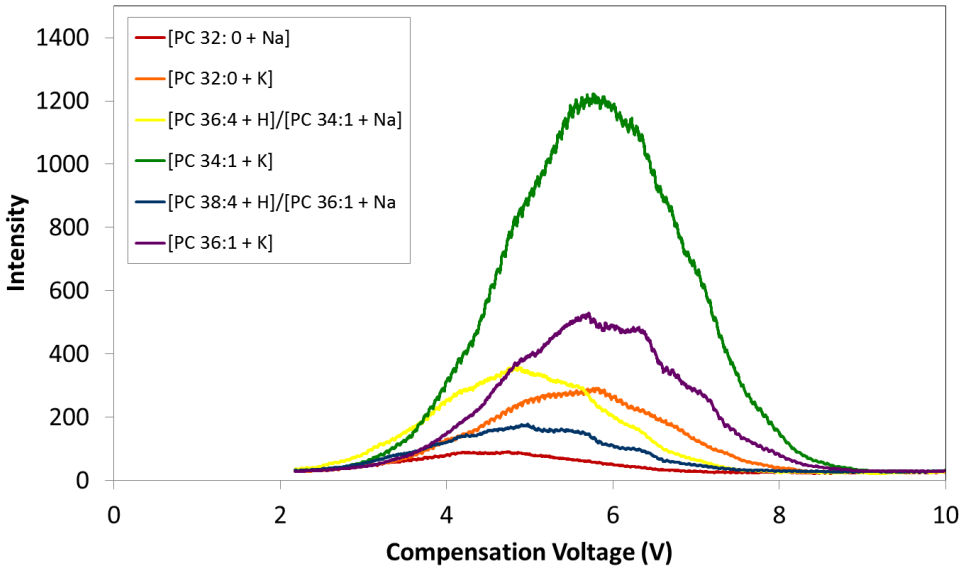

Figure 3.4. Averaged intensity of primary PCs during V_c sweeps acquired directly on brain tissue section.

After optimizing the DMS unit settings on the suite of PCs present in biological tissue, the resolution in the mobility dimension, defined as the ratio between the peak width at half maximum and the compensation voltage at which the peak is observed, was calculated using a lipid standard solution (PC 36:2) and was found to be 2. The resolution of this particular DM unit is greatly limited by a short (10 mm) cell length, limited V_{rf} in the driving electronics, and the use of a carrier gas without solvent dopants or He gas.[196, 200] This resolution alone is insufficient for complete separation of large biomolecules within the same class that generally display wide mobility profiles due to molecular flexibility affecting their three dimensional structure.[197] Resolution in DMS can be further improved changing carrier gas composition (type of gas used and solvent modifiers)[196, 199-200, 212] or the dimensions of the DMS unit (increased length, reduced gap).[199] Shvartsburg *et. al* have demonstrated the ability to separate classes of lipid species using He/N_2 carrier gas mixtures and a different DMS cell geometry than that used here.[197] Despite the ability of helium to increase separation and peak capacity, previous experiments with the specific DM cell used in this study resulted in reduced sensitivity.[202] Therefore, for the quasi-targeted analysis of lipids in biological samples, N_2 was used as the carrier gas in order to maximize detection of low-abundance species. Even still, the PCs of interest were successfully separated from background spectral noise that includes solvent contaminants and other classes of endogenous species present in tissue such as peptides and other metabolites in the studied mass range.

Figure 3.5a shows an average mass spectrum obtained from a rat brain tissue section image with the DM unit operated in the transparent "off" mode. The major PC

species observed were tentatively identified by comparing accurate masses with previously reported data.[140] Figures 3.5b and c show zoomed DM-off and on mode mass spectra, respectively, obtained at two identical spatial coordinates of two adjacent brain tissue sections expected to have comparable chemical composition. The DM-on mass spectrum shows a marked reduction in low-abundance species and chemical noise compared to the DM-off mode. The baseline noise is decreased by 52%, resulting in a two-fold improvement in S/N. Compared to algae surfaces, brain tissues contain a much greater number of concomitant chemical species in the mass range of interest that could complicate MSI analysis. Although the observed increase in S/N is lower for the brain tissues versus the algae, this increase is still sufficient to significantly reduce spectral complexity and increase image quality.

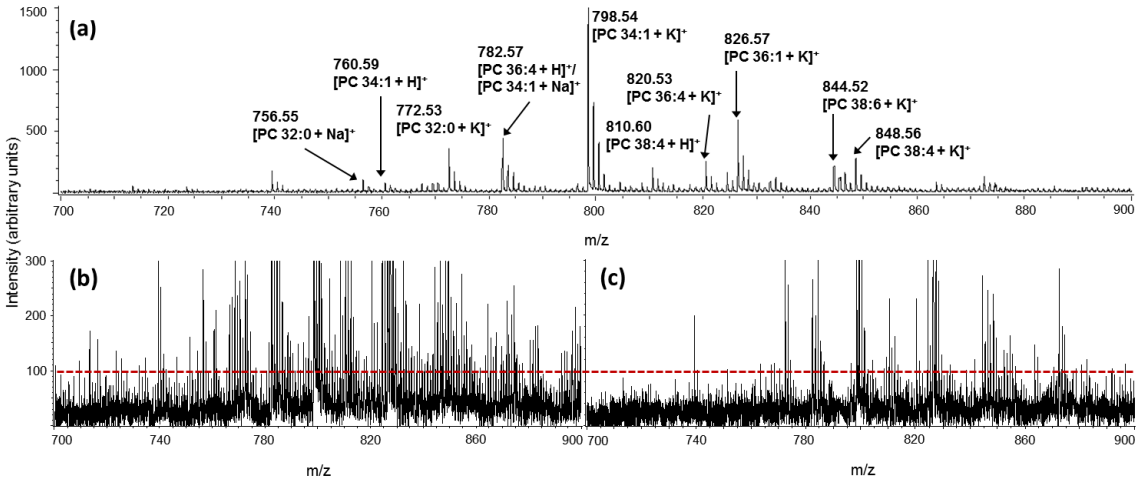

Figure 3.5. (a) Averaged DESI mass spectrum obtained from the DM-off mode MS image of a rat brain tissue section. Baseline detail of single DESI mass spectra in the 700-900 m/*z* range obtained from equivalent areas of two rat brain tissue sections imaged with DM-off (b) and on (c) settings. The y axis is scaled equally in (b) and (c) for comparison purposes; the horizontal dashed line indicates an intensity = 100 for both experiments. The DM unit was operated at a compensation voltage of 5.3 V for optimum detection of major PC species.

To demonstrate the effect of DM filtering on brain tissue chemical images for specific species, the selected ion image at m/z = 782 ($[PC\ 36:4+H]^+$ / $[PC\ 34:1+Na]^+$) is shown in Figure 3.6. These lipids were identified based on accurate mass and literature comparisons; $[PC\ 36:4+H]^+$ Δm = 2.9 mDa, 3.7 ppm, $[PC\ 34:1+Na]^+$ Δm = 5.3 mDa, 6.8 ppm. Images were acquired on serial tissue sections with DMS voltages off (a) and on (b). All other instrumental conditions were kept identical. Both DESI-MSI images provide sufficient spatial detail to conclude that this PC is mainly distributed in the white matter portion of the tissue. However, the image acquired in DM-on mode shows a more homogeneous distribution of the PC species in these areas, which is expected given that it is composed of the same tissue type.[80] Additionally, the boundaries at the edges of the white matter regions are more regular and well-defined, and features not discernible from background noise in DM-off mode are clearly visible in DM-on mode. Weber's definition of contrast can again be applied to the tissue samples as PC 36:4/PC 34:1 is expected to have consistent distributions in the cerebral cortex which was used for the background signal. The average contrast for m/z 782 was calculated using seven image rows with equal tissue composition in the right third of the respective images (area outlined in white in Figure 3.6) and was found to be 1.87 in DM-on mode, which compared favorably with 0.98 in DM-off mode, nearly doubling the image contrast.

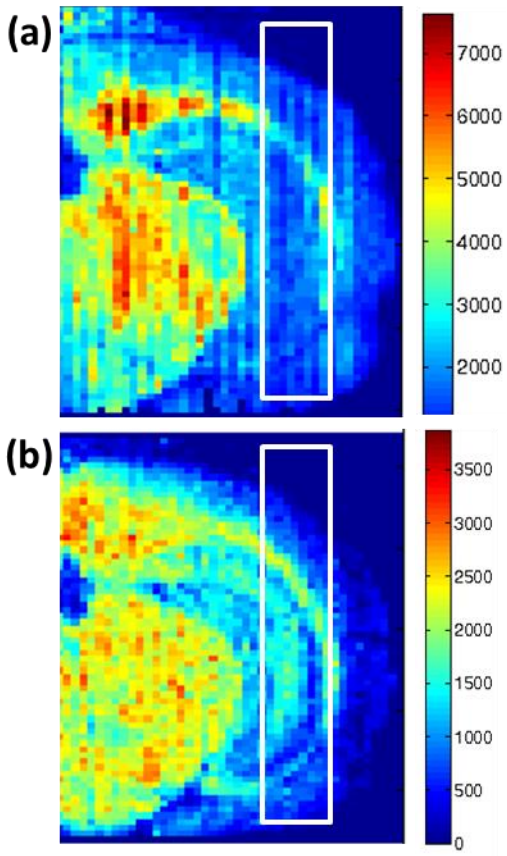

Figure 3.6. Rat brain tissue images for the PC at m/*z* = 782 obtained in DM-off (a) and on (b) modes. The area used for average contrast calculations in outlined in white. The absolute intensity pseudo-color scale has arbitrary units.

The maximum signal observed is significantly different between the two imaging modes naturally affecting the image contrast. The average maximum signal intensity observed in the tissue images acquired in DM-off mode for m/*z* 782 was 2727 counts compared to a maximum intensity of 1944 counts in the DM-on mode for the corpus callosum shown in Figure 3.6. Considering that the two tissues sections used in these experiments were adjacent, they can be considered biologically identical. Therefore the 31% decrease in ion intensity can be attributed to two factors not related to the sample itself: (a) diffusional loses that occur during the DMS separation process and (b) the voltage

of the selected V_c that is considered optimal for a group of species in contrast to a V_c selected for one individual analyte. Diffusional losses up to 20-30% have previously been observed for planar DMS cells,[213-214] which is ultimately dependent upon the residence time of the ions in a high electric field. Variables effecting ion residence times can be tuned for maximum transmission; however, increased transmission has been shown to come at a cost of lower resolution.[214] Alternatively, cylindrical high field asymmetric waveform ion mobility (FAIMS) cells have higher transmission efficiencies than their planar counterparts.[213]

The second type of loses, particularly relevant for DM-on mode, relate to the broadened peak shape observed for a given species when the RF field is applied.[215] This diffusional peak broadening becomes beneficial when attempting targeting multiple species for imaging with a single compensation voltage. The RF-induced peak broadening generates a greater overlap among species, facilitating the use of a single, compromise V_c value that can be used to enhance detection of multiple analytes. The PC species studied here showed maximum transmission for V_c values ranging from 3.5-5.5 V. Although the selected optimal V_c of 5.3 V did not correspond to an optimum value for any specific analytes, it was a compromise that still allowed for detection of all of them with reduced background noise. Because the background signal is reduced to a greater extent (52%) than the analyte signals, the noise reduction is a result of the DMS filtering effect, not simply diffusional loses. Despite loses observed for analytes of interest, which are comparable to previously reported loses observed during DMS analysis,[213-214] it is the significantly larger reduction in chemical noise that results in improved image contrast.

Individual biomolecules can be used as markers of disease or other alterations, but diagnostic accuracy is generally increased by considering marker panels.[216] In this line of thought, chemical images constructed with a combination of chemical species instead of a single ion can reveal higher-level phenomena and relationships not easily observable through single m/*z* images. Statistical methods such as principal component analysis (PCA)[217] or non-negative matrix factorization (NMF)[171] are frequently used to identify significant combinations of chemical species in MSI. As DM filtering improves the chemical contrast of detected species, it could also yield image enhancements while multiple lipid species are considered in multivariate space.

For example, when two-component NMF calculations were performed on rat brain chemical images using the built-in function within omniSpect,[171] white and grey matter regions are clearly separated (Figure 3.7), without any *a priori* knowledge of the most relevant lipid markers contributing to those regions. When considering all ions that contribute to a particular tissue type, DM filtering provides a clear visual improvement of image features compared to the DM-off imaging mode (Figure 3.7a-b). As shown in the corresponding component mass spectra, DM filtering significantly decreases interfering signals and chemical noise. These spectral changes result in increased contrast and more defined grey matter/white matter boundaries in the DM-on mode component images. The combination of NMF analysis to computationally identify relevant ionic species made more evident by DM filtering promises to become an important element in the ambient MSI toolbox for the investigation of complex biological systems. Following this clustering data processing, the user may then optimize analytical parameters for targeted DESI-DM-MSI analysis of key markers.

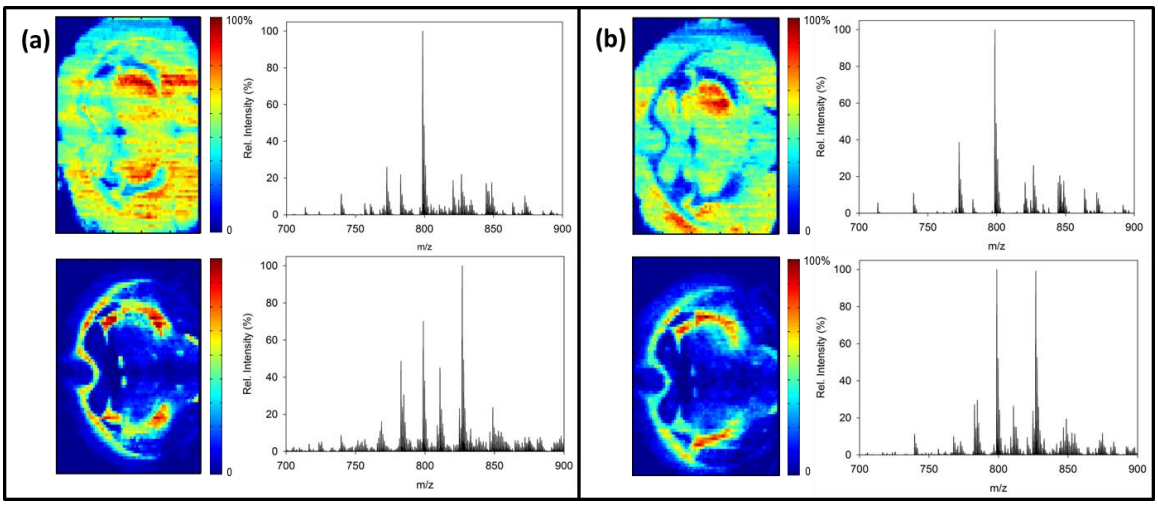

Figure 3.7. Two-component NMF analysis results for rat brain tissue sections imaged by DESI without (a) and with (b) DM filtering. Data in the top and bottom rows show the first and second NMF components, respectively. The corresponding component mass spectra are displayed to the right of each component image.

3.4.3 Carrier Gas Modifiers for Improved Separation

Preliminary experiments were conducted to study the effect of carrier gas modifiers on PC separation. Organic solvent modifiers were introduced into the carrier gas stream via controlled syringe injection. Of the modifiers and concentrations tested, isopropanol introduced at a flow rate of 3 μL min^{-1} gave the best enhancement, albeit moderate. The separation of PCs acquired during optimization of DM voltages with isopropanol as the modifier is shown in Figure 3.8. Again, the DM compensation voltage was scanned from 0-8 V (V_{rf} = 1500 V) while continuously sampling directly from brain tissue. Data was smoothed using a boxcar moving average (50 data points) to account for spatial variability in ion abundance on tissues. The addition of isopropanol into the gas stream begins to

separate sodiated PC adducts from protonated and potassiated adducts. This separation is beneficial for the selective detection of lipids, which is frequently complicated by overlapping signals from different lipid adducts; for example an ion observed for m/z 782 could correspond to $[PC\ 36:4+H]^+$ or $[PC\ 34:1+Na]^+$. Currently tandem mass spectrometry is required to distinguish these species, or as previously discussed, tissue washing is also an effective means for reducing salt adduct formation.[155] However, separation of these isobars by DMS would accomplish the same goal without disturbing the sample from washing while also allowing for broader chemical detection of entire lipid adduct classes without the need for single precursor ion selection.

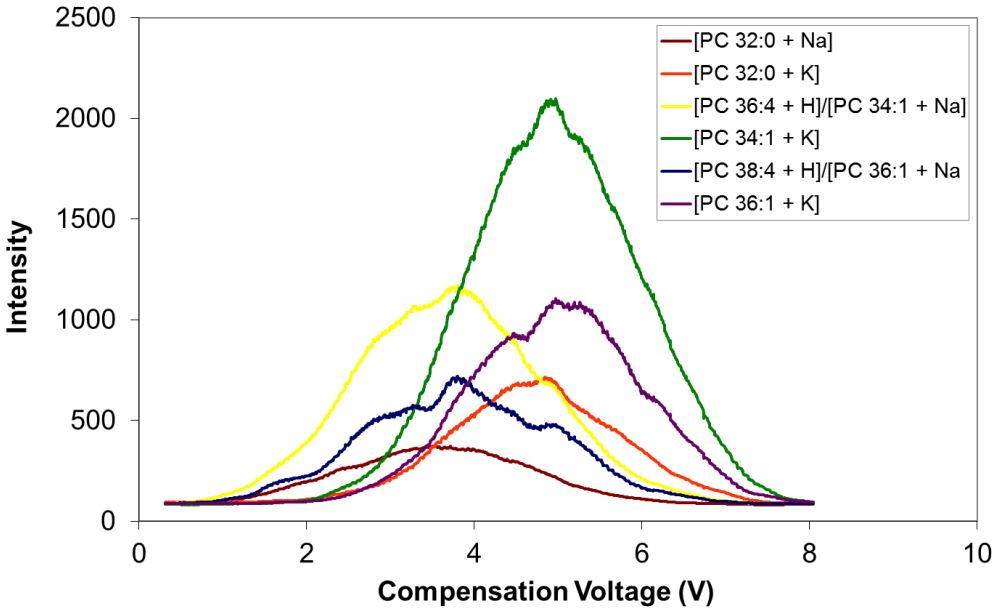

Figure 3.8. Averaged intensities of PCs separated by DMS with the use of isopropanol as a carrier gas dopant. Data acquired directly on tissue sections and averaged using a moving box car average. Data suggests potential of separating species based on adduct ion.

The use of dopants in imaging experiments were limited due to inconsistent vapor-phase introduction of the modifier throughout the entire imaging experiment (~3 hours). Initially, dopants were introduced through a tee junction, first with a small (0.57 μL) then a larger (2.1 μL) swept volume, but the solvent was not efficiently vaporized and quickly restricted the carrier gas flow. Changes in carrier gas flow rates affect the residence time and trajectories of ions in the DM cell ultimately affecting transmission. Additionally, any change, even minor, in dopant concentration in the carrier gas affects the clustering of ions and ultimately changes the optimal V_c at which ions are transmitted through the cell. Because the V_c was constant during the imaging experiment, the change in chemical environment ultimately prevented transmission of PCs into the mass spectrometer for detection. This problem was observed as periods of no signal during the experiment and resulted in low-intensity streaks in the images. Later, a Swagelok cross union (fitted for 1/8" tubing") was used to allow a greater volume for solvent-gas mixing. Even still, over extended periods of time gas and dopant delivery was inconsistent to the point that it affected DMS operation.

Figure 3.9 shows images acquired during this optimization stage comparing DM separation of lipids with and without the isopropanol modifier. When isopropanol was used selective imaging of protonated and sodiated species was possible with V_c = 6.0 V (chosen based on data from Figure 3.7), whereas a V_c = 2.8 V allowed for exclusive imaging of sodiated PCs. These species and adducts were tentatively identified by comparing accurate masses with previously reported data.[140] Ignoring the streaks in the image, this separation is sufficient to clarify spatial distributions of [PC 34:1 + Na] versus [PC 36:4 + H], both m/z 782.

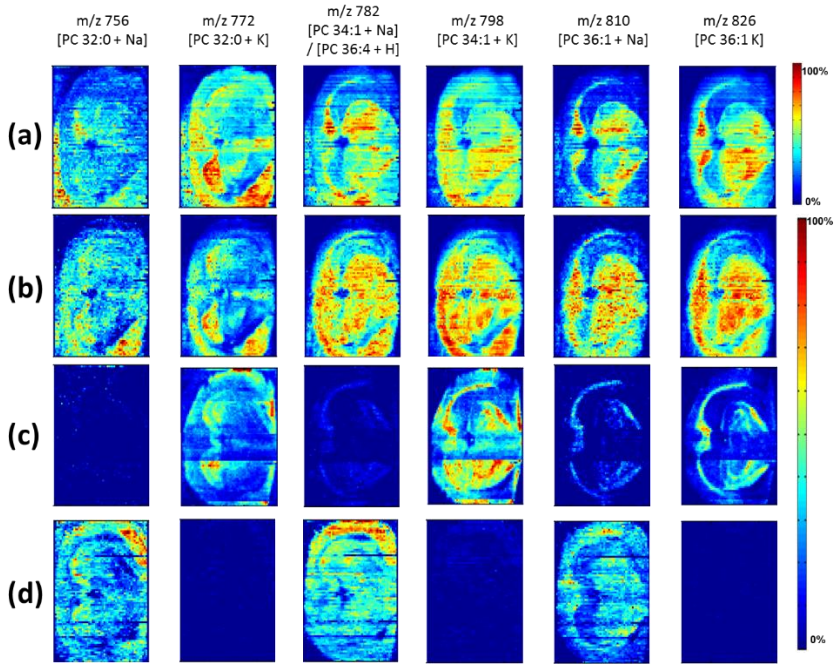

Figure 3.9. Control DESI-DM-MS images of PCs in brain tissues acquired in DM-off mode and no dopant in the carrier gas (a). DESI-DM-MS images acquired in DM-on mode with no dopant added and V_c = 5.3 V (b). DESI-DM-MS images acquired in DM-on mode and a carrier gas dopant of isopropanol introduced at a flow rate of 3 μL min^{-1} and V_c = 6.0 V (c) and V_c = 2.8 V (d). Ion image intensities in (b-d) were scaled to the maximum intensity observed across all three images. Intensities in (a) were left unadjusted due to a significant difference in ion intensity between DM-off and DM-on mode allowing for better visualization of spatial features.

As the system was being optimized for successful imaging with carrier gas modifiers, the electronics board controlling to the potentials applied to the DM plates failed beyond repair and prevented full implementation of carrier gas dopants for DESI-DM-MSI experiments. A recent publication by Lintonen et al. found isopropanol to be the best dopant for separation of phospholipids during a lipidomics study, which supports the findings here.[218] Therefore further investigation into the separation of lipids with carrier gas modifiers in DESI DM-MSI experiments is warranted for even greater selectivity and image enhancement. Additionally, this system was not tested in negative ion mode, and as

it could potentially assist in the separation of isobaric lipids from different classes in that mode, DESI-DM-MSI could be a valuable tool in selective imaging of those species as well.

3.5 Conclusions

Targeted differential mobility filtering prior to MS analysis has previously shown significant capabilities for improving signal-to-noise ratios while preserving duty cycle for a number of bioanalytical applications. This study demonstrated how these benefits translate to substantial improvements in ambient MSI image quality. In these experiments, DMS filtering facilitated significant signal to noise improvement, an order of magnitude increase, for imaging sea algae samples for a small (137 Da) chemical cue agent. Imaging of higher-mass lipid species in brain tissue sections further demonstrated the improved image quality and contrast with DMS filtering enabled. This was true when considering a single analyte but was further strengthened when considering multiple analytes of interest that may comprise a statistical component. The use of carrier gas dopants showed promise, but further characterization and implementation was halted by an electronics failure of the system. Overall, DMS, a high-duty-cycle ion mobility filtering method, offers convenient coupling to DESI-MSI and provides higher quality chemical images by filtering off unwanted signals and chemical noise.

CHAPTER 4. IMAGING BULKY SAMPLES BY DESORPTION ELECTROSPRAY IONIZATION MASS SPECTROMETRY

Adapted with permission from

Bennett, R. V.; Cleaves, H. J.; Davis, J. M.; Sokolov, D. A.; Orlando, T. M.; Bada, J. L.; Fernández, F. M., Desorption Electrospray Ionization Imaging Mass Spectrometry as a Tool for Investigating Model Prebiotic Reactions on Mineral Surfaces. Anal. Chem. 2013, 85 (3), 1276-1279. Copyright 2013 American Chemical Society.

Bennett, R.; Fernández, F., Desorption Electrospray Ionization Imaging of Small Organics on Mineral Surfaces. In Mass Spectrometry Imaging of Small Molecules, He, L., Ed. Springer New York: 2015; Vol. 1203, pp 79-89. Copyright 2015 Springer Science + Business Media New York.

4.1 Abstract

One key advantage of ambient ionization techniques for mass spectrometry imaging is their freedom from the confines of sample chambers commonly found in vacuum-based configurations. This offers a flexibility to accommodate both thin (~10 μm) and thick (> 10 mm) samples. As one example, this study showed that desorption electrospray ionization-mass spectrometry imaging (DESI-MSI) allows interrogation of the molecular species produced from chemical reactions on heterogeneous granite samples with minimal sample preparation. Mineral-assisted thermal decomposition of formamide ($HCONH_2$) is a heavily studied model prebiotic reaction that has offered valuable insights into the plausible pathways leading to the chemical building blocks of primordial informational polymers. To date, most efforts have focused on the analysis of formamide reaction products released in solution. Although several studies have examined the role of mineral catalysts in promoting this chemistry, the direct investigation of reactive mineral surfaces by DESI-MSI gives a new perspective on the important role of the mineral surface

in the formation of reaction products. Purine and pyrimidine nucleobases and their derivatives were successfully detected by DESI-MSI, with a strong correlation of the spatial product distribution with the mineral micro-environment. To our knowledge, this study was the first application of DESI-MSI to the study of complex and porous mineral surfaces, and their roles in chemical evolution. This DESI-MSI approach is generally applicable to a wide range of reactions or other processes involving minerals.

4.2 Introduction

Since the introduction of desorption electrospray ionization (DESI)[63] in 2004 and direct analysis in real time (DART)[64] in 2005, the field of ambient ionization mass spectrometry (ambient MS) has provided new and exciting analytical capabilities. Whereas vacuum matrix assisted laser desorption ionization (MALDI) and secondary ion mass spectrometry (SIMS) are commonly used for MSI, sample sizes are limited by the dimensions of the sample chamber, which is under vacuum. For both MALDI and SIMS, the sample must be mounted on a conductive substrate and be thin enough that it does not interfere with ion extraction; the electric field between the sample target and extraction lenses enable the transmission of charged species generated from the desorption-ionization process. In contrast, DESI, DART, and other ambient ionization techniques allow for *in situ* analysis in ambient air of thick or bulky samples. With the greater freedom afforded by ambient conditions, samples of many shapes and sizes may easily be positioned for effective surface sampling. As previously discussed, a successful DESI-MSI depends on consistent source-sample-inlet geometry, limiting samples to those with relatively flat surfaces (variations < 1 mm).[95, 107] However adjustments to accommodate unleveled and bulky samples are straightforward. Since its first demonstration,[80] DESI-MSI has been the

most popular ambient MSI technique, with applications to the analysis of biological tissues,[219,135,139] thin layer chromatography plates,[220] and algae surfaces[210] among other examples.

This study was the first application of DESI-MSI to the analysis of organic compounds on heterogeneous mineral surfaces which may have been involved in prebiotically-relevant reactions. Specifically, as a model system, the thermal decomposition of formamide and subsequent formation of a variety of compounds of biological interest[221,222,223] were examined. Formamide is the first hydrolysis product of hydrogen cyanide (HCN)[224] which may have been abundantly produced in the primitive atmosphere, depending on its composition.[225] Due to its stability compared to HCN,[226] and relatively low volatility compared to water, formamide may have been a plausible starting material for prebiotic nucleobase synthesis especially in drying lagoons or in geothermal fields, and in the pore spaces of carbonaceous chondrites during meteorite desiccation. Previous studies have shown that under a variety of environmental conditions possibly relevant to primitive Earth, formamide decomposition results in the synthesis of several nitrogen heterocycles of biological importance (Scheme 4.1).[223,227-228] These molecules may have been vital building blocks for RNA or related biopolymers on early Earth. While purine can be formed by heating or irradiating[229] neat formamide, inorganic catalysts, such as minerals (including metal oxides, clays, and iron-containing minerals), have been shown to also produce pyrimidines and to significantly alter the types and yields of both purines and pyrimidines from this reaction.[230,231] The interaction of formamide and the reaction products on minerals surfaces as well as the sequestration of products in the mineral pores could also facilitate the concentration of products allowing for possible polymerization.[232]

However the detection of formamide reaction products directly on mineral surfaces has not yet been reported, nor have any attempts been made to determine any particular specificity in the reaction probability.

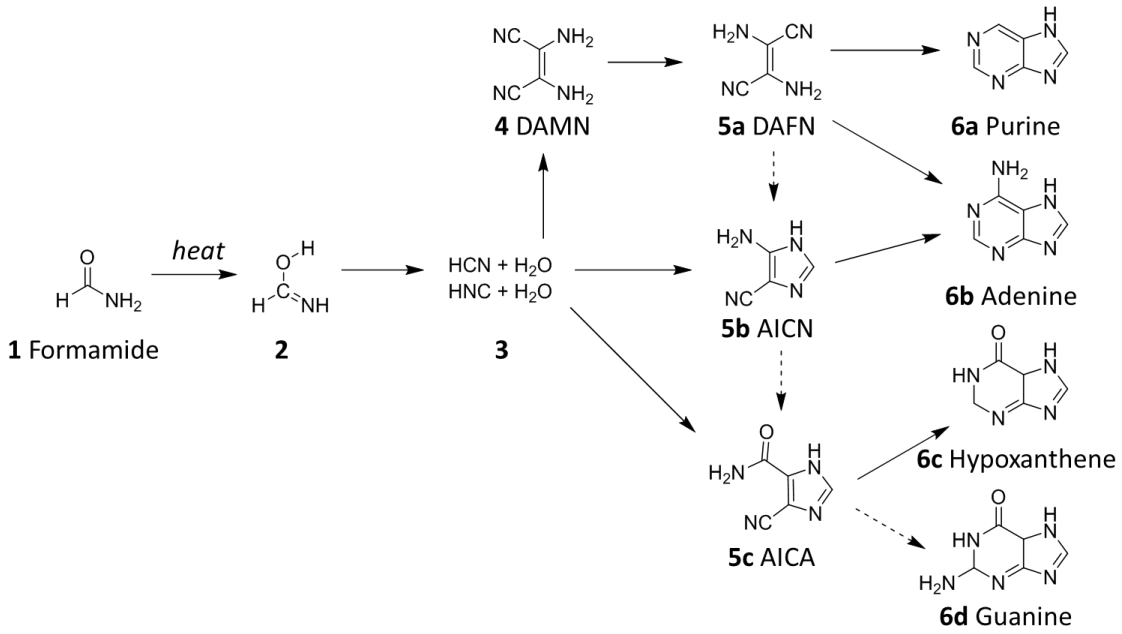

Scheme 4.1. Potential reaction pathway for the synthesis of nucleobases from formamide. (1) energy input as heat isomerizes formamide to formamidic acid, (2) which is then converted to hydrogen cyanide or isocyanide and water, (3) further transformations produce reactive intermediates diaminomaleonitrile (DAMN, 4), diaminofumaronitrile (DAFN, 5a), aminoimidazolecarbonitrile (AICN, 5b), and aminoimidazolecarboxamide (AICA, 5c), which go on the react further ultimately leading to the formation of purine (6a) and its derivatives including, but not limited to adenine (6b), hypoxanthine (6c), and guanine (6d). Adapted with permission from Reference 226.

Because they contain a variety of juxtaposed mineral species, granites were selected for this study to examine the effects of local mineral environments on the formamide reaction product mixture. Granites are mainly composed of heterogeneous assemblages of crystalline quartz, mica, and feldspar, and are believed to have formed on Earth in slowly cooling magmas as early as 3.5-4 billion years ago,[233] which may coincide with the period in which primitive life arose.[234] In practical terms, cutting of these granites into thin

sections presents a challenge, therefore the flexibility afforded by DESI-MSI with respect to sample sizes makes it ideal for chemical imaging of these surfaces.

4.3 Experimental Details

4.3.1. Granite Characterization

The large granite samples were cut with a mineral saw into smaller pieces with dimensions on the order of 20 x 20 mm, 3-6 mm thick. The surface of the cut samples were relatively flat and pore depths did not exceed 100 μm, as measured through optical profilometry (Wyco Non-contact Profilometer NT3300, Veeco, Plainview, NY, USA). Granite mineral composition was determined by bulk powder X-ray diffraction (XRD, RAXIS-RAPID, Rigaku, The Woodlands, TX, USA) and micro focused X-ray fluorescence (μXRF) imaging (Eagle III μXRF, EDAX, Mahwah, NJ, USA). X-ray images were collected by stepping the μXRF stage in 80 μm increments in an array pattern across each of the samples.[235] At each array point, a full X-ray spectrum was collected and stored in a hyperspectral binary data file. Once collected, a series of multivariate statistical algorithms were performed to reduce the dimensionality of the data and identify areas of spectral similarity.[236] These spectrally distinct areas were identified using K-means clustering, from which compositionally distinct granite/clay mineral phases were inferred. As these phases were identified, they were checked against the XRD to ensure accurate phase identification.

Raman microscopy was performed on the mineral samples for further characterization using a Senterra Raman microscope spectrometer (Bruker, Billerica, MA, USA). The incident laser wavelength was 532 nm, and data was collected in the pinhole

confocal microscopy mode. Raman spectral features in the 0-1500 cm^{-1} range were used to confirm the identity of the minerals present. XRD and Raman spectra were cross-referenced with the RRUFF Project Database.[237]

4.3.2. DESI-MSI Instrumentation

DESI experiments were performed with an Omni Spray® 2D automated DESI ion source (Prosolia, Indianapolis, IN, USA) coupled to a Synapt® G2 HDMS mass spectrometer (Waters, Milford, MA, USA) in positive ion mode. A nitrogen-assisted (140 psi) spray of methanol:water (7:3, 3 μL min^{-1}) was used. The methanol used was LC-MS Ultra Chromasolv® grade (Sigma Aldrich, St. Louis, MO, USA). Ultrapure water (18 MΩ cm^{-1}) was used in all experiments. Previous studies have shown that a 1:1 mixture of methanol and water is effective for the analysis of nucleobases by DESI-MS.[238] We increased the methanol content to a 7:3 ratio to decrease the diameter of the impact spot for improved lateral resolution.[109]

Granite samples were mounted on glass microscope slides using double-sided tape. Additional layers of tape were placed under select edges of the sample to level the top surface for consistent DESI source-surface-inlet geometry during imaging. Source geometry was optimized prior to each experiment for maximum sensitivity. The distance between the spray tip and the sample surface was 2 mm, and the angle was 58°, the separation between the source sprayer and the capillary inlet of the mass spectrometer was 4 mm. Sample stage motion controls were set such that data was acquired in 200 x 200 μm pixel sizes through a series of uni-directional line scans. The total area imaged was 10x10 mm, and the total image acquisition time was approximately one hour. The m/*z* range acquired for each pixel was 50-300. Mass spectral data was converted using Firefly™

conversion software (Prosolia Inc., Indianapolis, IN, USA) and images were visualized using BioMAP (maldi-msi.org). Image pseudocolor intensity scales within BioMAP were optimized for each image to maximize contrast.

4.3.3. Formamide Reaction

Before formamide reactions were performed, mineral samples were cleaned in order to remove intrinsic organic material from the surface. Heating in an oven (165 ˚C, 24 hours) followed by a "cleaning" DESI-MSI experiment over the entire surface effectively removed all contamination as evidenced by reduced Raman fluorescence and mass spectral data closely resembling that of the DESI spray solvent. Model reactions were carried out by submerging each granite sample in a glass beaker containing 50 mL formamide, which was then covered in aluminum foil. Mineral samples in formamide were heated in an oven at 160 ˚C for 96 hrs.

The average literature-reported amount of reactants used in the formamide-mineral reactions is ~5% mineral by weight with respect to the formamide.[228] Given the size of the granite samples used in the present studies, large amounts of formamide would be required to maintain the traditional reactant ratios. Therefore, the volume of formamide was reduced for practical reasons, but was still sufficient for satisfactory reaction yield. The substantial volume of formamide present during and after the reaction presents a challenge for DESI-MSI data interpretation due to adsorption effects. Initial formamide reaction conditions tested the feasibility of using smaller volumes of formamide to minimize this effect, however, this resulted in a very low abundance of the expected products on the surface such that imaging was not feasible. Therefore the 50 mL volume selected in conjunction with the adsorption control experiment was deemed appropriate.

At the end of this reaction period, samples were removed from the oven and supernatant solution, and blotted with a laboratory tissue (VWR, Radnor, PA, USA). Reacted granites were then rinsed twice in a methanol-water mixture (7:3) to remove outermost layers of the reacted formamide solution coating the surface. Though the presence of methanol and water in this rinse and DESI spray may affect some reaction pathways, it was necessary to remove excess formamide to allow for direct measurements of surface-adsorbed species. This rinse step may also impact the spatial distribution of the reaction products on the surface. However, we found the capability to image the products closest to the granite surface outweighed the adverse effects of the rinse step.

Products on the granite surface were putatively annotated based on accurate mass measurements and searching of a custom database. The reaction product database was compiled in-house using products reported in the literature.[228]

4.4 Results and Discussion

4.4.1. Granite Characterization

Bulk XRD (Figure 4.1a) identified the primary mineral component of the granite to be quartz (75%, SiO_2) based on peaks observed with 2-θ angles of 26.6° and 20.8°. Eleven percent of the total granite was orthoclase ($KAlSi_3O_8$, 2θ = 27.6°, 29.9°, 26.9°, 23.5°) and 5% consisted of biotite ($K(Mg, Fe^{2+})_3(Si_3Al)O_{10}(OH)_2$ 2θ = 8.8°, 26.5°). Elements identified based on μXRF spectral lines included Al (1.45 keV), Ca (3.65 keV and 3.93 keV), K (3.26 keV), Fe (6.36 keV and 6.96 keV), and Si (1.72 keV). These elements were identified using the higher energy K-L_3 (Kα) and K-M_3 (Kβ) transitions, for which the peak centroids are listed. Once fully identified, the X-ray images were color coded to show class

membership, as shown in Figure 4.1b. The three major phases identified on the surface using this method were quartz, orthoclase and biotite and the corresponding optical image of the granite sample is shown in Figure 4.1c.

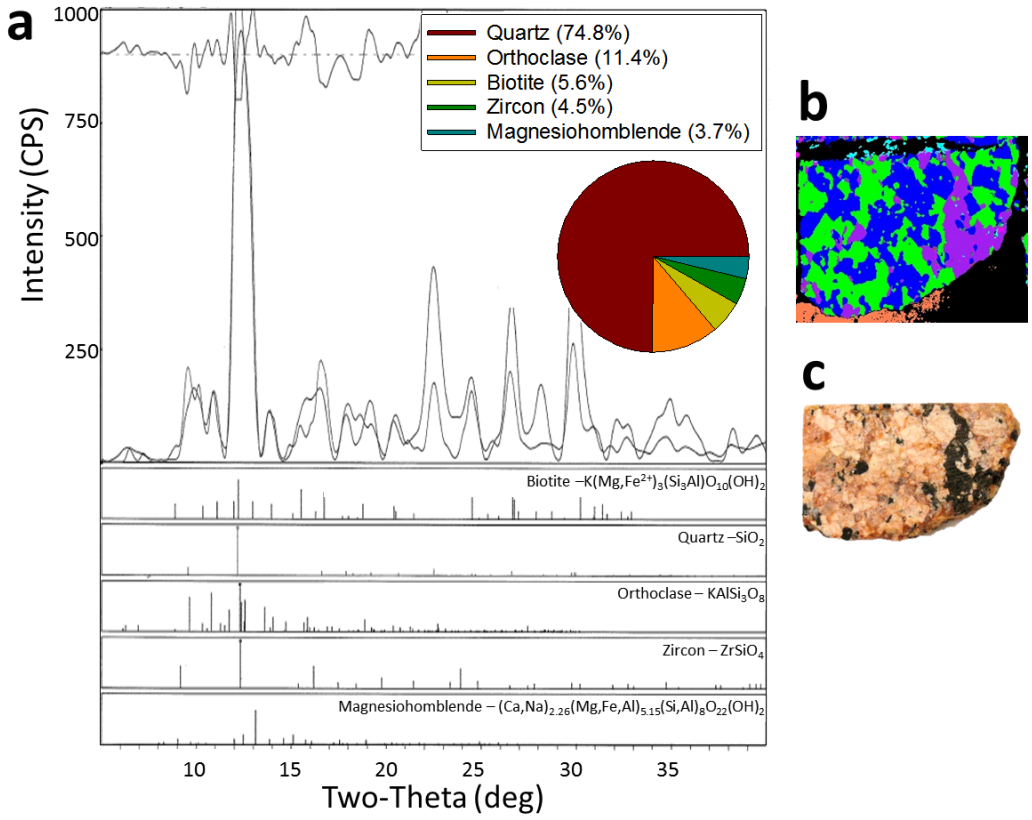

Figure 4.1. XRD spectra from the bulk granite sample compared to spectra from pure mineral standards to determine corresponding percent compositions (a). µXRF image of the granite surface with data clustered to show key mineral types – quartz (green), orthoclase (blue) and biotite (purple), (b), and the corresponding optical image of the same granite sample (c).

As another means by which to confirm the mineral composition of the granite sample, Raman spectra were acquired directly from the granite surface (Figure 4.2). The spectra presented are baseline corrected with intensities normalized to the maximum signal observed for each spectrum. Surface regions of interest sampled were selected for

maximum separation of mineral types, however the heterogeneous mineral surface composition inevitably complicated spectra and their interpretation. Key Raman shifts for biotite were observed at 189.5, 377.0, and 582.0 cm^{-1}; orthoclase Raman shifts were observed as broad peaks at 375.0 and 583.0 cm^{-1}; quartz Raman shifts were observed at 124.5, 203.0, 351.5, and 461.5 cm^{-1}. These spectral features compare well with literature values for the corresponding minerals,[237] and combined with XRD and μXRF data confirm mineral types and their spatial distributions in the granite.

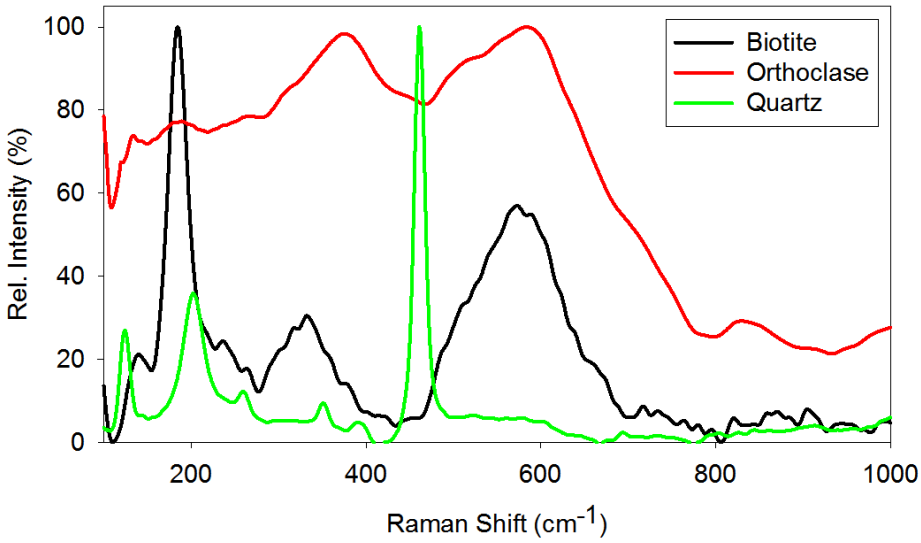

Figure 4.2. Surface Raman spectra obtained from areas of unique mineral composition.

4.4.2. DESI-MSI of Reaction Products

Prior to conducting the formamide-mineral reactions, the granite samples were imaged by DESI-MSI for two reasons: (1) to clean the sample surface and (2) to ensure that none of the desired reaction products were already present on the surface. The volume of the DESI solvent system believed to remain on the granite surface following this

experiment is thought to be minimal when compared to the volume of formamide used in the decomposition reaction. Therefore, it should have minimal effect on the reaction outcome. Figure 4.3 shows the optical image (a) of the granite surface imaged and the key ion images acquired during this imaging step (Figure 4.3b-d). Purine (Figure 4.3c) and other expected reaction products showed negligible abundance on the granite surface indicating any product detected following the decomposition of formamide was generated from the reaction itself.

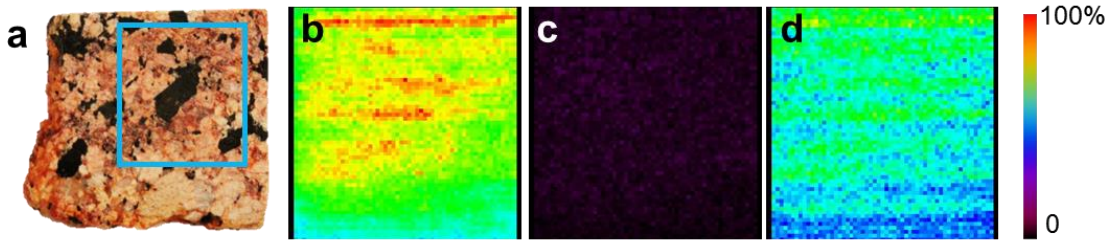

Figure 4.3. Optical image of the unreacted granite sample with the area imaged outlined in blue (a), total ion image (b) and selected ion images of protonated purine (m/*z* 121, c) and solvent contaminant phthalate ester (m/*z* 149, d) obtained by imaging the unreacted granite sample by DESI-MSI. The intensity scale range for (c) and (d) were set to match the maximum intensities observed following the formamide reactions in order to demonstrate relative ion abundance difference before and after the formamide reaction.

The average mass spectrum obtained from averaging one line scan across the clean granite surface in imaging mode is shown in Figure 4.4a. The species detected are primarily attributed to contaminant species present in the DESI solvent; a similar spectrum was obtained by spraying the solvent directly on a clean glass slide for comparison purposes that showed similar peaks. Figure 4.4b shows the average spectrum obtained from a single line scan of the reacted granite surface. Peaks unique to this spectrum are considered

products from the formamide reaction with the granite. Two key signals detected on the reacted granite include peaks with m/*z* values of 121.0471 and 135.0230, which were tentatively identified based on accurate mass as protonated purine and sodiated 5-azacytosine. Chemical imaging by DESI-MSI of a larger area of the granite surface was used to obtain more representative results of the reaction products along with their spatial distributions.

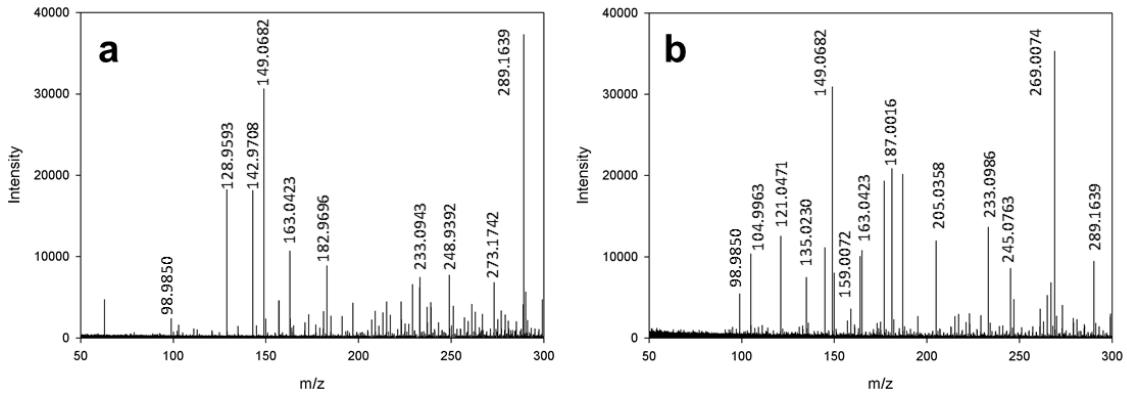

Figure 4.4. Mass spectra averaged across a single line scan of the surface of the unreacted (a) and reacted (b) granite surface obtained by DESI-MSI.

Figure 4.5 shows an optical image, the total ion, and selected ion DESI-MS images for a representative granite sample reacted with formamide. Image features were found to correlate with mineral surface composition for all products as highlighted by the comparison between the optical image of the granite sample (Figure 4.5a) and the total ion image (Figure 4.5b). When selected ion images for detected products were compared individually to the optical image, identical correlations were observed for all products except for purine (Figure 4.5c). As purine was the dominant reaction product, it may have

coated the entire granite surface in a layer too thick to discern a correlation with the local surface environment.

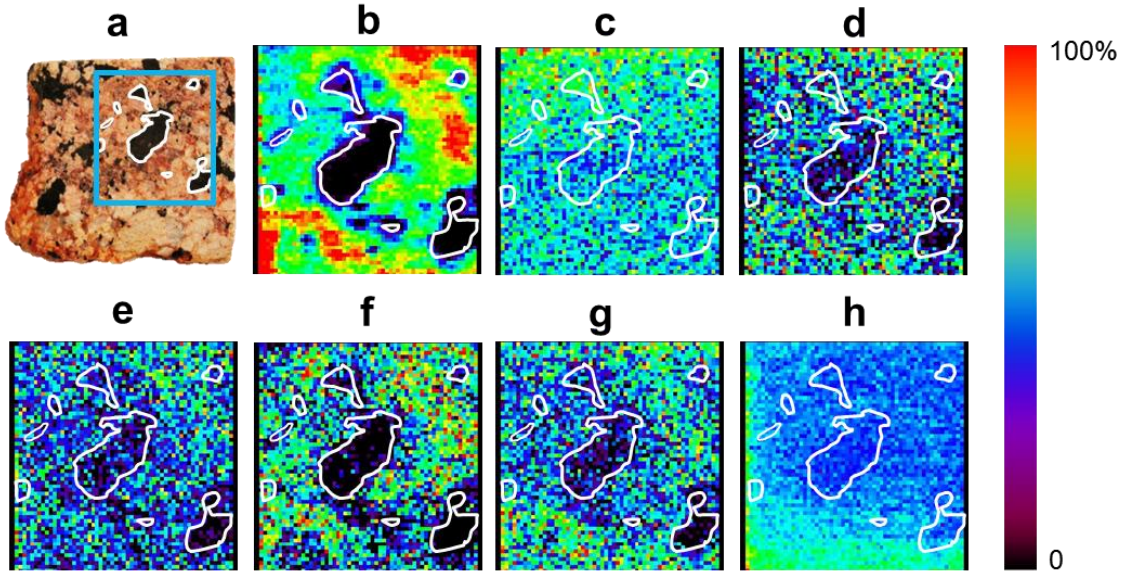

Figure 4.5. Optical image of reacted granite (a), total ion image (b) and selected ion images of protonated purine (m/*z* 121, c), sodiated 5-azacytosine (m/*z* 135, d), potassiated purine (m/*z* 159, e), potassiated n(9)-formylpurine (m/*z* 187, f), sodiated cytosine dimer (m/*z* 245, g), and phthalate ester (m/*z* 149, h) acquired with the area imaged outlined in blue and trends overlaid in white.

The reaction products detected were tentatively identified and are listed in Table 4.1. The relatively high abundance of alkali metal adducts observed is attributed to the presence of the corresponding cations in the granite minerals. To compare average product abundance and distribution across different mineral types, spectra were averaged across representative equal-areas of each individual mineral type in the granite and divided by the total selected ion intensity sum for each mineral type. While all products were detected across the entire granite, 39% of the total product population was present on quartz, followed by orthoclase (34%). The lowest relative product abundance was observed on the

biotite regions (27%), being roughly one third less than for quartz. These results indicate that DESI facilitates the analysis of a complex mixture of organic matter present on surfaces with heterogeneous composition and morphology.

Table 4.1. Tentatively identified products and their distributions across minerals present in the granite sample shown in Figure 1.

Assignment	Exp. m/*z*	Mass Error (mDa)	% Abundance		
			Quartz	Biotite	Orthoclase
$[Purine + H]^+$	121.0471	4.3	37.3	30.2	32.5
$[5\text{-azacytosine} + Na]^+$	135.0230	5.3	40.2	29.0	30.8
$[Purine + K]^+$	159.0072	0.1	39.4	24.5	36.1
$[N(9)\text{-formylpurine} + K]^+$	187.0016	6.0	37.1	27.4	35.5
$[2Cytosine + Na]^+$	245.0871	10.8	38.7	26.1	35.2

4.4.3. Transmission Control

To ensure that the observed DESI-MSI surface features were not experimental artifacts, several control experiments were conducted. First, a transmission control experiment was performed to verify that analytes were desorbed and ionized consistently across different mineral types present in the granite sample. Differences in the physical properties of each of these minerals has the potential to affect the extent to which an analyte is extracted, desorbed and ionized during the DESI process.

During the imaging of the granite samples, depending on solvent grade, impurities in the solvent may still be observed.[174] These impurities can be identified through a reflective ESI[106, 220] background spectrum acquired by spraying at a clean glass slide

(versus the granite surface). A common solvent contaminant found in methanol, $C_8H_4O_3$ m/*z* 149, an ion originating from phthalate esters[174] was detected in all DESI-MSI experiments. It is assumed that this species is mixed evenly throughout the solvent syringe and is being delivered at a constant concentration in the DESI spray. Therefore, any changes in the intensity of this ion would indicate changes in ion transmission due to differences in the porosity or roughness of the different minerals on the surface, resulting in changes in surface liquid film formation and DESI secondary droplet emission angles. The homogeneous distribution of m/*z* 149 shown in Figure 4.5h, however, indicated that there was no appreciable change in ion transmission between different mineral types.

4.4.4. Selective Adsorption Control

The presence of a large volume of reaction supernatant in extended contact with the mineral could result in the selective adsorption of products in solution onto the surface. In order to verify that the observed product distributions are not simply due to selective adsorption, a granite sample with a comparable composition of the one shown in Figure 4.1 was soaked in adenine (25 μM in methanol) for 48 hours and then DESI-imaged. Adenine was chosen because of its chemical similarity to the reactions products and would behave comparably in the presence of the granite. Because the reflective-DESI control showed homogeneous desorption/transmission across mineral types, any difference in adenine intensity would be the result of adsorption differences. No variation of ion intensity across the mineral surface was observed, indicating no preferential adenine adsorption (Figure 4.6).

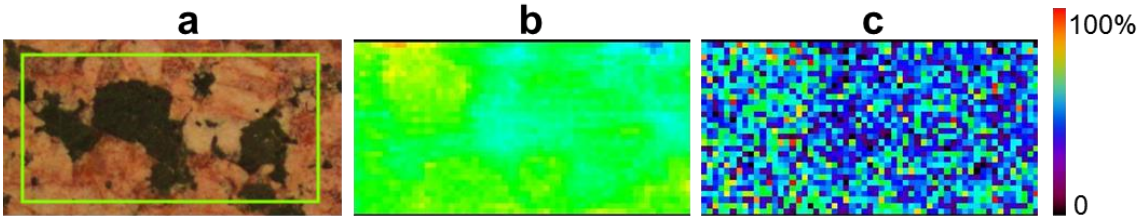

Figure 4.6. Optical image (a) of granite sample that was soaked in adenine with area imaged by DESI-MSI outlined in green, total ion intensity image (b) and extracted ion image of protonated adenine, m/z 136 (c).

4.4.5. Thermal Decomposition Control

In order to confirm that the products observed on the surface of the mineral sample were produced by the heating of formamide with the granite, we performed a control experiment in which a mineral was soaked in formamide, but not heated. Prior to the control experiment, the mineral underwent the same cleaning process by heating and blank imaging. The granite sample was then submerged in 50 mL of formamide and covered for 96 hrs in an identical manner as for the heated reaction, but was left at room temperature (25 °C) as opposed to 160 °C. The control granite was then imaged according to the same procedure as the heated reaction by DESI-MSI. All products observed in the heated reaction (Table 4.1, Figure 4.5) were mapped and showed low-intensity homogenous distributions indicating that the products observed on the surface are not endogenous and are only formed when the formamide is heated in the presence of the granite sample. Representative results from the control experiment are given in Figure 4.7, and the ion intensities for Figure 4.7a-c were scaled to match the respective maximum intensities detected from the heated formamide reactions for each analyte.

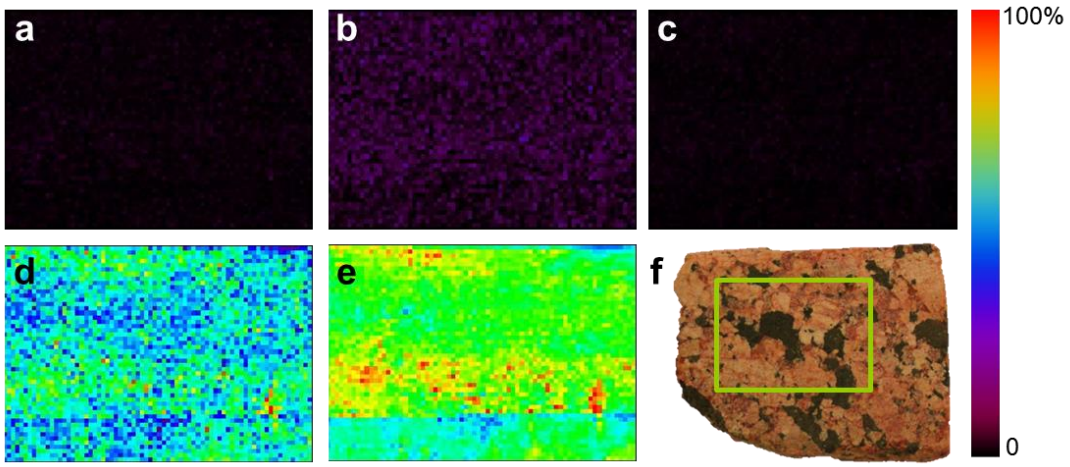

Figure 4.7. Extracted ion images of protonated purine, m/z 121 (a), protonated adenine, m/z 136 (b), potassiated N(9)-formylpurine, m/z 187 (c), solvent contaminant phthalate ester, m/z 149 (d), and total ion (e) images obtained by DESI-MSI of a granite sample (f, imaged area outlined in green) soaked in formamide at room temperature.

4.4.6. Ultra-High Performance Liquid Chromatography-Tandem Mass Spectrometry (UPLC-MS/MS) Analysis of the Reaction Supernatant

Following the reaction of formamide in the presence of the granite sample, the supernatant solution changed color from clear to a dark brown (Figure 4.7). This indicates a change in the composition of the solution, which likely contains a number of reaction products. Previous literature reports of the thermal decomposition of formamide in the presence of inorganic catalysts have studied products present in the supernatant, therefore it is logical to expect reaction products in that phase.[229] To characterize the supernatant and validate the imaging results, analysis of the reaction supernatant solutions was performed using UPLC-MS/MS. Due to the high concentration of formamide in the supernatant, a serial dilution was used to prevent contamination of the mass spectrometer. Purine and adenine were readily detected, and MS/MS was performed to successfully confirm

identities. Uracil and N(9)-formylpurine were also detected, but in low abundance that prevented MS/MS analysis. The low number of products detected is attributed to the serial dilution, which could have diluted low-abundance species below limits of detection. Alternatively, vacuum centrifugation at elevated temperatures[229] is recommend for future experiments to remove formamide without sacrificing sensitivity for low-abundance products. Even so, these results confirmed that the thermal decomposition of formamide in the presence of the granite samples is reacting as expected.

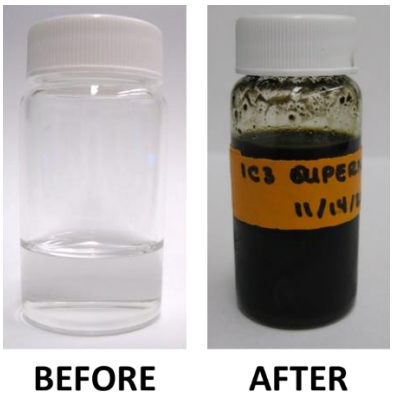

Figure 4.7. Optical images of the formamide before and after the thermal decomposition reaction in the presence of a granite sample.

4.4 Conclusion

In conclusion, this study demonstrates the ability to successfully image porous and bulky samples by DESI-MSI. DESI-MSI enabled the detection of products of the model prebiotic formamide reaction, indicating their distribution across a heterogeneous mineral surface. Control experiments confirmed that product distributions are not an artifact from the DESI analytical process or the selective adsorption of products onto the surface,

confirming previous hypotheses that indicated that mineral surfaces play a direct reactive or catalytic role in the formamide reaction. To our knowledge, this study was the first application of DESI to the analysis of minerals.

CHAPTER 5. NOVEL THREE-DIMENSIONAL SURFACE IMAGING USING ROBOTIC PLASMA PROBE IONIZATION MASS SPECTROMETRY

Adapted with permission from

Bennett, R. V.;* Morzan, E. M.;* Huckaby, J. O.; Monge, M. E.; Christensen, H. I.; Fernandez, F. M., Robotic plasma probe ionization mass spectrometry (RoPPI-MS) of non-planar surfaces. Analyst 2014, 139 (11), 2658-2662.

* Equally contributing authors

5.1 Abstract

In order to image irregularly-shaped samples by mass spectrometry, typically they must first be sliced into a series of 2D sections to accommodate ion source geometry restrictions. During this process, there is potential for disturbing the natural spatial distributions of molecules of interest. Instead of altering the sample to fit the method, a new technique for imaging irregular, 3D surfaces was developed using a robotic sample introduction/ionization system for mass spectrometry termed Robotic Plasma Probe Ionization Mass Spectrometry (RoPPI-MS). In RoPPI, a Universal Robots UR5 robotic arm with six degrees of freedom maneuvers an acupuncture needle to probe the sample surface, then places the probe into the ionization region of a plasma ion source for subsequent MS detection. The motion of the robot is guided by a PrimeSense Carmine short-range sensor communicating to an RViz software package that generates a point cloud within for x,y,z coordinate selection on the sample surface. By probing multiple points across a sample, a chemical image of the surface may then be rendered. Direct analysis in real time (DART) was selected as a plasma-based ionization source for RoPPI given its ability to ionize both polar and non-polar analytes and its relatively large

ionization region. The modularity of the RoPPI system makes it conducive to the imaging of various samples such as irregular mineral surfaces, biopsies, whole organs, or skin lesions, through any number of interchangeable sampling/ionization probes.

5.2 Introduction

Vacuum-based ionization techniques such as matrix-assisted laser desorption/ionization (MALDI)[23] or secondary ion mass spectrometry (SIMS)[5] provide high spatial resolution images (~10 μm or 100 nm, respectively), but require thin planar samples. Ambient MSI methods are less restricted by sample size and shape, offering convenience through reduced sample preparation, but still generally require flat samples. These include spray-based techniques that comprise a solid-liquid extraction followed by electrospray ionization as in the case of desorption electrospray ionization (DESI)[80, 89] and the liquid microjunction surface sampling probe (LMJ-SSP).[117] Laser ablation can be coupled to various ionization sources for imaging, as in laser ablation-electrospray ionization (LAESI)[239] or infrared laser ablation-metastable-induced chemical ionization (IR-LAMICI),[75] among others.[240] Alternatively, sampling of a surface decoupled from the ionization event can be achieved using a small probe, such as the solid needle used in probe electrospray ionization (PESI)[241-242] which laid the foundation for our work.

MSI data is typically acquired for 2-dimensional planar samples, given the need for consistent probe-surface-inlet geometry. MSI analysis of more irregularly-shaped objects can be performed in one of the following ways: (1) 2D imaging of serial sample sections followed by computer rendering into a 3D image or (2) serial imaging of surface layers by sequential depth profiling or sputtering across an area.[243] The first method is commonly used in the 3D imaging of biological tissues and is amenable to all imaging methods.[244]

The second is typically performed with a more ablative method, such as LAESI or SIMS, on thicker samples.[245-246] Both approaches ultimately produce a full 3D volumetric image with information about the sample interior, but require long (≥ 40 hours) analysis times, and several sample preparation steps.[81]

This study was driven by the need to image irregular sample ***surfaces*** without destroying the sample during sectioning or ablation. A method for the systematic 3D surface analysis of native, irregularly-shaped or curved samples was developed by coupling robotic probe surface sampling with direct analysis in real time (DART).[64] DART was selected as a plasma-based ionization source for its ability to ionize both polar and non-polar analytes[247] and its relatively large ionization region.[248] In DART (Figure 5.1), a point-to-plane glow discharge plasma is used to generate atomic metastables from the helium (or occasionally nitrogen) gas traveling through the ion source. The gas is then heated and flows through a grid electrode, which filters out charged species formed in the discharge to prevent ion-ion and ion-electron recombination. Therefore only neutral metastables and gas molecules exit the ion source. These reactive species are directed towards the mass spectrometer, and when the sample is placed in this gas stream, analytes are thermally desorbed and ionized for detection.

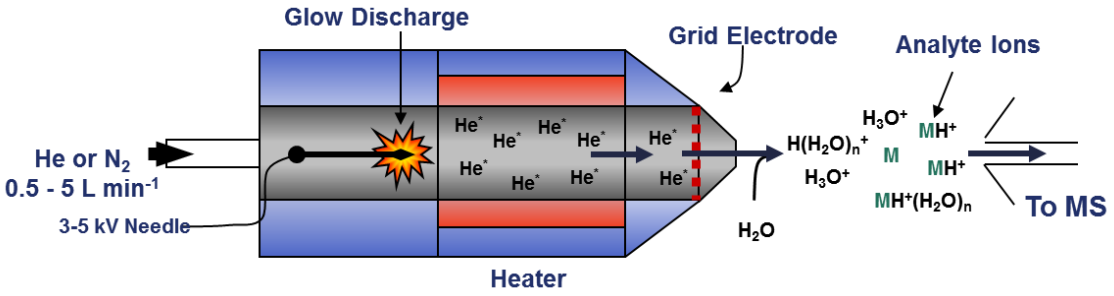

Figure 5.1. Schematic of DART ion source and ionization process. Metastables are generated from the glow discharge and the gas is heated by a ceramic heater. Metastables and neutrals exit the source through a grid electrode and then react with atmospheric water and analyte molecules to form analyte ions for mass spectral detection.

The detection of protonated ions ($[M + H]^+$) in the mass spectra suggests that the DART ionization process begins with the formation of atmospheric water ion clusters from the helium metastables (He^* 2^3S_1, 19.8 eV) via Penning ionization.[64] These water ion clusters then protonate desorbed analyte molecules through proton-transfer reactions, thus generating analyte ions. This mechanism is possible because atmospheric water has a lower ionization energy that the internal energy of He^*. Furthermore, protonation of analyte molecules from the water clusters is only possible if the analyte has a higher proton affinity than the water ion clusters.[249-250] Alternatively, analytes may be ionized via direct Penning ionization[251] by He^* or by charge-exchange reactions with molecular oxygen ions ($[O_2^{+\bullet}]$) formed by Penning ionization by He^*, but these pathways are less common and depend on analyte ionization efficiency and gas-phase basicity.[247]

The spatial positioning and orientation of the sample in the ionizing gas stream can influence sensitivity in DART ionization due to the thermal gradient of the reactive gas plume that will affect analyte desorption.[248] Furthermore, positioning of the sample will also affect fluid dynamics of transferring analyte ions into the mass spectrometer.[252]

However the source-sample-inlet geometry for DART has higher tolerances on the order of several millimeters compared to the more restricted alignment in DESI, for example. The larger ionization region accommodates minor precision errors in the robotic placement of the sample probe while still allowing for efficient ionization. Another advantage of coupling the robotic probe with DART is that the sample does not need to contain a minimum amount of water or other fluids for effective ionization as in the case of PESI[241] due to the inherent ionization mechanisms of plasma-based sources.[64, 67]

The large range of ionizable analytes and the implementation of a robotic probe broaden the possible applications of this new surface analysis technique, and allow for remote sampling. For example, this system would be conducive to the real-time analysis of metabolites in biological samples, as in the case of tissue screening during surgery to differentiate between healthy and tumor regions for biopsy, given the rather non-invasive nature of the acupuncture needle. Because the surface sampling step is removed from the ionization process, this offers flexibility to modify the surface probe or ionization mechanism used to maximize practicality for unique applications.

5.3 Experimental Details

5.3.1 DART-MS Instrumentation

A DART source (Ion Sense, model SVP100) coupled to a Q-TOF mass spectrometer (Bruker micrOTOF-QII) was used for all the measurements in positive ion mode using He as the discharge supporting gas (1 L min-1). The set DART gas temperature was varied between 200 and 400 °C to determine the effects of the temperature on the shape of the ion trace. The glow discharge needle voltage of the DART source was set to -

3500 V. Millenia stainless steel acupuncture needles (0.18 mm x 13 mm) were used for surface sampling by mounting them on a custom-made PEEK block which was tightly held by the robot gripper.

5.3.2 Lynxmotion Robotic Arm

The first robotic arm used in the set-up was a Lynxmotion AL5A (Swanton, VT, USA) with 5 degrees of freedom. The median reach of the arm was 14.60 cm with a 113.40 g lift capacity. Only the wrist and the base actuators were used in order to maximize precision. The robot was manually moved to define home, sampling and analysis positions which were then saved into a motion path program (Lynxmotion RIOS SSC-32 V1.06). This sequence was repeated for each sampling position on the hemisphere with constant home, sampling and analysis positions, and the sample was manually moved using the 3-axis RollerBlock (ThorLabs, Newton NJ).

5.3.3 Kuka Robotic Arm

The second manipulator used was a KUKA KR5 sixx R650 robot (Shelby Township, MI, USA), a platform targeted toward light manufacturing and industrial tasks. It has 6 degrees of freedom with a maximum reach of 650 mm, a payload of 5 kg, and a maximum speed of 7.6 m s^{-1}. Motion control of the robot was programmed using a custom Robot Operating System (ROS) interface to the KUKA controller. Robot perception was performed using a PrimeSense (San Jose, CA, USA) Carmine 1.09 short range 3D sensor mounted to the end effector of the robot, just above the sampling rig, calibrated to the reference frame of the robot, and the Point Cloud Library (PCL) software package. Using techniques from computer vision, the library takes data from the sensor and creates a 3D

point cloud of the environment. The RViz visualization software (also available from ROS) was utilized to visualize that point cloud of the scene, and provide an interface for the human operator to specify a location on the surface for the robot to sample. After peak area was extracted from extracted ion chronograms, all images were rendered in Matlab® (Mathworks, Natick, MA, USA).

5.4 Results and Discussion

5.4.1 Principles of Operation and Motion Sequence

Two different robotic arms were utilized for proof-of-principles experiments: a do-it-yourself Lynxmotion AL5A-5 and a Kuka KR5 sixx R650 robot. Figure 5.2 schematically illustrates the analysis process of this method with the Kuka robot when sampling dye-colored spots on a hand-painted polystyrene hemisphere as a test sample. Starting at a "home position" (Figure 5.2a), a robotic arm maneuvers an acupuncture needle to stab the surface of the sample, which is mounted remotely outside the ionization region, thus collecting a small amount of analyte (Figure 5.2b). This is similar to the initial step in the PESI process, but robot-assisted. The needle is then reproducibly inserted into the ionizing gas stream of the DART ion source (Figure 5.2c). The position sampled by the robotic probe may be selected by means of a joystick control, or by using a 3D camera (Figure 5.2f) that creates an (x,y,z) point cloud (Figure 5.2g) for accurate sample coordinate determination. A selected ion chronogram observed for each of the analysis steps described, and the subsequent mass spectrum are shown in Figure 5.2d-e. By probing multiple points across the sample surface, the acquired mass spectra (and corresponding peak areas from extracted ion chronograms) are correlated with the known x, y, and z

position. We have named this approach Robotic Plasma Probe Ionization-Mass Spectrometry (RoPPI-MS).

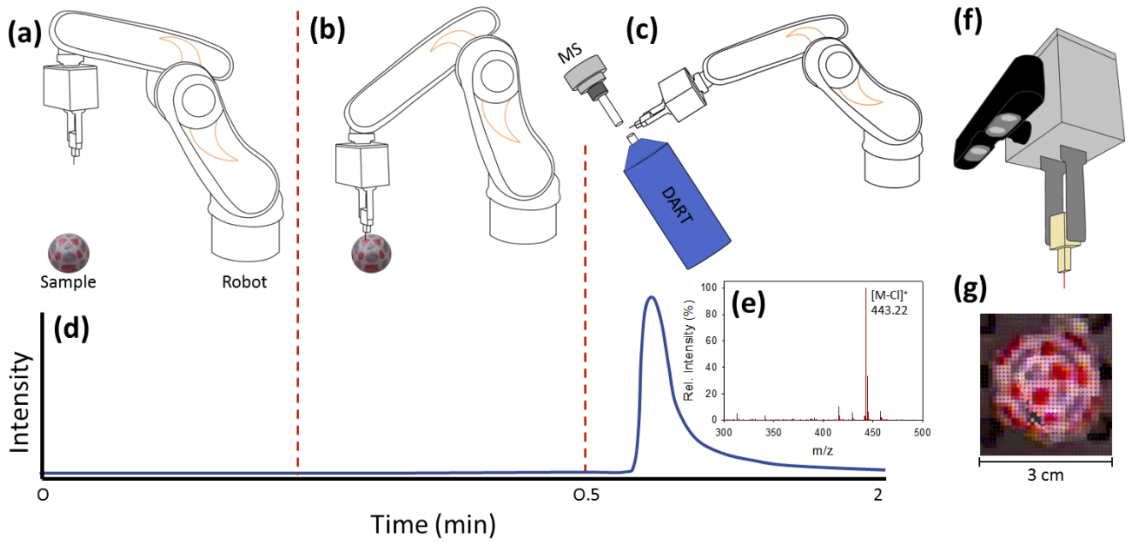

Figure 5.2. Robot in the Home position (a), Sampling position (b), and Analysis position in which the needle is placed between the DART ion source and MS gas-ion-separator (GIST) interface (c). Selected ion intensity chronogram at m/z 443 ([M-Cl]+ for Rhodamine 6G) observed during the analysis sequence corresponding to the robot positions described directly above (d). Sample mass spectrum observed during analysis of Rhodamine 6G coloured spots (e). End effector (grey), PEEK needle mount (tan), acupuncture needle (red) and 3D visualization camera (black) (f) for point cloud generation (g).

5.4.2 Minimizing Analysis Time

The total analysis time in RoPPI-MS is dependent upon three factors: robot speed, number of surface points, and desorption/ionization time of the analytes from the needle. In the current configuration, the latter of these is the slowest step (on the order of minutes), and thus the speed-limiting variable as it depends on the time for the signal to return to the baseline ensuring no carryover between samples. The duration of this step can be optimized

by changing the temperature of the DART gas stream to induce faster exhaustive sample consumption. In order to optimize the DART temperature for ideal operation, a planar polystyrene surface was colored with black Sharpie. The surface was robotically probed and the base peak signal (m/z 303.4819) was recorded for different positions in the ionization region, and various DART temperatures between 200 and 400 °C (Figure 5.3); the sample was left in the ionization region until the signal returned to baseline. Maximum sensitivity was observed when the acupuncture needle tip was placed within 1 mm of the DART nozzle, the hottest region of the gas stream.[248] Indeed, the highest signal intensity was observed at 400 °C with negligible thermally-induced analyte fragmentation. Peak resolution, calculated as the full width of the peak, at half-maximum (FWHM) was comparable for 300-400 °C, FWHM ≈ 0.15 minutes, but increased for 250 °C (0.21 min) and was highest for 200 °C (0.46 min). Some variability in signal intensities observed at different temperatures might be attributed to the sampling of unique positions across the sample that might have different analyte abundances. However this variability is not expected to be an order of magnitude change, therefore the differences in sensitivity are predominantly based on DART temperature. A DART operating temperature of 400 °C was chosen for further experiments given highest sensitivity and narrow desorption profiles that enabled higher throughput analysis.

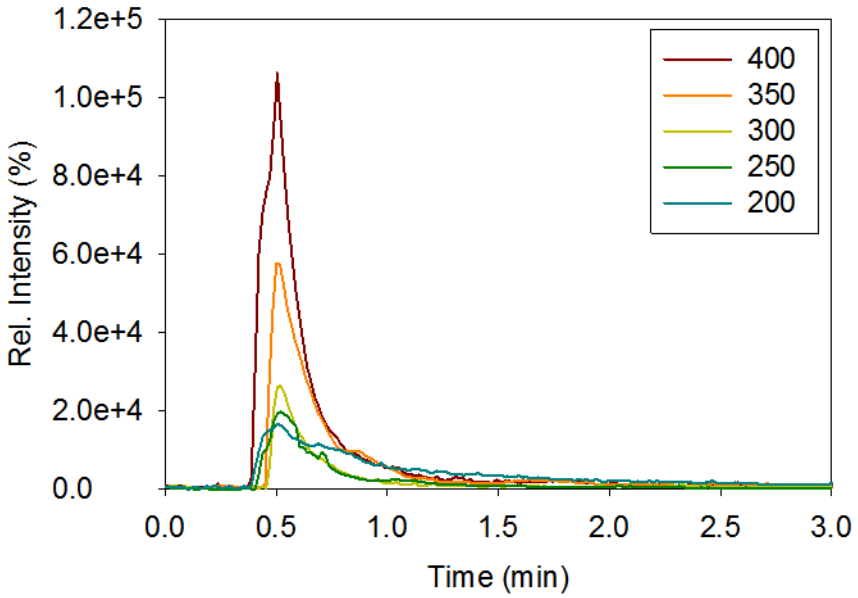

Figure 5.3. Absolute ion intensity for m/z 303, a dye found in black Sharpie© as a function of time for different DART heater temperatures (°C). As DART temperature increases, signal intensity also increases.

The need for higher desorption temperatures than those typically utilized in DART-MS with glass sampling probes, is attributed to the thermal conductivity of stainless steel, which is 15× higher than glass.[253] Glass melting point capillaries are common sampling tools for DART because they efficiently maintain heat at the tip of the capillary where the sample is localized for desorption. In contrast, the higher thermal conductivity of the stainless steel results in faster heat dissipation across the needle and thus less effective vaporization of the analytes on the tip. The small mass of an acupuncture needle further favors heat dissipation in comparison to the larger glass capillary. The higher DART analysis temperature is not only necessary for faster analysis times, but also beneficial to prevent carryover between sampling points. In the current system configuration, the motion sequence is manually initiated for each sampled point when the total ion trace returns to

baseline intensity, indicating all analyte has been desorbed and no sample is being carried over to subsequent analyses.

5.4.3 Proof-of-Principle Testing

The do-it-yourself Lynxmotion AL5A-5 robotic arm was used in the first set of experiments (Figure 5.4), and comprised 5 degrees of freedom and motion precision of ~5 mm. To enhance accurate surface analysis, only two arm degrees of freedom were used, which improved precision to 3 mm. With this system, the sample was mounted on a 3-axis RollerBlock with micrometer drives with 0.01 mm precision to control sampling position. The robot was programmed to sample one specific x, y, z coordinate orthogonal to the sample stage, and the RollerBlock moved the sample so that new regions of the sample surface were probed. Manual control of the sample stage allowed for simplified robot programming by repeating one motion sequence. For this set of experiments, the polystyrene hemisphere (13 mm diameter, shown in Figure 5.5a) used as test sample was painted with Rhodamine 6G (m/*z* 443.2335,) and Nile Blue Chloride (m/*z* 318.3645) in three rows of eight equally-spaced spots.

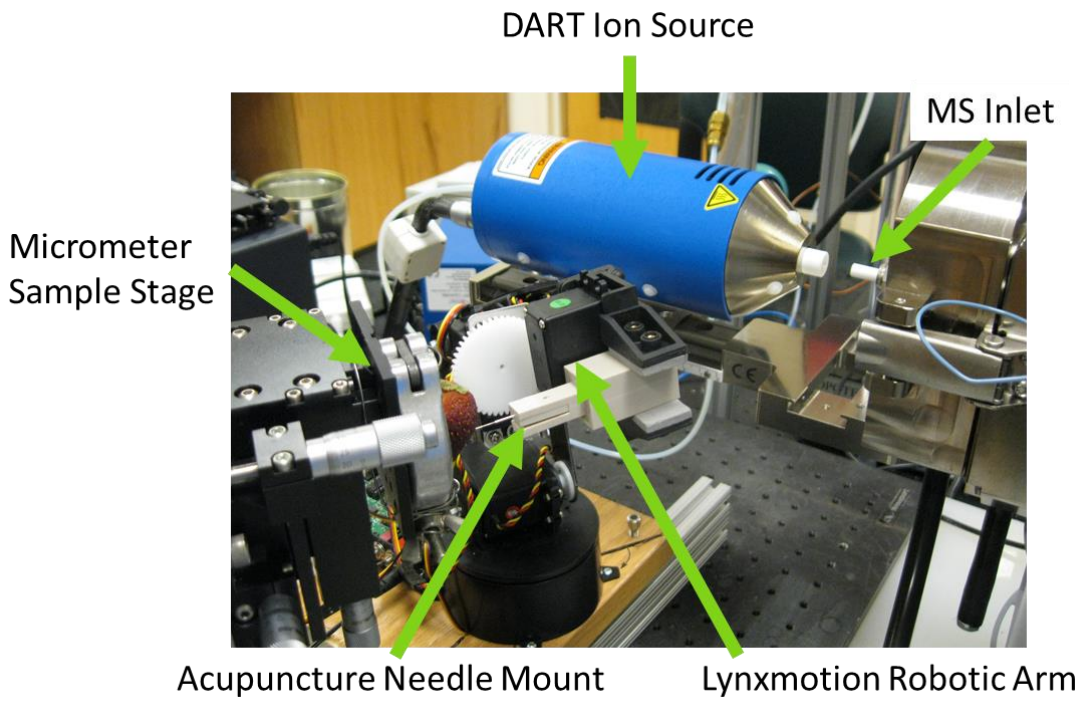

Figure 5.4. Picture of the RoPPI system with the Lynxmotion robotic arm. In this snapshot, the robot is maneuvering the acupuncture needle to probe the surface of a strawberry mounted on the micrometer sample stage.

The theoretical limit of the spatial resolution of this technique is determined by the diameter of the sampling probe, which in this case is an acupuncture needle of 180 μm. However, the Lynxmotion robotic arm limits the spatial resolution to ~3 mm. For this reason, preliminary experiments were carried out by sampling only one point for each color painted block on the polystyrene hemisphere (Figure 5.5a). By puncturing the surface to a depth of ~2 mm, this simple proof-of-principle setup afforded sufficient sensitivity, but with significant resolution limitations.

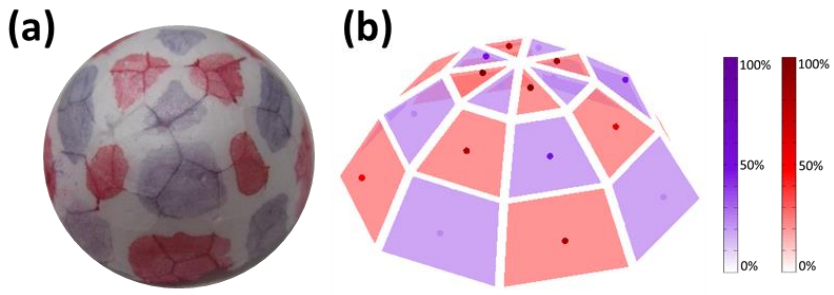

Figure 5.5. Optical image of small polystyrene hemisphere (a) imaged by sampling one point per dye spot and corresponding RoPPI-MS image (b).

Mass spectral data is converted into a 3D chemical information mesh by integrating the extracted peak area from each sampled point and pairing that with the x, y, z coordinates. This information is plotted using the scatter3 function in Matlab® and translating sampling coordinates to points on the mesh of the hemisphere created (Figure 5.5b). As the area sampled by the acupuncture needle is smaller than the sample spacing (1 mm), the signal observed was plotted as circles whose diameter reflect the precision of the measurement. These points are overlaid on a hemisphere showing the theoretical distribution of the dye painted on the surface. Peak area was converted into a pseudocolor intensity map used in the fill of each data spot. For ease of visualization of the dye data, two separate scale bars were set within the primary color map for each color component painted on the surface. For all data shown here, the purple scale denotes the ion intensity for Nile Blue Chloride and the red scale corresponds to Rhodamine 6G.

5.4.4 Increased Robotic Precision and Spatial Resolution

Following these early experiments, the Kuka KR5 sixx R650 robot (Figure 5.6) was implemented. This higher-precision robot comprised 6 degrees of freedom, a greater range

of motion (650 mm) to accommodate larger samples, and motion precision of 0.02 mm. This robotic system was paired with a 3D point cloud visualization system mounted on the robot arm (Figure 5.2f) to allow for user-selectable sampling position (Figure 5.2b). In between each point of analysis, the robot returns to the home position hovering above the sample (Figure 5.2b, 5.6) to allow the user to select a new point in the 3D point cloud image. Given a constant home position, the point cloud generated is the same for each analysis sequence, which facilitates full surface coverage. Although the robotic arm has a precision of 0.02 mm, which defines the maximum resolution of the technique, the resolution of the current 3D point cloud limits sampling to points with 1 mm spacing. The sampling and analysis process of this new system may be viewed as a video included in the Electronic Supporting Information.

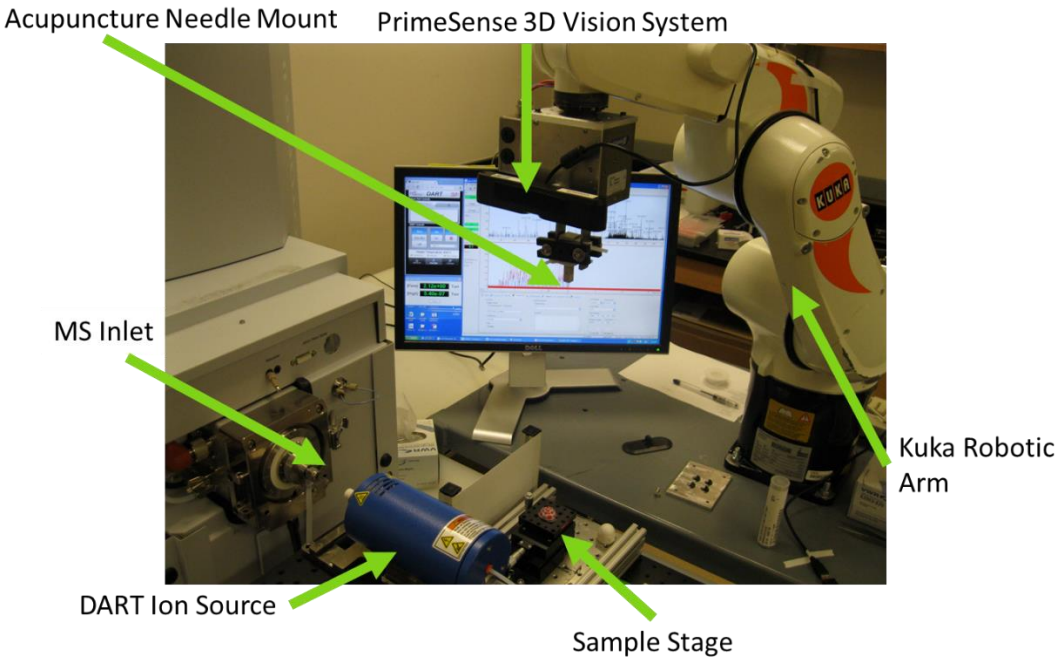

Figure 5.6. Picture of the RoPPI system employing the Kuka KR5 sixx R650 robotic arm. In this snapshot, the robot is in the "home" position to generate the 3D point cloud of the sample surface for sampling coordinate selection.

Using the 3D vision system input, the new x, y, z coordinate is specified for each analysis sequence so that the robot automatically probes the new position. This eliminates the need for manual adjustment of the sample position as in the early experiments because the robot is now easily capable of precise motion across the entire surface through more advanced programming. Given the defined home position, the robot still probes the sample surface orthogonal to the sample stage resulting in various approach angles, but the accuracy of the robot motion is sufficient to ensure reproducible sampling. Despite these improvements in the sophistication of the method, the 3D sensor is limited in the z dimension resolution (1 mm at optimal configuration), which often results in a noisy point cloud generation, particularly at surface boundaries. Even so, the depth to which the acupuncture needle punctures the surface is still more precise with this combination of vision system and robot than manual adjustment of the sample (puncture depths ranging from 1-5 mm).

This second set of 3D surface sampling experiments was conducted on a larger polystyrene hemisphere (30 mm diameter) that was also hand-painted with the same dyes. The top-down view seen through the 3D vision system and the sampled area are illustrated in Figure 5.2g and 5.7a, respectively. This sampled area resulted in 128 evenly-distributed data points that were also plotted (Figure 5.7) using Matlab® following the same procedure described above. The variable intensity detected within each painted region and the irregularly-shaped boundaries are mainly attributed to the hand painting of the sample because the increased precision of the robot motion should also increase the reproducibility of the technique. The detection of dye ions outside the intentionally painted areas of the surface is attributed to the bleeding of the dye solution along crevices in the polystyrene.

These studies indicate the second robotic system provides the most accurate 3D chemical images of curved surfaces.

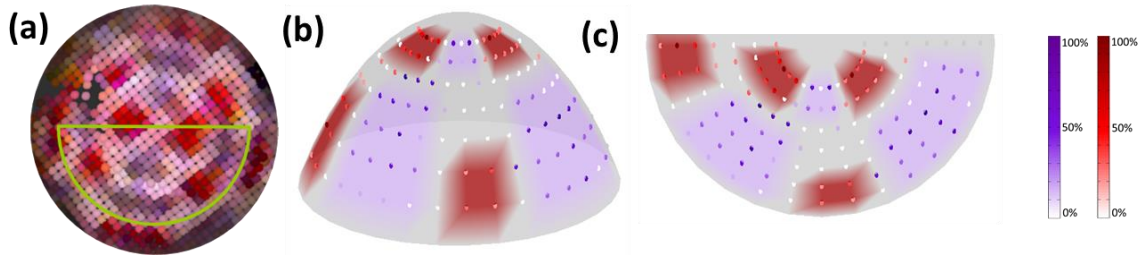

Figure 5.7. 3D point cloud top-view of large polystyrene hemisphere with area sampled outlined in green (a), and side-view of RoPPI-MS image acquired (b), and top-view of RoPPI-MS image (c); grey areas in (b) and (c) were not sampled.

5.5.1 Future Directions

Our lab is currently implementing a new RoPPI-MS system with a new robotic arm that is safe to operate in the presence of humans. This robotic arm, a Universal Robots (Odense S, Denmark) UR5 model offers 0.1 mm positioning repeatability and a more user-friendly interface. Several other improvements are also being made to the system for greater modularity and applicability. The generation of the 3D point cloud will be generated by "stitching together" snapshots of the sample from multiple angles, creating a more accurate point cloud at the boundary edges.

The probe used for surface sampling is being modified to accommodate different types of probes including a soldering iron for thermal desorption or a fiber optic for laser ablation. This modification is essential to be able to tailor the sampling probe for the type of sample and desired application; a solid acupuncture needle would not be efficient for extracting analytes from a hard or dry surface, therefore alternative sampling is necessary.

Based on different surface sampling probes used, a new sample introduction system is also being designed to more efficiently collecting sample material. A line with moderate suction is being used to transport desorbed analytes into the ionization region of the DART source. Alternatively, this line may be introduced into to the ionization region of an extractive electrospray (EESI)[254-255] which may offer greater sensitivity. Extensive characterization of the analytical figures of merit of the optimized system will be reported in the future.

5.5. Conclusion

A new mass spectrometry surface analysis technique, RoPPI-MS, is first described for the investigation of non-planar samples. The use of an ionization technique without enclosures such as DART enables easy and repeatable injections of the probed material into the plasma region. RoPPI-MS opens new avenues for examining in vivo tissues, organisms as they grow, classifying human skin lesions, probing 3D cell cultures, high-throughput baggage screening, monitoring produce safety, etc. We recognize that the resolution in the current system can still be improved, mainly arising from limitations of the robotic arms and probes utilized. This is not a drawback of the concept per se, but of the specific implementation used in these proof-of-principle experiments.

CHAPTER 6. DetectTLC: A TOOL FOR TURNKEY REACTION MIXTURE SCREENING ON THE BASIS OF AMBIENT MASS SPECTROMETRIC IMAGES

Adapted from

Kaddi, C. D.;* Bennett, R. V.;* Paine, M. R. L.; Weber, A. L.; Fernandez, F. M.;§ Wang, M.D., § DetectTLC: A Tool for Turnkey Reaction Mixture Screening on the Basis of Ambient Mass Spectrometric Images. In preparation for Angewandte Chemie.

* Equally contributing authors

§ Co-corresponding authors

6.1 Abstract

One of the first applications of ambient imaging mass spectrometry (MSI) was to thin layer chromatography (TLC) plates and MSI has since proven to be a comprehensive method of characterizing the separated chemical mixtures. User-guided investigation of MSI data for mixture components with known m/z values is generally straightforward; however, spot detection for unknowns is rather tedious and has limited the applicability of mass spectrometric imaging for TLC plate analysis. For complex reaction mixtures, an understanding of all chemical products is essential for the comprehensive investigation of reaction mechanisms. Therefore, we developed DetectTLC, an automated approach that identifies m/z values exhibiting spot-like shapes in mass spectrometric images. This automated approach reduces data processing time from days to minutes and increases the number of spot-like features found in MSI datasets. Furthermore, advances in mass spectrometry instrumentation now allow for multi-modal analysis in which alternating scans are acquired in different modes of operation, i.e. alternating between a low-energy (parent ion) and high-energy (fragment ions) scans. Without precursor mass selection, correlating parent and fragment ions is impossible. DetectTLC is also capable of

correlating spots observed in the two modes of operation without precursor mass selection based on the spatial distribution of m/*z* values. Employing desorption electrospray ionization mass spectrometry (DESI-MS) as the ambient sampling method in conjunction with DetectTLC, we were able to identify and characterize previously unknown products of an abiotic pyrazine nucleic acid synthesis products. This nucleic acid synthesis is of great interest to prebiotic chemists and the origin of life community but the DetectTLC software package is also expected to be extremely useful for any application that benefits from fast TLC separations or for reaction monitoring purposes.

6.2 Introduction

In the search for a prebiotically-relevant abiotic synthesis of informational biopolymers such as DNA and RNA, it is reasonable to expect that functionally-similar but chemically-unique species were made first, then evolved into the structures observed in modern biology. These synthetic routes typically produce a large and complex inventory of chemical species rather than a single product of prebiotic relevance, and only a select few capable of reacting further to form larger-order structures. The reaction products are not necessarily identical to the nucleobases and phosphate backbones observed today, but rather molecules such as pyrazine nucleic acids (PzNA) composed of pyrazin-2-one (PZO) and 2-aminopyrazine (APZ) monomers that are potentially autocatalytic and capable of self-assembly, providing alternate routes to self-replicating entities.[256]

As is common practice in synthetic chemistry, preliminary screening of these complex prebiotic reaction mixtures is often performed via thin layer chromatography (TLC)[257] due to its robustness and simplicity. Routine visualization of TLC plates uses dyes or fluorescence to identify spots corresponding to the separated components.[258] These

approaches are rapid, but lack chemical specificity. For a more comprehensive analysis of TLC plates, mass spectrometry (MS) may be employed through extraction or direct probing of the plate surface.[259-262] Direct MS can be performed statically on a few select spots, or dynamically in microprobe MSI mode; the latter eliminating the need for knowing a priori where the separated compounds are located. MSI of 2D high performance (HP) TLC plates has been demonstrated with a variety of approaches, including matrix assisted laser desorption ionization (MALDI)[263] and desorption electrospray ionization (DESI),[89, 220] among others.[69, 264]

Targeted interpretation of MSI data from HPTLC plates is straightforward if m/*z* values of analytes of interest are known; images of these m/*z* values are simply extracted from the (x,y,m/z) data cube. However, untargeted detection of unknown or unexpected species can be much more challenging as the datacubes generated by MSI experiments typically contain thousands of chemical images. Under these circumstances, extracting the useful information from MSI data can easily take hours or even days. An automated program to detect spots in a MS image of an HPTLC plate would significantly reduce processing time of information-rich datasets such as these. Algorithms commonly used in MSI data analysis have included principal component analysis (PCA),[6, 265] non-negative matrix factorization (NMF),[171] and clustering,[266] but these approaches are not intended for detecting the many individual components that would be present in a TLC separation. Therefore, we developed a new software tool for automatically detecting individual spots on the TLC MSI images, named DetectTLC. The core assumption within DetectTLC is that m/*z* images containing spots are distinguishable from other images on the basis of quantitative image features.

6.3 Experimental Details

6.3.1. Synthesis and TLC Separation of PZO Monomers

The pyrazin-2-one (PZO) products were prepared by heating at 85°C for 2 days a solution containing 0.10 M 1,3-dihydroyacetone, 0.10 M glycolaldehyde, 0.10 M alanine amide, and 0.25 M aqueous sodium phosphate (pH 7.4) in sealed headspace-deaerated ampules (Scheme 6.1). Three hundred microliters of the reaction product solution was desalted using an Alltech Ultra-clean SPE-C18 column (500 mg). The salts were eluted with water (1.4 ml) that was then discarded. Reaction products remaining on the column (incl. pyrazinones) were eluted with 3.5 ml 12% aqueous methanol, the eluent concentrated in vacuo, and separated by 2D-TLC using Merck HPTLC Silica gel 60 RP-18 W plates eluted using two solvent systems: the eluent for system "A" was aqueous 0.2 M acetic acid:methanol (5:1) in the first dimension of separation followed by trichloromethane:methanol (5:1) in the second dimension; the eluent combination for the system "B" was aqueous 0.2 M acetic acid:methanol (5:1) solution for the first dimension of analysis followed by trichloromethane:methanol:water (6:4:1) mixture in the second dimension.

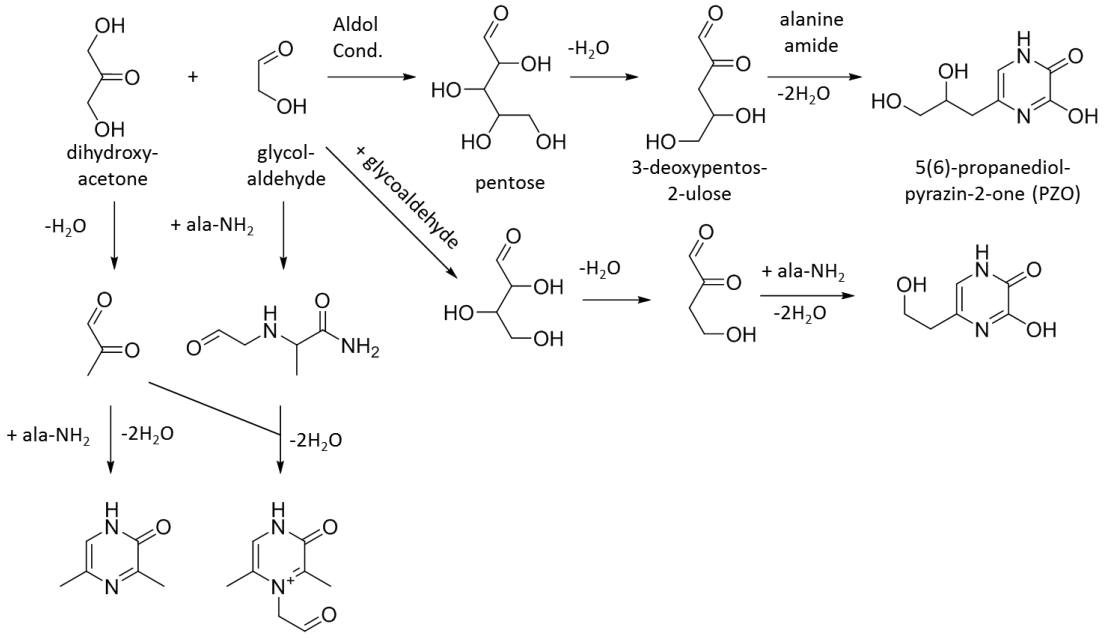

Scheme 6.1. Abiotic "one-pot" synthesis of pyrazin-2-one (PZO) monomers as alternative nucleobases.

6.3.2. Synthesis and TLC Separation of APZ Monomers

The 5(6)-(2,3-dihydroxypropyl)-2-aminopyrazine (APZ) monomer was synthesized (Scheme 6.2) by heating for 1 day at 85°C a 1.2 ml solution of 0.10 M dihydroxyacetone and 0.10 M glycolaldehyde, 0.10 M 2-aminoacetamidine-dihydrobromide (adjusted to pH 7.4 with NaOH), and 0.25 M sodium phosphate (pH 7.4) contained in a 2 ml glass vacule that was sealed in vacuo after being frozen and deaerated by cycling four times between a vacuum and nitrogen gas. A 1.0 ml aliquot of the reaction product was diluted to 8 ml with water. Five milliliters of the diluted solution was desalted using a 20 ml (5 g) Discovery DSC-18 column (Supelco) that was eluted with water (0-56 ml) and then 50% methanol in water (56-80 ml). Four ml fraction were collected and salt-containing fractions 0-9 (0-36 ml) were discarded. Fractions 10-20 (37-80 ml) were pooled

and concentrated to 0.5 ml using a CentriVap centrifugal concentrator. Two dimensional thin layer chromatography of the reaction was carried out by applying a 3 µl aliqout of the desalted, concentrated reaction solution to two Merck HPTLC RP-18W plates that were developed in the first dimension using 0.20 M ammonium acetate / methanol (5:1 v/v), and in second dimension with chloroform / methanol (10:1.4 v/v).

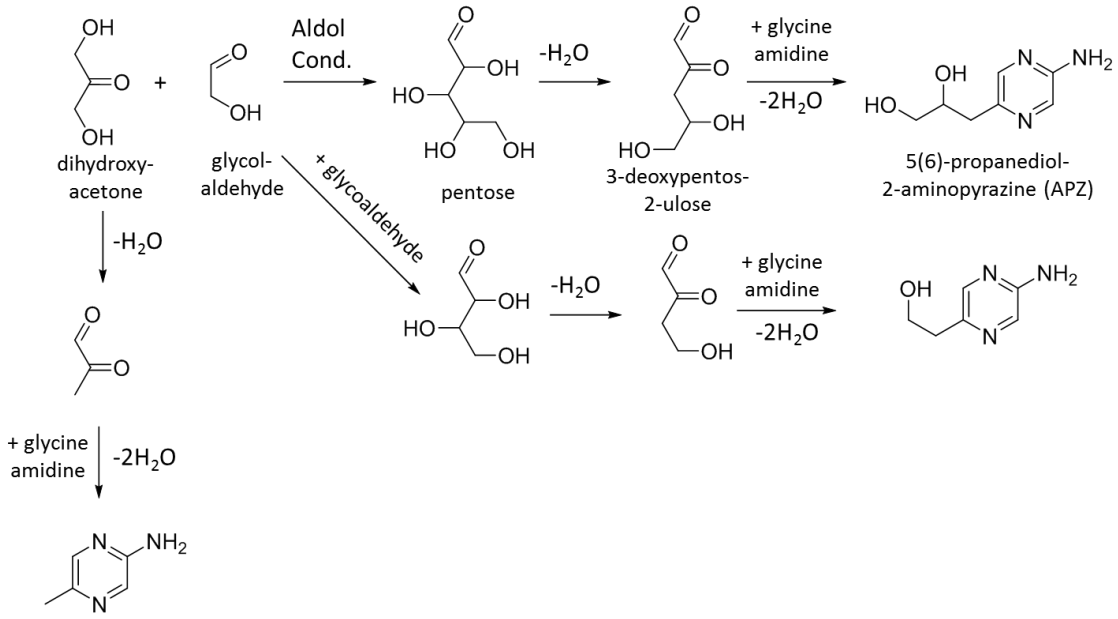

Scheme 6.2. Abiotic "one-pot" synthesis of 2-aminopyrazine (APZ) monomers as alternative nucleobases.

6.3.3. Fluorescent Visualization of TLC Plates

The fluorescent spots on the TLC plates, illuminated by a Spectroline UV-312 nm transilluminator, were captured using a Sony NEZ-5R camera. NIH's ImageJ image processing program (http://imagej.nih.gov/ij/) was used to split the RGB images into their

red, green, and blue channels, and subtract the background of the depicted blue channel image.

6.3.4. DESI-MSI of TLC Plates

Mass spectrometry images were acquired using combinations of two ion source/imaging stages and mass spectrometers to demonstrate the ability of DetectTLC to process datasets from instruments with different spatial and mass spectral resolution. The PZO synthesis mixture was imaged using a 2D OmniSpray automated DESI ion source (Prosolia Inc., Indianapolis, IN) coupled to a Synapt G2 HDMS mass spectrometer (Waters, Milford, MA) in positive-ion mode. The m/z range acquired for each pixel was 50-250. A DESI spray of 1% acetic acid (ACS Reagent grade, Sigma-Aldrich, St. Louis, MO) in acetonitrile (OmniSolv® LC-MS Grade, EMD Millipore Corporation, Billerica, MA) with a flow rate of 5 μL min^{-1} and a N_2 nebulizing gas (150 psi) was used for maximum sensitivity and minimal impact spot size. Stage motion was programmed such that data was acquired in 200 μm × 200 μm pixels for a total image size of 30 mm^2. Mass spectral data was converted using Firefly conversion software (Prosolia, Inc., Indiandapolis, IN) into Analyze 7.5 format and images were visualized using omniSpect (http://omnispect.bme.gatech.edu/)[171] and DetectTLC.

The APZ reaction mixture was imaged using an OmniSpray DESI probe (Prosolia Inc., Indianapolis, IN) spraying acetonitrile at a flow rate of 8 μL min^{-1} and a N_2 nebulising gas pressure of 130 psi. The sample was rastered using a motorized microscope stage (OptiScan II, Prior Scientific Inc., Rockland, MA) controlled by a Labview VI described elsewhere[171-172] moving at a speed of 160 μm s^{-1} with a line step of 200 μm. Mass spectra were acquired on an Exactive Plus mass spectrometer (Thermo Scientific, San Jose, CA)

in positive-ion mode with mass resolution set to 35,000, alternating each scan between Full MS (no Collision Energy applied) and All-Ion Fragmentation (AIF, CE=60) modes. There is no precursor ion selection during AIF scans prior to higher-energy collision-induced dissociation (HCD), therefore all ions entering the HCD cell are fragmented and detected. In this manner, every other pixel in the MS image represents ions from the alternating modes. The dataset may be visualized as (1) a complete dataset with pixels from both modes included or (2) as separate Full MS or AIF images after separating the scan modes using Xcalibur software (Thermo Scientific, Inc.). Data was converted to the .mzxml format using ‘msconvert‘ for visualization using omniSpect and DetectTLC.

6.3.5. Ultra-High Performance Liquid Chromatography-Tandem Mass Spectrometry of APZ Mixture

The desalted APZ reaction mixture was diluted 50x in ultrapure water (18 MΩ cm). Chromatographic separation was performed using a Waters ACQUITY UPLC H Class system fitted with a Waters ACQUITY UPLC C_{18} column (2.1 x 50 mm, 1.7 μm particle size) coupled to a Synapt G2 mass spectrometer (Waters Corp., Manchester, UK). The chromatographic method for sample analysis involved elution with 0.1% acetic acid in water (mobile phase A) and acetonitrile (mobile phase B) at a flow rate of 0.2 ml min^{-1} using the following gradient program: 0-5 min 98% A, 5-6 min 80% A, 6-7 min 98% A. The sample injection volume was 10 μL. Mass spectra were acquired in positive ion mode with a mass range m/z 50-1000, and CE = 20 for fragmentation.

6.3.6. DetectTLC Development

All DetectTLC develpment was done in MATLAB (MathWorks, Natick MA). DetectTLC utilizes a five-step processing pipeline. First, two-dimensional median filtering and pixel count-based filtering are applied to each m/z image in order to remove spatially disperse, low-intensity noise and to remove sparse or high-intensity noisy images, respectively. The images that pass this step are then thresholded to binary images in order to identify spot-like regions regardless of signal intensity. This facilitates the detection of low-abundance species that are separated by TLC, and leaves the decision of significance to the user. Third, a morphological image processing operation (dilation or opening) is applied to smooth heterogeneous pixel clusters into spot-like regions, thus correcting for signal variability and enhancing the quantitative image feature-based detection method. Fourth, quantitative image features are used to score each m/z image on the basis that it contains a spot. Eight image features are currently available in DetectTLC, seven of which are shape-based (area, compactness, convex area, eccentricity, extent, number of connected regions, and solidity) and the eigth is texture-based (entropy). Each of these steps are automatically performed during routine analysis using two preset protocols, one tailored to identify larger TLC spots, and one for smaller spots, both with no user input required. Finally, m/z images are ranked in terms of their feature values and visualized in the DetectTLC graphical user interface (GUI).

Detect TLC can be downloaded from the following address: centerforchemicalevolution.com

6.4 Results and Discussion

6.4.1. DetectTLC Workflow

The DetectTLC workflow is shown in Figure 6.1, and below is a complete description of the processing steps used for spot finding from TLC-MSI datasets.

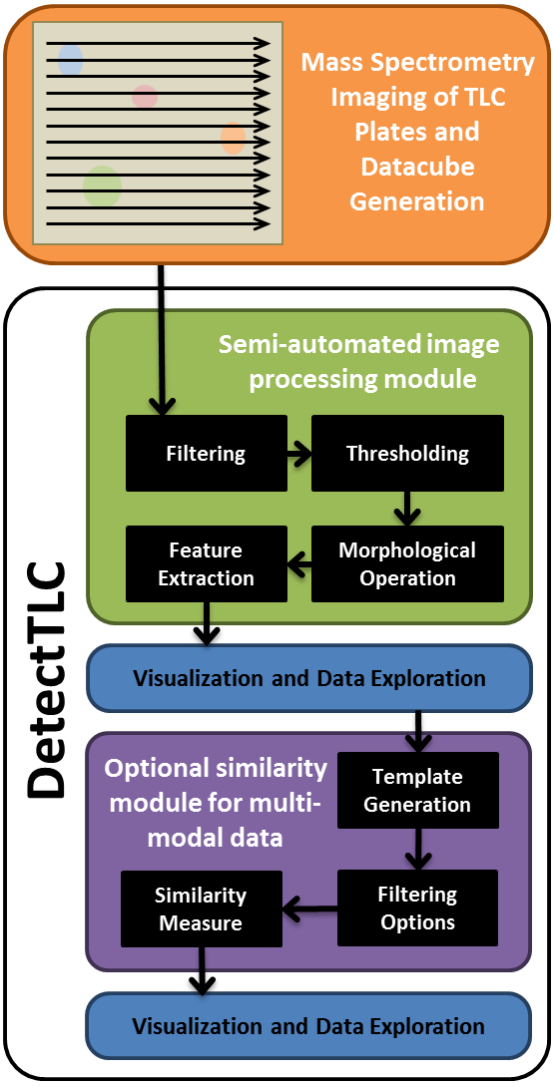

Figure 6.1. Overview of the workflow used in the DetectTLC software tool.

Step 1: Smoothing and Pixel-count Filters

Median filtering[267] was used to remove background noise. For the MSI datasets examined in this study, 5×5 and 7×7 median filters were compared, but the difference in performance was small compared to the effects of other factors, so results from 7×7 median filters are shown. Median filtered-results are also compared with un-filtered results.

The pixel-count-based filter was useful for removing sparse and streak-filled images from consideration. It was observed that many DESI-MS images were sparse or streak-filled due to the constant chemical background produced by the DESI spray. In different datasets, the necessity of performing this filtering step may vary, as few such images may exist. Typically, binary m/*z* images with fewer than 5 and more than 1500 non-zero pixels were removed from consideration.

Step 2: Generating Binary Images

Two different methods for generating binary images were compared in this study. The first method is a manually-selected threshold: if any signal S was present at a pixel (x, y) in the original m/*z* image above the threshold value T (i.e., $S(x, y) > T$), the value of the pixel in the binary image $B(x, y) = 1$. Otherwise, $B(x, y) = 0$. Users may select the desired threshold through the Advanced Options menu of the DetectTLC interface, which also provides a visualization of the selected threshold with respect to the average spectrum of the dataset. The second technique is Otsu's method, which selects the threshold at which the within-class variance of the pixels assigned to each label is minimized.[268]

Step 3: Morphological Operations

An m/*z* image may feature a spot-like region that is not solid, i.e., single pixels or clusters of a few pixels where no or low signal was detected may occur between pixels

where signal was detected. This area may be interpreted as a single spot-like region by an expert user with knowledge of the predicted chemistry. However, these heterogeneities can influence the automated, image-feature based detection of spot-like regions. To address this issue, DetectTLC applies morphological image processing operations to the MSI dataset. Erosion and dilation are two basic morphological operators used in image processing.[269] A structuring element of a particular shape – common shapes include disks, squares, and diamonds – is used to remove (in erosion) or add (in dilation) a layer of pixels from the image. The compound morphological operators of opening and closing are defined in terms of erosion and dilation: in opening, erosion is followed by dilation, and in closing, dilation is followed by erosion. In this study, we compared the performance of dilation and opening in generating homogenous spot-like regions: dilation fills in small holes in a single region and gaps between regions, while opening also removes connections between separate regions.

Step 4: Scoring Based on Quantitative Image Feature Values

The performances of eight quantitative image features were investigated and compared in the development of DetectTLC. These included seven shape-based features: area, compactness, convex area, eccentricity, extent, number of connected regions, and solidity; and one texture-based feature: entropy. Each of these features is described further in Table 6.1.

Table 6.1. Definition and description of image features investigated in the development of DetectTLC.

Image feature	Definition	Description
Area (*A*)	$A = \sum f(x)$, where x represents pixels with a value of one in the binary image, and f is a neighborhood operation function.	This feature is the weighted sum of pixels with a value of one in the binary image. Different spatial distributions of pixels are weighted. Images containing a spot-like region may have lower area values than images with other structures.
Compactness (*Co*)	$Co = P^2 / A$, where P is the perimeter of the non-zero region and A is its area.	Compactness is a regional descriptor defined as the ratio of an object's squared perimeter to its area. Compactness is minimal for disk-shaped regions (Gonzalez and Woods, 2002), so images with a spot-like region may be characterized by lower compactness values.
Convex area (*Ca*)	$Ca = \sum x$ where x represents pixels which are in the convex hull of the image.	The convex area is the number of pixels inside the convex hull, which is the smallest convex polygon that contains the entire region of non-zero pixels. A smaller convex area implies a small, cohesive region of interest, so images containing a spot-like region may be characterized by lower convex area values.
Eccentricity (*Ec*)	$Ec = Dc / Dv$, where Dc is the distance from the center to the focus of the ellipse, and Dv is the distance from the center to a vertex.	Eccentricity is calculated by fitting an ellipse to the region of interest, such that the ellipse and the region share the same second moments. The image feature is then the eccentricity of the fitted ellipse. For a circular region, eccentricity would be 0; for a line it would be 1. Images containing a spot-like region may be characterized by lower eccentricity values.

Table 6.1. Continued

Image Feature	Definition	Description
Entropy (*En*)	$En = -\sum p_i log_2(p_i)$, i = 0...1, where p_i represents the fraction of zero (i = 0) and non-zero (i = 1) pixels in the image.	Entropy is a measure of randomness used to describe image texture. For binary images, entropy is defined in terms of the fractions of zero and non-zero pixels. The quantity is maximized when the fraction of each pixel type is equal, so images with larger spot-like regions may be characterized by higher entropy values.
Extent (*Ex*)	$Ex = \sum x / \sum B$, where *x* represents pixels which are within the region, and *B* represents all pixels which are within the bounding box.	Extent is defined in terms of the bounding box, which is the smallest rectangular region that completely encloses the region. Extent measures the proportion to which the region of interest fills the bounding box. Images with a spot-like region may be characterized by higher values of *Ex.*
Number of connected regions (*Re*)	$Re = E + H$, where *E* is the Euler number and *H* is the number of holes.	The number of connected components is related to the Euler number (*E*), a commonly used shape-based image feature. The Euler number is defined as the difference between the number of connected components and the number of holes (*H*). In an image with solid spot-like feature, ideally there would be no holes ($Re = E$), so the number of connected components was considered as a feature instead of Euler's number. Images with several distinct spot-like regions may be characterized by higher values of *Re.*
Solidity (*S*)	$S = A / Ca$, where *A* is the image feature Area and *Ca* is the image feature Convex area.	Solidity is a composite feature, defined in terms of Area and Convex Area. This image feature measures the fraction of pixels which are in both the convex hull and the region of interest. Images with a spot-like region may be characterized by higher values of *S.*

6.4.2. DetectTLC Graphical User Interface

The DetectTLC user interface comprises four windows, with the main window shown in Figure 6.2. This window displays the spot-containing images identified through different algorithms, and contains a control panel for accessing the "Load New Dataset", "Advanced Options", and "Similarity Options" menus. Algorithm results are displayed on the main graphical user interface (GUI), 24 m/*z* images at a time. After running a processing protocol, images are initially sorted based on a quantitative image feature-based score. Within each window, they may be re-sorted by ascending m/*z* value for convenience. A scroll bar is used to scan though all images, which may also be visualized with alternate color schemes if desired. Additionally, the user can narrow the examined mass range for more targeted examination of images containing spot-like regions. The key options in the DetectTLC GUI are described in further detail below.

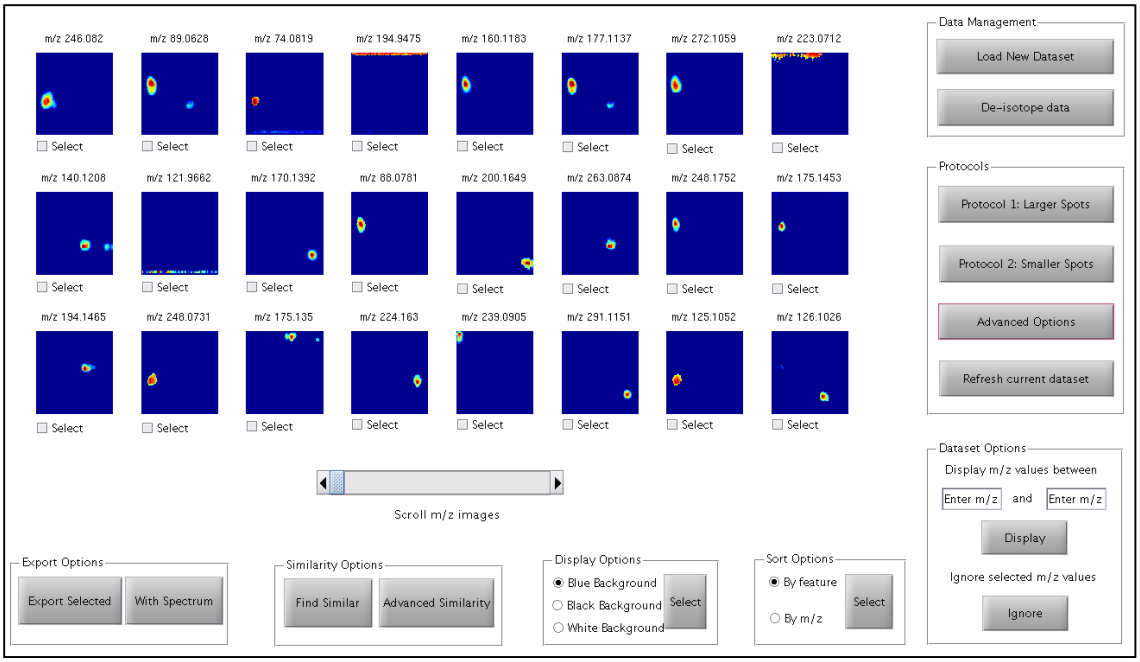

Figure 6.2. The main graphical user interface with the top 24 images containing spot-like regions displayed. Data is first uploaded and (optionally) de-isotoped, following which the user may select from Protocols 1 or 2 for feature selection, or design their own processing pipeline through the Advanced Options tab. Spots with similar spatial distributions may be identified using the Similarity Options. Selected images and/or spectra may be exported using the Export Options.

Load New Dataset

DetectTLC accommodates MSI data in Analyze 7.5 and mzXML format (with time and position information). It also accepts MSI data which have been imported into MATLAB and saved as matrices in '.mat' files. Thus, other MSI data formats can also be used with DetectTLC if they are first imported into MATLAB.

De-isotope data

DetectTLC currently uses a basic de-isotoping algorithm in which the highest-intensity m/z value in each 3 Da-window is retained. Each spectrum is de-isotoped individually, and the spectra are then re-assembled into a de-isotoped datacube. This de-isotoping is used to remove isotope ion images from the DetectTLC output, which would

result in redundancies in the spot list and often rank unique species lower in the outpu. The large m/z range used for this step risks eliminating low-abundance species that overlap with higher-intensity peaks, therefore the user must be careful when performing this step and weigh the risk. With DetectTLC being intended for TLC plates, ideally the spot separation is sufficient to prevent elimination of key signals. After de-isotoping is performed, all further processing protocols will automatically be performed on the de-isotoped data. In order to return to the raw data (with no de-isotoping), it is necessary to re-load the data files.

Pre-set automatic protocols

Two automatic protocols are offered. The first, "Protocol 1: Larger spots", uses entropy as the quantitative image feature for scoring. The second, "Protocol 2: Smaller spots", uses compactness as the image feature. The default settings for filtering by intensity, filtering by non-zero pixels and median filtering are implemented in both of these protocols.

Refresh current dataset

By pressing the "Refresh dataset" button, the user can return the display to the original MSI data before any processing protocols (pre-set or via the advanced options) were applied. If the dataset had been de-isotoped, the de-isotoped data will be shown.

Find m/z values

This option displays all images corresponding to the user-input m/z range. Note: any processing steps that are called after the "Find m/z values" command will operate only on the images within that m/z range. To process the entire dataset, it is necessary to press the 'Refresh dataset' button first.

Ignore m/z values

This feature can be used to select m/z images which are not of interest to the user (e.g., noisy images, or images with homogeneous signal intensity) and remove them from the current dataset view. The original MSI data can be retrieved by using the "Refresh dataset" option.

Export (with or without average spectrum)

Two different export utilities are available in DetectTLC: (1) Export Selected Images and (2) Export With Spectrum. In (1) Export Selected Images, the user can use the checkboxes below each m/z image to make selections, and then click the button labeled "Export Selected Images". All selected images will be saved in '.fig' format to the user-specified directory, and an ASCII file listing the selected m/z values will be created in the same directory. Multiple m/z images within one screen (24 images) can be exported simultaneously. In (2) Export With Spectrum, the user will instead click the button labeled "With Spectrum". A new figure will appear, showing the selected m/z image. The user can use the drawing cursor to select a region of interest by drawing a line through the spot-like region or around it. After the region of interest is selected, a composite figure containing both the m/z image and the average spectrum in the region of interest (Figure 6.3) will be saved as a MATLAB '.fig' file in the user-specified directory. Again, multiple m/z images (24 per screen) can be selected simultaneously. If multiple m/z images are selected, the process of manual region of interest selection will be repeated for each image, and an ASCII file listing the selected m/z values will be created in the same directory.

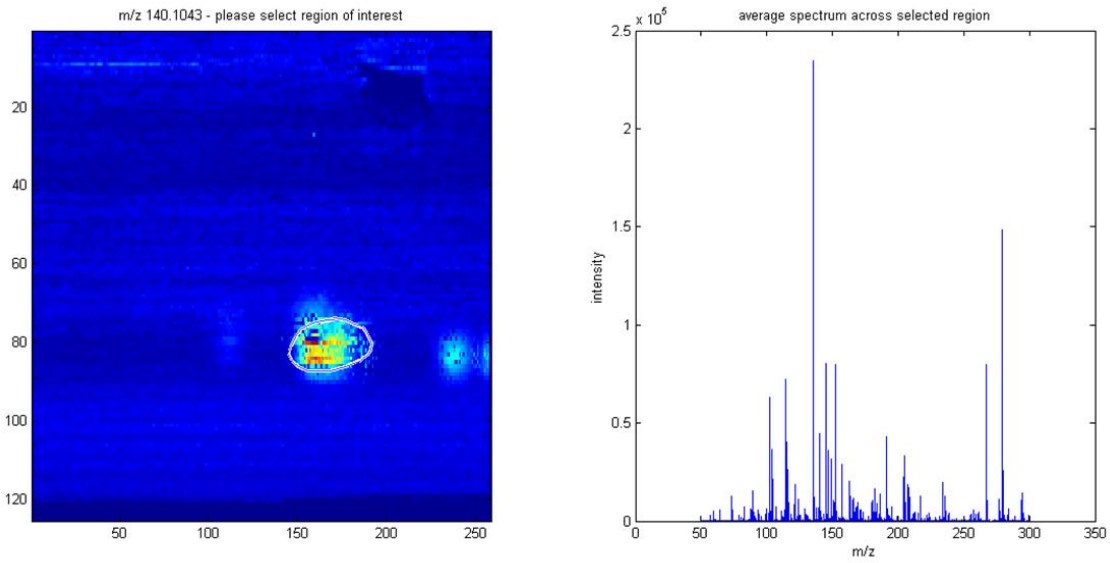

Figure 6.3. Image selected with m/z 140.1043 to draw a region of interest (ROI, outlined in white) and resulting average spectrum for selected pixels.

6.4.3. Advanced DetectTLC options

The Advanced Options GUI (Figure 6.4) provides users with more control over how the MSI data is processed and analyzed. Four different pre-processing control panels are available: (1) Generation of binary images; (2) Pixel-count filtering; (3) Median filtering; and (4) Image feature selection.

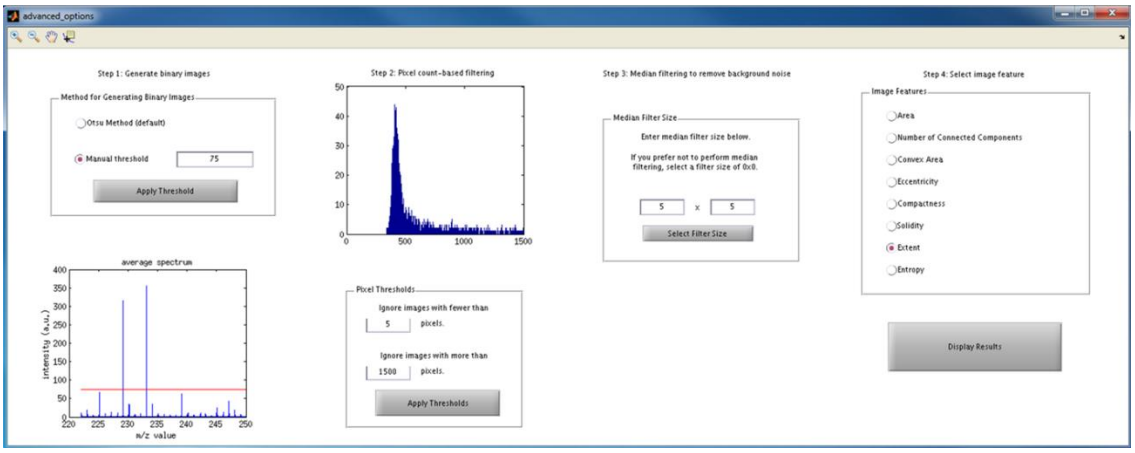

Figure 6.4. Advanced Options GUI in DetectTLC.

In DetectTLC, morphological operations and image feature scores are computed on binary m/z images. In the "Generation of binary images" control panel, the user has the option of using Otsu's method (default) or manually selecting a threshold for generating binary m/z images. The success of the thresholding process is highly dependent on spectral signal-to-noise; it is valuable to identify genuine spots that may have low abundance, but that are still sufficiently above baseline noise. The average spectrum across the MSI dataset is displayed below the thresholding panel in the GUI, and when the "Apply" button is clicked, the manually-selected threshold is overlaid on the spectrum as a red line.

The "Pixel-count filtering" control panel can be used to eliminate sparse images and so-called streaky images. In the MSI dataset analyzed in this paper, sparse images were generated as a result of the centroiding process. These images were eliminated by establishing a minimum of 5 pixels for a spot to be detected. Conversely, no more than 1500 pixels for a particular m/z could be present for a true spot, as the presence of that many pixels indicated streaks or widespread presence of a species across the entire TLC plate (e.g. an impurity in the DESI solvent). For general use, a histogram showing the

distribution of m/z images with different numbers of non-zero pixels is displayed. The user can refer to this histogram to select the upper and lower thresholds for pixel-count filtering. When the "Apply" button is clicked, all m/z images containing a number of non-zero pixels above the upper threshold or below the lower threshold are discarded from the dataset. The default setting is to discard images with fewer than 5 non-zero pixels and with more than 1500 non-zero pixels.

In the "Median filtering of m/z images" panel, the user can select the size of the two-dimensional median filter applied to remove "salt-and-pepper" background noise from the m/z images. The default setting is a 5×5 median filter. If no median filtering is desired, the filter size should be set to 0×0.

The fourth and final panel allows the user to select from among the eight image features investigated in this paper: area, compactness, convex area, eccentricity, entropy, extent, number of connected regions, and solidity. The m/z images remaining after the filtering steps, sorted according to the selected image feature, will be displayed in the main GUI. Selection of the image feature of interest is independent of the three pre-processing options. It is not necessary to perform any pre-processing before applying the image feature-based sorting – the default settings of Otsu's method, < 5, > 1500 pixel-count filtering, and 5×5 median filtering will be applied. The three pre-processing steps can also be applied individually or in any combination prior to selecting an image feature.

6.4.4. Performance Evaluation of Alternative Pipelines

DetectTLC was designed with complex chemical reaction mixtures in mind, therefore various processing pipelines within its framework were assessed for their ability to identify TLC spots. Each possible image processing combination, 128 pipelines in all,

was evaluated based on the number of true spots identified in the top 40 images generated when applied to the PZO synthesis dataset. A full assessment of the results for all eight quantitative image features is included in Table 6.2.

Table 6.2. Performance comparison of all 128 alternative processing pipelines in identifying m/z images containing TLC spot-like regions among the top 40 rankings.

Evaluation	Binarization	Morphological Operation	None		7x7		Median Filtering
			None	5<x<1500	None	5<x<1500	Pixel Filtering
Area	Manual	Dilation	0	0	26	28	
		Opening	20	35	24	28	
	Otsu	Dilation	0	0	27	38	
		Opening	24	27	25	36	
Number of connected regions	Manual	Dilation	2	1	24	37	
		Opening	11	39	24	**40**	
	Otsu	Dilation	1	1	21	37	
		Opening	11	39	25	**40**	
Convex area	Manual	Dilation	2	2	24	28	
		Opening	15	37	38	**40**	
	Otsu	Dilation	2	2	24	37	
		Opening	15	35	36	**40**	
Eccentricity	Manual	Dilation	0	0	26	31	
		Opening	17	36	34	**40**	
	Otsu	Dilation	0	0	24	36	
		Opening	17	34	34	**40**	
Compactness	Manual	Dilation	0	0	27	30	
		Opening	23	37	39	**40**	
	Otsu	Dilation	0	0	26	38	
		Opening	20	31	39	**40**	
Solidity	Manual	Dilation	9	15	23	36	
		Opening	33	**40**	27	**40**	
	Otsu	Dilation	8	10	22	**40**	
		Opening	33	**40**	27	**40**	
Extent	Manual	Dilation	6	10	23	31	
		Opening	36	39	34	**40**	
	Otsu	Dilation	5	7	21	36	
		Opening	36	39	33	**40**	
Entropy	Manual	Dilation	1	3	24	**40**	
		Opening	18	**40**	24	**40**	
	Otsu	Dilation	0	1	24	39	
		Opening	18	39	24	**40**	

It was observed that, for thresholding purposes, Otsu's method and selected manual thresholds yielded comparable results across all other processing variables. The key difference between these two approaches is the need for user input required for manual thresholding versus the user-independent Otsu's method. In almost every combination of processing methods, morphological opening yielded a higher number of spot-containing images than dilation (on average twice as many true spots for all combinations). The other processing step that significantly affected the number of true spots identified was median filtering. For this dataset, the 7x7 median filter was found to perform better than no filter, or a 5x5 median filter; through the "Advanced Options" menu the user can input different filter sizes and select the most appropriate size for the dataset under analysis.

Ultimately, the analysis pipeline of (1) Otsu's threshold, (2) morphological opening, (3) 7×7 median filtering and (4) removal of images with < 5 and > 1500 non-zero pixels, provided the best results for the PZO dataset. Combining this pipeline with entropy as the image feature for ranking, two of the known products in the PZO reaction mixture were included in the top 5 images output by DetectTLC, and all three predicted products were within the top 40 ranked images. For other chemical systems, DetectTLC settings could be tailored to provide optimum results, and to obtain a complete list of m/z images containing spots.

As previously mentioned, the best results were returned by the analysis pipeline consisting of (1) Otsu's threshold, (2) morphological opening, (3) application of a 7×7median filter, and (4) removal of images with < 5 and > 1500 non-zero pixels. For all of the image features except area, all 40 of the top 40 ranked images contained TLC spot-

like regions. The difference among the feature measures is most clearly demonstrated by the variety and size of the spots identified, as illustrated to an extent in Figures 6.5.

To further investigate these differences, the overlap among the top 40 rankings between each feature pair is shown in Table 3. This comparison confirms qualitative observations: image features which returned m/*z* images with smaller spot-like regions, such as compactness (Figure 6.5a) and convex area, had similar top 40 lists (e.g., 34/40 in common). Meanwhile, entropy, which returned m/*z* images with larger spot-like regions (Figure 6.5b), and compactness had very different lists (e.g., 11/40 in common). Importantly, none of the image features were completely redundant in terms of their top 40 rankings. Image feature pairs which highlighted similar types (e.g. smaller or larger) of spot-like regions still returned unique m/*z* images. For example, entropy and extent both tended to highlight larger spot-like regions, but only 20/40 of their top-ranked images were in common. Thus, examining both of their top-ranked lists would be helpful during analysis, compared to considering only one image feature.

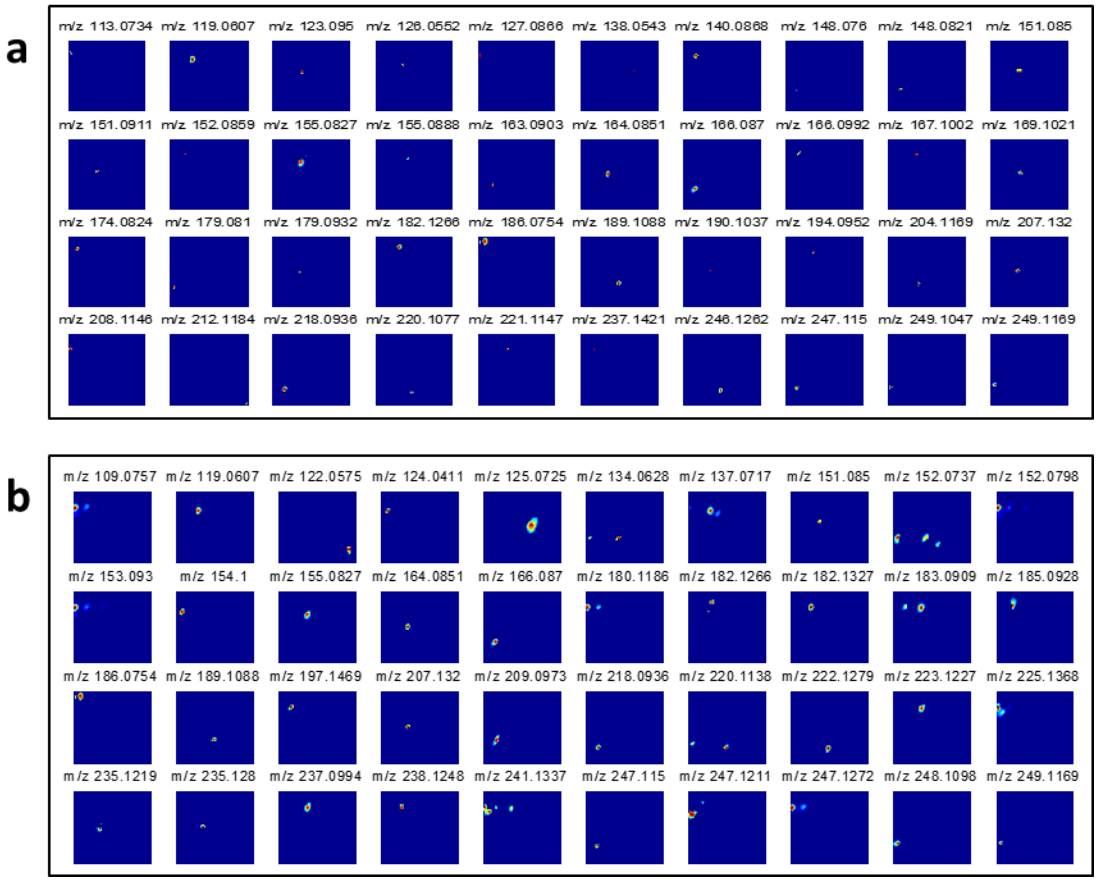

Figure 6.5. Example of the top 40 m/z image results generated by DetectTLC using different quantitative image features: (a) compactness, which feature smaller spot-like regions, and (b) entropy, which features larger TLC spot-like regions. The analysis pipeline used consisted of (1) Otsu's method for generating binary images, (2) morphological opening, (3) 7×7 median filtering, (4) removal of images with < 5 and > 1500 non-zero pixels, and (5) the respective image features.

Table 6.3. Number of common *m/z* images which are selected as among the top 40 selections by two different image features.

	Area	# Connected Regions	Convex Area	Eccentricity	Compactness	Solidity	Extent	Entropy
Area	40	16	26	17	26	7	18	0
# Connected Regions	-	40	24	23	23	21	26	21
Convex Area	-	-	40	28	34	14	27	11
Eccentricity	-	-	-	40	29	17	24	20
Compactness	-	-	-	-	40	15	25	12
Solidity	-	-	-	-	-	40	25	31
Extent	-	-	-	-	-	-	40	20
Entropy	-	-	-	-	-	-	-	40

6.4.5. DetectTLC to Find Spots in the PZO Separation

The synthesis of PZO and APZ monomers is of great interest to prebiotic chemistry and provided the reaction mixtures studied here (Scheme 1-2). These were used as an example to demonstrate the capabilities of DetectTLC applied to MSI data, but the approach is generally applicable. The fluorescence image obtained from the HPTLC separation of the PZO mixture using solvent system “A” is shown in Figure 6.6a. Three major PZO products of interest (#1-3) that had been previously identified (chemical structures shown in Figure 6.6b) were observed in the MSI data, and MS images could be generated manually (Figure 6.6c). Automated analysis of the MSI data using DetectTLC generated a series of ion images with spot-like regions corresponding to analyte spots on the TLC plate, including the known products as shown in Figure 6.6d.

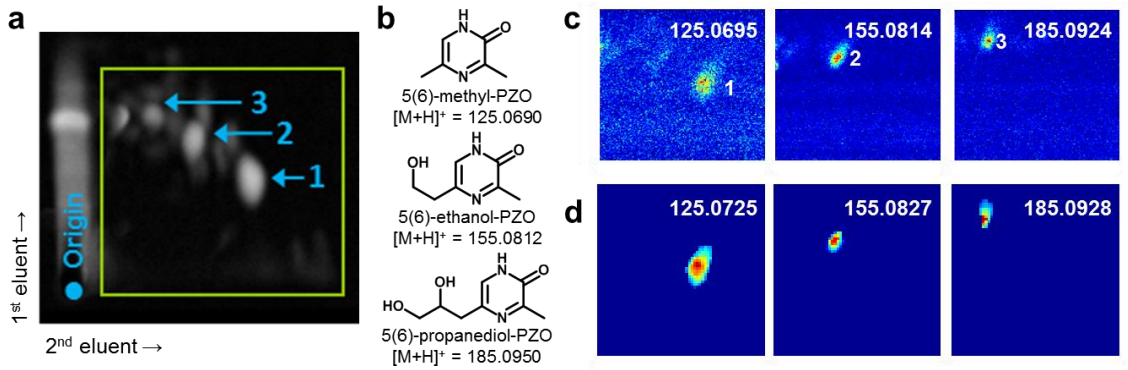

Figure 6.6. Fluorescence image of developed HPTLC plate with the area imaged by DESI-MSI outlined in green (a). Known products of the PZO reaction, with the numbers indicating the spatial location of each product in the fluorescence and MS images (b). Selected ion images acquired by DESI-MSI of reaction products previously identified (b) and the corresponding spot-like images as they were generated by DetectTLC using the pre-set Protocol 1 processing pipeline (d).

An average difference of 5 mmu between the accurate m/z values for the raw ion images and the DetectTLC images of the known products was observed, which was attributed to the centroiding process used in DetectTLC. Mass spectra were acquired in profile mode, and the m/z peaks observed are not truly Gaussian, therefore the local maximum m/z value observed in the profile spectrum differed slightly from the centroided m/z value.[270] Additionally, there are distinct differences in image contrast between the manual and DetectTLC images, which is due to the median filtering step removing background pixels in the DetectTLC output images, resulting in a higher apparent image contrast. In all, the DetectTLC output results for the separated PZO reaction mixture included upwards of 40 m/z images that displayed spot-like regions corresponding to additional reaction side products. The number of genuine spots found by DetectTLC, as curated by an expert user, was found to be dependent on the image analysis pipeline used, as described below.

One key benefit of DetectTLC is its ability to pinpoint key mixture components that would not be otherwise characterized. When the PZO mixture was separated by a second solvent system "B", an intense fluorescence spot different from spots 1-3 was detected; this compound was not observed with mobile phase system "A". DetectTLC was applied to the dataset generated with the new solvent system, and the results included an m/*z* = 167.0853 ion image with a spot co-localized with the fluorescent image, yielding a chemical formula of $C_8H_{11}N_2O_2$ ($\Delta m = 2.6$ mmu) for the analyte. Taking into consideration the reaction chemistry, the unknown species of interest was identified as 3,5(6)-dimethyl-4-oxoethyl-2-oxo-pyrazin-4-ium, a probable side reaction product (Scheme 1). The m/z 167.0853 image ranked 13th in the DetectTLC results, which would be displayed on the first page of 24 images in the main GUI window, making it straightforward for the user to select this ion as the analyte of interest. The fluorescence image, manually selected m/z images, and DetectTLC results for solvent system "B" are shown in Figure 6.7.

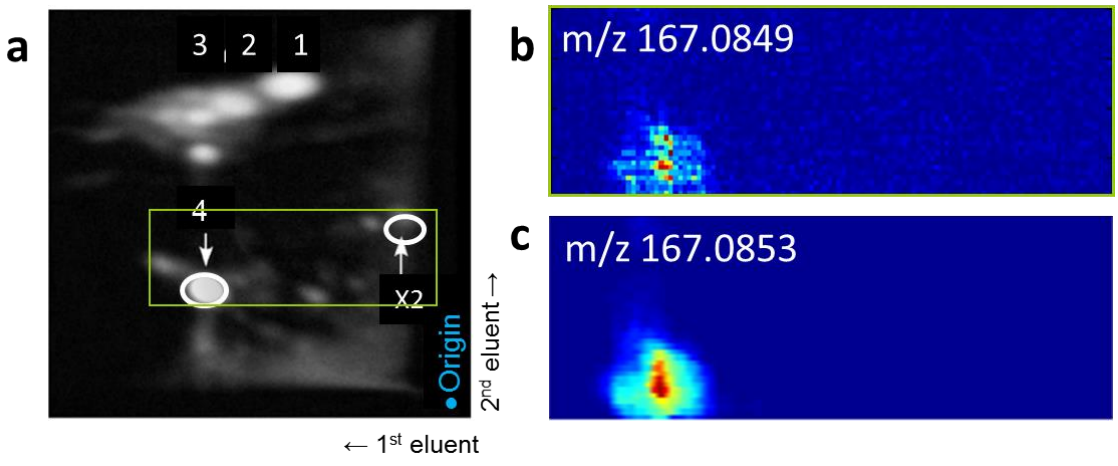

Figure 6.7. Fluorescence visualization of 2D HPTLC of PZO reaction mixture as separated by eluent System "B" indicating unknown Spot 4 (a), manually plotted image of m/z 167.0353 (b) and resulting image from DetectTLC identifying compound with m/z 167.0815 to be co-localized with Spot 4 (c). The area of the plate imaged by DESI-MSI is indicated in green.

6.4.6. Similarity Assessment for Matching Ions with Like Spatial Distributions in DetectTLC

To confidently assign analyte structures by mass spectrometry, MS fragmentation data must be used. Modern mass spectrometers now allow for data to be acquired in multiple modes sequentially, in pseudo-real time. For example, alternating between low- and high-energy scans enables acquiring data corresponding to precursor and product ions in a single acquisition cycle. In true tandem mass spectrometers, the precursor ion is first selected for fragmentation, but when many analytes are simultaneously ionized it becomes challenging to mass-select all individual precursor ions while maintaining high imaging throughput. To comprehensively fragment all ions, alternating low- and high-energy scans may be acquired and precursors may be matched to products based on similar 1D chromatographic profiles.[271]

DetectTLC includes similarity algorithms capable of automatically pairing precursors and product ions based on their similar spatial (2D chromatographic) distributions on the TLC plate, thus facilitating more confident assignment of analyte structures. This kind of similarity matching is performed in DetectTLC by first allowing the user to select the precursor ion spot of interest from a low-energy image. This region of interest is used to generate a template against which to measure similarity in the high-energy images using either Pearson correlation or the hypergeometric similarity measure.[272-273] The results are displayed as a set of ion images, but the user also has the option of generating an all-fragment mass spectrum displaying peaks for all m/*z* values with similar spatial distribution to the precursor.

Multiple methods for performing similarity analysis are available in DetectTLC. The most basic method, which is implemented by selecting any m/z image via its checkbox and clicking the "Find Similar" button, will return the most similar m/z images within the same dataset, as ranked by the hypergeometric similarity measure. Alternatively, by clicking the "Advanced Similarity" button, the Advanced Similarity Options window will open, as shown in Figure 6.8.

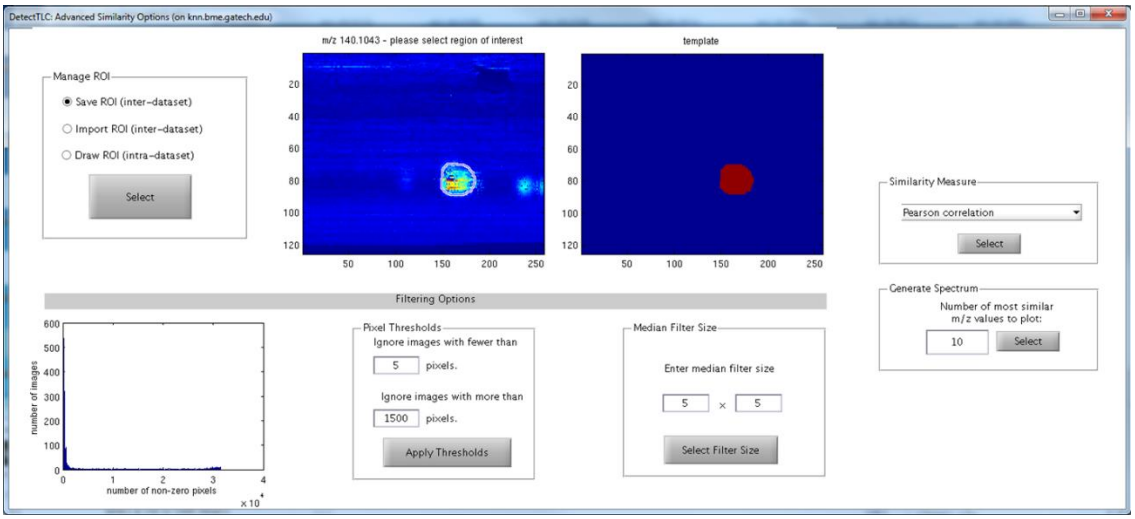

Figure 6.8. Advanced Similarity Options GUI in DetectTLC. The binary template for m/z 140.1, a side product of the APZ reaction, is shown as an example.

The Advanced Similarity Options window provides three methods for managing the region of interest (ROI) for similarity assessment. These are: (1) Create and save a new ROI template (may then be used with the same or another dataset, i.e., "inter-dataset"); (2) Import an existing ROI template (may be from the same or another dataset, i.e., "inter-dataset"); (3) Create and implement an ROI template on the current dataset (i.e., "intra-dataset"). These options are described further below.

The first option, “Save ROI (inter-dataset)” enables the user to draw a binary ROI template and save it for later use, with the same or another MSI dataset having the same spatial dimensions. If the checkbox of any m/*z* image was selected in the main GUI, that m/*z* image will be provided as the guide for drawing the binary template. If not, the average image across the loaded dataset will be provided. Once the template is drawn, the user may save it to a selected filename and directory. If a particular m/*z* image is used as the template basis, three variables are saved: the binary ROI, the m/*z* vector from current dataset, and the peak height of selected m/*z* in the current average spectrum. When the template is imported later, this data will be used to draw a spectrum of similar peaks. If the average m/*z* image is used as the template basis, only the binary ROI is saved.

In the second option, “Import ROI (inter-dataset)”, a previously drawn ROI can be loaded. In order to use this ROI for similarity assessment, it must have the same spatial dimensions as the currently loaded dataset. Some variations in spatial dimensions can be handled by DetectTLC. These are:

1. Template image is rotated 90 degrees with respect to current dataset. DetectTLC will rotate the template so that the dimensions match.
2. Template image has one extra row and/or column. DetectTLC will delete the first row and/or column from the dataset.
3. Template image is rotated 90 degrees and has an extra row and/or column.

Before any of these actions are taken, DetectTLC will notify the user that the spatial dimensions of the current dataset and selected template do not match. If the mismatch falls into any of these three categories, DetectTLC will prompt as to whether the template should

be automatically adjusted. If the mismatch does not fall into these three categories, DetectTLC will prompt the user to load a different template for use with the current dataset.

In the third option, “Draw template (intra-dataset)”, the user can draw a template which will immediately be used for similarity assessment on the currently loaded dataset, and which will not be saved. This differs from basic “Find Similar” option in that the user may select which similarity metric to use, and the spectrum of most similar peaks may be plotted.

After a template is available (either through the Import or Draw options), the median filter, pixel-count filter, “Choose similarity measure,” and “Plot spectrum of most similar” panels become visible. The median filter and pixel-count filter options are as described previously in this document. The user may select between two similarity measures: Pearson correlation or the hypergeometric similarity measure. Once the “Select” button is pressed, similarity assessment will proceed using the selected measure, and the m/*z* values in the current dataset will be sorted in the main GUI according to their similarity to the template. After similarity assessment has completed, the user may plot a spectrum of most similar m/*z* values by choosing the number to plot in the “Plot spectrum of most similar” panel. If the imported template was based on a particular m/*z* value, that m/*z* value (the precursor peak, in precursor-product analysis) will be indicated in red on the spectrum, and the similar peaks from the current dataset will be plotted in black. Otherwise, all peaks will be plotted in black.

6.4.7. Application Similarity Measure to Match Spots From Multi-Modal APZ Dataset

As an example to demonstrate the similarity capability within DetectTLC, a TLC plate with the separated APZ synthesis reaction mixture (Scheme 2) was imaged using

multi-modal MSI, alternating high- and low-energy scans. The fluorescence visualization of the separated APZ reaction mixture is shown in Figure 6.9a, and the structures of several predicted products are shown in Figure 6.9b. First, the low-energy dataset was processed with DetectTLC to identify key reaction products using a processing protocol of (1) Ostu's Method, (2) morphological opening, (3) pixel count filtering excluding [<5, >1500], (4) 5x5 median filtering, and (5) entropy image feature. The corresponding m/z images generated manually as well as the corresponding spots found by DetectTLC are shown in Figure 6.9c and Figure 6.9d, respectively. All three spots were detected in the top 24 results, which would be displayed on the first page of results in the DetectTLC GUI.

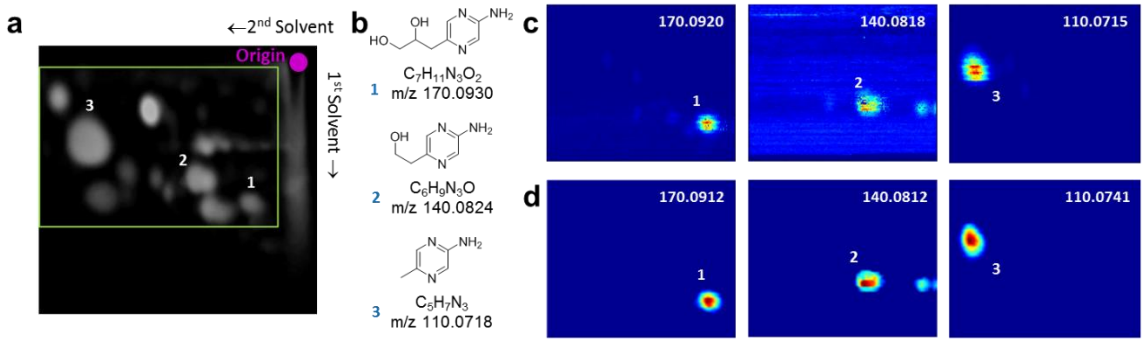

Figure 6.9. Fluorescence image of the separated APZ reaction mixture with the area imaged by DESI-MSI outlined in green (a). Known products of the APZ reaction, with the numbers indicating the spatial location of each product in the fluorescence and MS images (b). Selected ion images acquired by DESI-MSI of reaction products previously identified (b) and the corresponding spot-like images as they were generated by DetectTLC (d).

The spot with m/z 140.0812, 5(2-hydroxyethyl)-2-aminopyrazine, a predicted side-product of the APZ reaction was of particular interest, therefore Pearson correlation and the hypergeometric similarity measure were applied to pair it with fragment ions, to ultimately confirm its structure. The spot corresponding to the intact protonated ion was

first identified by DetectTLC from the low-energy dataset (Figure 6.9.d), and was selected to create a template of the spot's location (Figure 6.10a). The binary template (Figure 6.10b) was then applied to the high-energy dataset to find product ions that showed similar spot shape and location. The top eight m/*z* images matched using the Pearson correlation are shown in Figure 6.10c. The same top eight m/*z* images were obtained using the hypergeometic similarity measure, but ranked in a different order (data not shown). Upon further investigation, three of the product ions are logical fragments of the precursor ion (or the unfragmented precursor ion itself) based on expected chemical structure and predictable fragmentation patterns. Several ion images in the product results list showed multiple spots indicating multiple precursor ions with unique spatial separation having similar fragments, and therefore possibly similary structures. This is to be expected as the reaction products are all precursors to, or variations of, the desired product.

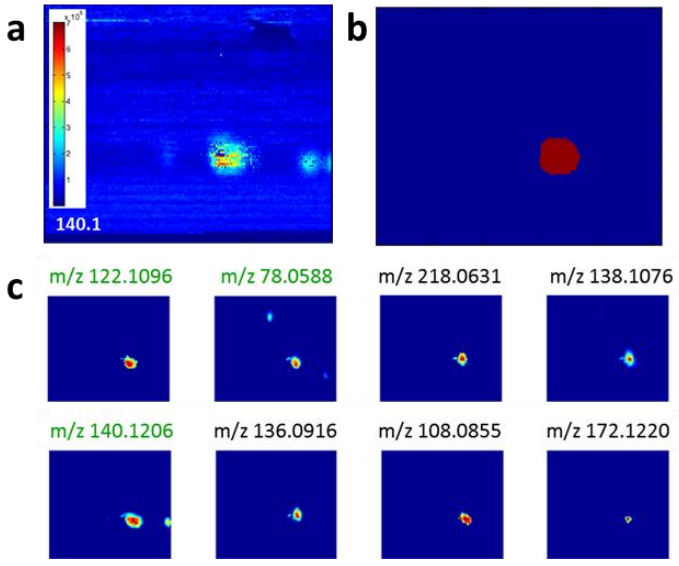

Figure 6.10. Selected ion image of precursor ion m/*z* 140.1 (a), and the template used to apply the similarity measure (b). Top eight ion images matched with the parent ion using Pearson correlation (c). Fragment ions detected in both LC-MS/MS and DetectTLC datasets are indicated with green labels.

To validate these matches generated by DetectTLC, liquid chromatography-tandem MS analysis was performed on APZ reaction mixture (Figure 6.11). The three predicted reaction products were successfully separated by UPLC (Figure 6.11a) and tandem mass spectrometry was performed on each (Figure 6.11b-d). When DetectTLC was applied to the parent ions with m/z 170.09 and 110.07, pairing of fragments ions with similar spatial distributions was not successful. However, upon further examination of the raw data, the fragments detected by UPLC-MS/MS were not detected by DESI-MSI. This is assumed to be because the collision energy was too low preventing full fragmenation of all species, therefore this failure is not considered to be a flaw with DetectTLC. Even still, the proof-of-principle application to the APZ mixture demonstrates the power of DetectTLC for improved chemical characterization of the TLC separation.

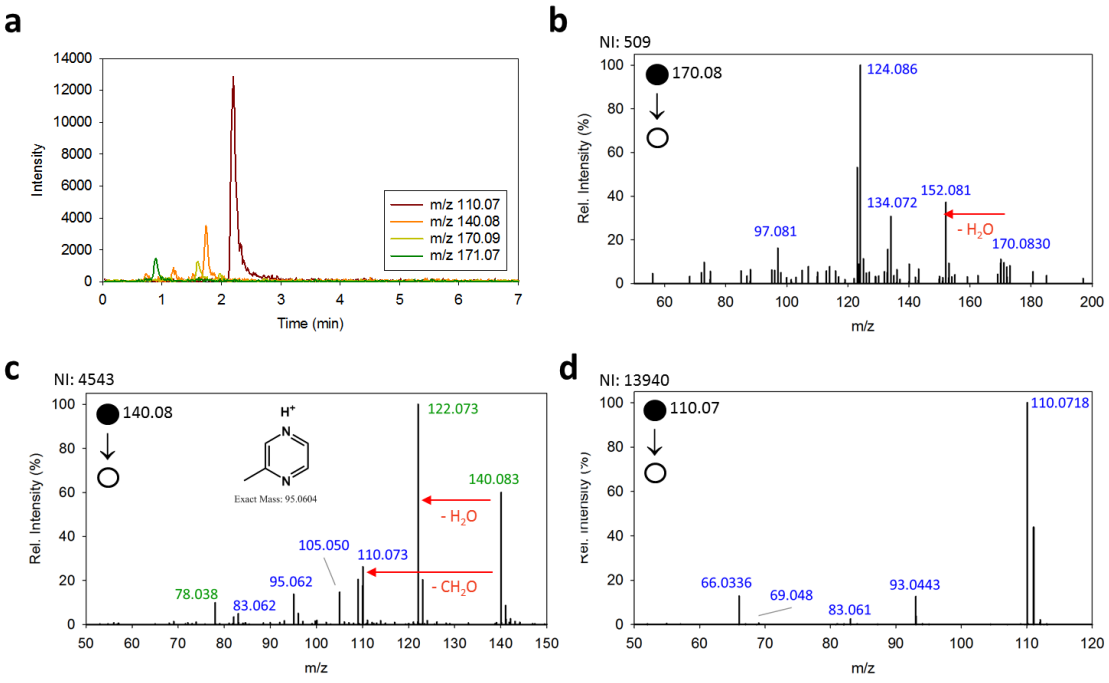

Figure 6.11. Tandem MS results from UPLC-MS/MS analysis of key APZ reaction products including extracted ion chromatograms (a) and selected tandem mass spectra (b-d). Fragment ions labeled in green were also paired as fragment ions in DetectTLC

6.5. Conclusion

In summary, through automated analysis of MSI data, DetectTLC is able to automatically pinpoint spots on 2D HPTLC plates corresponding to reaction products that were unexpected and undetectable via fluorescence, or co-eluted preventing selective optical visualization. This ensures that the user gains information describing all chemical species present on the plate regardless of their optical properties or chemical separation completeness. Structural identification of reaction products displaying spot-like regions can be accomplished when multi-modal imaging is performed, detecting intact and fragment ions in a single acquisition. This procedure facilitated the identification of a previously-unknown reaction side product and confirmed the chemical structure of other products. Although DetectTLC was designed for processing TLC-MSI datasets, it could also be more broadly applied to any MSI dataset where spot-like features are expected.

CHAPTER 7. CONCLUSIONS AND OUTLOOK

7.1. Abstract

This chapter presents a summary of the results and advances in instrumentation capabilities for mass spectrometry imaging (MSI) that have enabled increased chemical diversity, enhanced sensitivity and image contrast, imaging of bulky or irregularly-shaped surfaces, and multivariate tools to facilitate data interpretation. Additionally, potential future directions for continuation of this work are discussed.

7.2. Chemical Coverage Afforded by Different MSI Methods

7.2.1. Summary of Accomplishments

The effects of sample treatment and analyte extraction for DESI- and MALDI-MSI were investigated in order to maximize lipid coverage from brain tissues that have experienced TBI. Tissue washing with NH_4Form increased sensitivity for lipids in negative ion mode, and removed salts, shifting ion formation to the protonated species in positive ion mode. When performed carefully, the integrity of the tissue is retained, which is critical for imaging purposes. Washing as a means of desalting is well characterized in the literature,[155, 165, 179] but I propose that the washing step also alters the water content of the sample that ultimately affects analyte extraction prior to ionization. This study also found MALDI and DESI to be complementary techniques for the detection of lipids in brain tissues in terms of coverage and sensitivity. No one method stood out in terms of unique species detected, therefore in order to achieve better lipid coverage, both techniques would

be required. Alternatively, based on these results, the appropriate protocol could be chosen for targeted lipid analysis. Preliminary efforts to characterize changes in lipid species following TBI were inconclusive. MALDI and DESI showed similar fold changes for most species investigated, but the small sample number (1) limits the significance of these changes. Given the precious nature of the tissues used to study TBI, this in depth evaluation of imaging protocols is valuable to ensure quality data in future imaging experiments without wasting samples.

7.2.2. Proposed Future Directions

Additional experiments are necessary to fully understand the mechanism by which tissue washing enhances lipid sensitivity in MSI. To test the proposed hypothesis relating to surface wetting and enhanced analyte extraction, longer tissue drying times after washing could be used to study samples dried out to different extents. By allowing the tissue to dry for a longer period of time, additional moisture introduced to the sample during washing would be removed. Alternatively, the tissues could be allowed to dry under ambient conditions, in which both the washed and unwashed tissues would equilibrate to comparable moisture content based on relative humidity. Modeling of the mass transport between tissues wetted to different degrees may also shed light on the mechanism that leads to enhanced sensitivity.

Future experiments in the study of TBI will involve imaging of more samples for increasing statistical significance in the localized identification of TBI biomarkers. Using optimized DESI and MALDI protocols, tissues will be imaged and lipids of interest will then be confidently identified by tandem mass spectrometry imaging experiments in a targeted fashion. Although comparisons between injured and contralateral tissues may be

compared to study TBI, naïve (uninjured and no surgery) and sham (uninjured, but undergo similar surgery to injured samples) specimens are necessary to establish adequate controls. The information obtained by imaging localized changes in metabolites in the brain tissue may help guide additional metabolomics studies of TBI. A parallel study of metabolite changes in rat serum following TBI is currently underway to establish biomarkers using a bio-fluid that is more easily accessible than brain tissue. The combination of MSI and serum metabolomics promises to provide valuable information for the diagnosis and treatment of TBI.

7.3. Enhanced Image Contrast by Differential Mobility-DESI-MSI

7.3.1. Summary of Accomplishments

Targeted differential mobility filtering prior to MS analysis has previously shown significant capabilities for improving signal-to-noise ratios while preserving duty cycle for a number of bioanalytical applications. By coupling DESI with DMS, we demonstrated how these benefits translate to substantial improvements in ambient MSI image quality. In these experiments, DMS filtering facilitated significant signal to noise improvement, an order of magnitude increase, for imaging sea algae samples for a small (137 Da) chemical cue agent. Imaging of higher-mass lipid species in brain tissue sections further demonstrated the improved image quality and contrast with DMS filtering enabled. This was true when considering a single analyte but was further strengthened when considering multiple analytes of interest that may comprise a statistical component. The use of carrier gas dopants showed promise, but further characterization and implementation was halted by an electronics failure of the system. Overall, DMS, a high-duty-cycle ion mobility

filtering method, offers convenient coupling to DESI-MSI and provides higher quality chemical images by filtering off unwanted signals and chemical noise.

7.3.2. Proposed Future Directions

The use of carrier gas modifiers shows promise for greater lipid separation by DMS, but the current study was limited by inconsistent dopant delivery. With a repaired or functional DMS cell, full optimization of modifier introduction is recommended. To ensure complete volatilization and mixing of the modifier with the carrier gas, it is recommended that a larger mixing chamber be incorporated to the gas delivery line. The larger mixing chamber used to mix modifiers at concentrations of ~1-5% have proven to be effective in other laboratories (based on personal conversations with DMS researchers). A recent publication by Lintonen et al. found isopropanol to be the best dopant for separation of phospholipids during a lipidomics study, which supports the findings here.[218] Greater DMS separation of lipids would be valuable in the identification of isobaric lipid species, which present challenges for data interpretation from direct tissue imaging studies. Additionally, this system was not tested in negative ion mode, and DESI-DM-MSI could also assist in the distinction between different classes in that mode as well.

Once key lipids or metabolites have been identified from the untargeted TBI studies, DESI-DM-MSI could be applied to those samples for targeted imaging. Changes in lipid abundance following the CCI injury may be very subtle depending on the time allowed for recovery. Therefore, the enhanced sensitivity and selectivity afforded by DESI-DM-MSI offers a key advantage to detect minor changes in targeted lipid species as a function of recovery time in order to study how the disease progresses or to identify key biomarkers immediately following injury.

7.4. Imaging of Irregular Surfaces by Ambient MSI

7.4.1. Summary of Accomplishments

DESI-MSI was successfully used to image porous and bulky samples for the first time. This technique enabled the detection of products of the model prebiotic formamide reaction, indicating their distribution across a heterogeneous mineral surface. Control experiments confirmed that product distributions were not an artifact from the DESI analytical process or the selective adsorption of products onto the surface, verifying previous hypotheses, which indicated that mineral surfaces play a direct reactive or catalytic role in the formamide reaction. To our knowledge, this study was the first application of DESI to the analysis of minerals.

A new mass spectrometry surface analysis technique, RoPPI-MS, was described for the investigation of non-planar samples. The use of an ionization technique without enclosures such as DART enables easy and repeatable injections of the probed material into the plasma region. Unlike other ambient MSI techniques, RoPPI-MS does not require a planar sample allowing for surface imaging of samples in their native states. RoPPI-MS opens new avenues for examining in vivo tissues, organisms as they grow, classifying human skin lesions, probing 3D cell cultures, high-throughput baggage screening, monitoring produce safety, etc. We recognize that the resolution in the current system can still be improved, mainly arising from limitations of the robotic arms utilized. This is not a drawback of the concept per se, but of the specific implementation used in these proof-of-principle experiments.

7.4.2. Proposed Future Directions

Our lab is currently implementing a new RoPPI-MS system with a new robotic arm that is safe to operate in the presence of humans. This robotic arm, a Universal Robots (Odense S, Denmark) UR5 model offers 0.1 mm positioning repeatability and a more user-friendly interface. Several other improvements are also being made to the system for greater modularity and applicability. The generation of the 3D point cloud will be generated by "stitching together" snapshots of the sample from multiple angles, creating a more accurate point cloud at the boundary edges.

The probe used for surface sampling is being modified to accommodate different types of probes including a soldering iron for thermal desorption or a fiber optic for laser ablation. This modification is essential to be able to tailor the sampling probe for the type of sample and desired application; a solid acupuncture needle would not be efficient for extracting analytes from a hard or dry surface, therefore alternative sampling is necessary. Based on different surface sampling probes used, a new sample introduction system is also being designed to more efficiently collecting sample material. A line with moderate suction is being used to transport desorbed analytes into the ionization region of the DART source. Alternatively, this line may be introduced into to the ionization region of an extractive electrospray (EESI)[254-255] which may offer greater sensitivity for certain applications. Extensive characterization of the analytical figures of merit of the optimized system will be reported in the future.

7.5. Automatic Reaction Mixture Screening Based on Mass Spectrometric Images

7.5.1. Summary of Accomplishments

Through automated analysis of MSI data acquired for TLC separations, DetectTLC is able to automatically pinpoint spots on 2D HPTLC plates corresponding to reaction products that were unexpected and undetectable via fluorescence, or co-eluted preventing selective optical visualization. This ensures that the user gains information describing all chemical species present on the plate regardless of their optical properties or chemical separation completeness. Structural identification of reaction products displaying spot-like regions can be accomplished when multi-modal imaging is performed, detecting intact and fragment ions in a single acquisition. This procedure facilitated the identification of a previously-unknown reaction side product and confirmed the chemical structure of other products. Although DetectTLC was designed for processing TLC-MSI datasets, it could also be more broadly applied to any MSI dataset where spot-like features are expected.

APPENDIX A: COLLABORATOR CONTRIBUTIONS

A.1. Abstract

This appendix serves to credit collaborators who have contributed to the research presented in this thesis, especially for the work published with co-contributing authorship.

A.2. Brain Tissue Imaging of Traumatic Brain Injury Model Samples

R.B. Stryffeler prepared all tissues beginning with tissue sectioning, acquired all MSI and processed all MSI data. The rat samples used in this study were house and cared for in the laboratory of Dr. Michelle LaPlaca (Georgia Institute of Technology, Wallace H. Coulter School of Biomedical Engineering). The rats were handled by Dr. Brian Rooney who also induced the controlled cortical injury with the assistance of Connor Crowley. Scott Hogan (Georgia Institute of Technology) provided insightful discussions on traumatic brain injury to better understand chemical changes observed in acquired data. Dr. Martin Paine (Georgia Institute of Technology) provided suggestions related to MSI data acquisition.

A.3. Enhanced Image Contrast by Differential Mobility-DESI-MSI

Dr. Chaminda Gamage and R.B. Stryffeler worked side-by side to optimize DESI-DM-MSI performance for brain tissue imaging. All brain tissue images shown in this thesis were acquired by R.B. Stryffeler. Dr. Asiri Galhena acquired DESI-DM-MSI imaging results from algae tissues. R.B. Stryffeler was the primary author of published manuscript and performed all secondary data processing in response to reviewer comments.

A.4. Imaging Bulky Samples by Desorption Electrospray Ionization Mass Spectrometry

R.B. Stryffeler carried out all formamide reactions and DESI-MSI experiments. Dr. H. James Cleaves provided granite samples and guidance for experimental design. Dr. Jeffrey M. Davis (National Institute of Standards and Technology) characterized granite mineralogy. Dennis Sokolov provided training and suggestions for Raman characterization; surface Raman experiments were conducted by R.B Stryffeler. Dr. Thomas Orlando (Georgia Institute of Technology) and Dr. Jeffrey Bada (University of California San Diego) provided direction with respect to prebiotic chemistry considerations.

A.5. Novel Three-Dimensional Surface Imaging Using Robotic Plasma Probe Ionization Mass Spectrometry

R.B. Stryffeler and Ezequiel M. Morzan (Universidad de Buenos Aires, Argentina) worked together to design Robotic Plasma Probe Ionization (RoPPI)-MSI system and worked side-by-side performing preliminary experiments with the Lynxmotion robotic arm. R.B. Stryffeler performed all experiments using the Kuka robotic arm, processed all data and wrote the publication manuscript. The Kuka robotic arm was programmed by Dr. Jacob Huckaby (Georgia Institute of Technology, College of Computing) for the motion sequence requested by R.B. Stryffeler and E.M. Morzan.

A.6. Automatic Reaction Mixture Screening Based on Mass Spectrometric Images

R.B. Stryffeler performed all DESI-MSI imaging experiments and provided direction for the design of DetectTLC with regard to necessary functions. Chanchala D. Kaddi selected the appropriate algorithms to employ and performed all coding of DetectTLC. R.B. Stryffeler and C.D. Kaddi worked together to troubleshoot DetectTLC and develop means by which to characterize its performance. Dr. Martin R.L. Paine provided insightful discussions and suggestions related to the capabilities and application of DetectTLC.

REFERENCES

1. Castaing, R.; Slodzian, G., Microanalyse Par Emission Ionique Secondaire. *Journal De Microscopie* **1962,** *1*, 395-410.

2. Liebl, H., Ion Microprobe Mass Analyzer. *J. Appl. Phys.* **1967,** *38* (13), 5277-5283.

3. Levi-Setti, R.; Wang, Y., L.; Crow, G., High Spatial Resolution SIMS with the UC-HRL Scanning Ion Microprobe. *J. Phys. Colloques* **1984,** *45* (C9), 197-205.

4. Chait, B. T.; Standing, K. G., A time-of-flight mass spectrometer for measurement of secondary ion mass spectra. *Int. J. Mass Spectrom.* **1981,** *40* (2), 185-193.

5. Pacholski, M. L.; Winograd, N., Imaging with Mass Spectrometry. *Chem. Rev.* **1999,** *99* (10), 2977-3006.

6. Sjövall, P.; Lausmaa, J.; Johansson, B., Mass Spectrometric Imaging of Lipids in Brain Tissue. *Anal. Chem.* **2004,** *76* (15), 4271-4278.

7. Chughtai, K.; Heeren, R. M. A., Mass Spectrometric Imaging for Biomedical Tissue Analysis. *Chem. Rev.* **2010,** *110* (5), 3237-3277.

8. Benninghoven, A., Surface investigation of solids by the statical method of secondary ion mass spectroscopy (SIMS). *Surf. Sci.* **1973,** *35* (0), 427-457.

9. Grade, H.; Winograd, N.; Cooks, R. G., Cationization of organic molecules in secondary ion mass spectrometry. *J. Am. Chem. Soc.* **1977,** *99* (23), 7725-7726.

10. Benninghoven, A.; Jaspers, D.; Sichtermann, W., Secondary-ion emission of amino acids. *Applied physics* **1976,** *11* (1), 35-39.

11. Benninghoven, A.; Sichtermann, W. K., Detection, identification, and structural investigation of biologically important compounds by secondary ion mass spectrometry. *Anal. Chem.* **1978,** *50* (8), 1180-1184.

12. Passarelli, M. K.; Winograd, N., Lipid imaging with time-of-flight secondary ion mass spectrometry (ToF-SIMS). *Biochimica et Biophysica Acta (BBA) - Molecular and Cell Biology of Lipids* **2011,** *1811* (11), 976-990.

13. Childs, K. D.; Narum, D.; LaVanier, L. A.; Lindley, P. M.; Schueler, B. W.; Mulholland, G.; Diebold, A. C., Comparison of submicron particle analysis by Auger electron spectroscopy, time-of-flight secondary ion mass spectrometry, and secondary electron microscopy with energy dispersive x-ray spectroscopy. *Journal of Vacuum Science & Technology A* **1996,** *14* (4), 2392-2404.

14. Gillen, G.; Bennett, J.; Tarlov, M. J.; Burgess, D. R. F., Molecular Imaging Secondary Ion Mass Spectrometry for the Characterization of Patterned Self-Assembled Monolayers on Silver and Gold. *Anal. Chem.* **1994,** *66* (13), 2170-2174.

15. Chabala, J. M.; Soni, K. K.; Li, J.; Gavrilov, K. L.; Levi-Setti, R., High-resolution chemical imaging with scanning ion probe SIMS. *Int. J. Mass Spectrom. Ion Processes* **1995,** *143* (0), 191-212.

16. Thompson, A. M.; Soni, K. K.; Chan, H. M.; Harmer, M. P.; Williams, D. B.; Chabala, J. M.; Levi-Setti, R., Dopant Distributions in Rare-Earth-Doped Alumina. *J. Am. Ceram. Soc.* **1997,** *80* (2), 373-376.

17. Altelaar, A. F. M.; Klinkert, I.; Jalink, K.; de Lange, R. P. J.; Adan, R. A. H.; Heeren, R. M. A.; Piersma, S. R., Gold-Enhanced Biomolecular Surface Imaging of Cells and Tissue by SIMS and MALDI Mass Spectrometry. *Anal. Chem.* **2006,** *78* (3), 734-742.

18. Pacholski, M. L.; Cannon, D. M.; Ewing, A. G.; Winograd, N., Imaging of Exposed Headgroups and Tailgroups of Phospholipid Membranes by Mass Spectrometry. *J. Am. Chem. Soc.* **1999,** *121* (19), 4716-4717.

19. Fletcher, J.; Vickerman, J., A new SIMS paradigm for 2D and 3D molecular imaging of bio-systems. *Anal. Bioanal. Chem.* **2010,** *396* (1), 85-104.

20. Hillenkamp, F.; Unsöld, E.; Kaufmann, R.; Nitsche, R., A high-sensitivity laser microprobe mass analyzer. *Applied physics* **1975,** *8* (4), 341-348.

21. Karas, M.; Bachmann, D.; Hillenkamp, F., Influence of the wavelength in high-irradiance ultraviolet laser desorption mass spectrometry of organic molecules. *Anal. Chem.* **1985,** *57* (14), 2935-2939.

22. Tanaka, K.; Waki, H.; Ido, Y.; Akita, S.; Yoshida, Y.; Yoshida, T.; Matsuo, T., Protein and polymer analyses up to m/z 100 000 by laser ionization time-of-flight mass spectrometry. *Rapid Commun. Mass Spectrom.* **1988,** *2* (8), 151-153.

23. Caprioli, R. M.; Farmer, T. B.; Gile, J., Molecular Imaging of Biological Samples: Localization of Peptides and Proteins Using MALDI-TOF MS. *Anal. Chem.* **1997,** *69* (23), 4751-4760.

24. Schwartz, S. A.; Reyzer, M. L.; Caprioli, R. M., Direct tissue analysis using matrix-assisted laser desorption/ionization mass spectrometry: practical aspects of sample preparation. *J. Mass Spectrom.* **2003,** *38* (7), 699-708.

25. Zhigilei, L. V., Dynamics of the plume formation and parameters of the ejected clusters in short-pulse laser ablation. *Appl. Phys. A* **2003,** *76* (3), 339-350.

26. Dreisewerd, K., The Desorption Process in MALDI. *Chem. Rev.* **2003,** *103* (2), 395-426.

27. Westmacott, G.; Ens, W.; Hillenkamp, F.; Dreisewerd, K.; Schürenberg, M., The influence of laser fluence on ion yield in matrix-assisted laser desorption ionization mass spectrometry. *Int. J. Mass spectrom.* **2002,** *221* (1), 67-81.

28. Zenobi, R.; Knochenmuss, R., Ion formation in MALDI mass spectrometry. *Mass Spectrom. Rev.* **1998,** *17* (5), 337-366.

29. Knochenmuss, R., Ion formation mechanisms in UV-MALDI. *Analyst* **2006,** *131* (9), 966-986.

30. Lemaire, R.; Tabet, J. C.; Ducoroy, P.; Hendra, J. B.; Salzet, M.; Fournier, I., Solid Ionic Matrixes for Direct Tissue Analysis and MALDI Imaging. *Anal. Chem.* **2006,** *78* (3), 809-819.

31. Karas, M.; Glückmann, M.; Schäfer, J., Ionization in matrix-assisted laser desorption/ionization: singly charged molecular ions are the lucky survivors. *J. Mass Spectrom.* **2000,** *35* (1), 1-12.

32. Ehring, H.; Karas, M.; Hillenkamp, F., Role of photoionization and photochemistry in ionization processes of organic molecules and relevance for matrix-assisted laser desorption lonization mass spectrometry. *Org. Mass Spectrom.* **1992,** *27* (4), 472-480.

33. Chiarelli, M. P.; Sharkey, A. G.; Hercules, D. M., Excited-state proton transfer in laser mass spectrometry. *Anal. Chem.* **1993,** *65* (3), 307-311.

34. Knochenmuss, R., A quantitative model of ultraviolet matrix-assisted laser desorption/ionization. *J. Mass Spectrom.* **2002,** *37* (8), 867-877.

35. Knochenmuss, R.; Zenobi, R., MALDI Ionization: The Role of In-Plume Processes. *Chem. Rev.* **2003,** *103* (2), 441-452.

36. Woods, A. S.; Colsch, B.; Jackson, S. N.; Post, J.; Baldwin, K.; Roux, A.; Hoffer, B.; Cox, B. M.; Hoffer, M.; Rubovitch, V.; Pick, C. G.; Schultz, J. A.; Balaban, C., Gangliosides and Ceramides Change in a Mouse Model of Blast Induced Traumatic Brain Injury. *ACS Chem. Neurosci.* **2013,** *4* (4), 594-600.

37. Luxembourg, S. L.; McDonnell, L. A.; Duursma, M. C.; Guo, X.; Heeren, R. M. A., Effect of Local Matrix Crystal Variations in Matrix-Assisted Ionization Techniques for Mass Spectrometry. *Anal. Chem.* **2003,** *75* (10), 2333-2341.

38. McDonnell, L. A.; Heeren, R. M. A., Imaging mass spectrometry. *Mass Spectrom. Rev.* **2007,** *26* (4), 606-643.

39. Chen, Y.; Allegood, J.; Liu, Y.; Wang, E.; Cachon-Gonzalez, B.; Cox, T. M.; Merrill, A. H.; Sullards, M. C., Imaging MALDI Mass Spectrometry Using an Oscillating Capillary Nebulizer Matrix Coating System and Its Application to Analysis of Lipids in Brain from a Mouse Model of Tay−Sachs/Sandhoff Disease. *Anal. Chem.* **2008,** *80* (8), 2780-2788.

40. Hankin, J. A.; Barkley, R. M.; Murphy, R. C., Sublimation as a Method of Matrix Application for Mass Spectrometric Imaging. *J. Am. Soc. Mass. Spectrom.* **2007,** *18* (9), 1646-1652.

41. Bouschen, W.; Schulz, O.; Eikel, D.; Spengler, B., Matrix vapor deposition/recrystallization and dedicated spray preparation for high-resolution scanning microprobe matrix-assisted laser desorption/ionization imaging mass spectrometry (SMALDI-MS) of tissue and single cells. *Rapid Commun. Mass Spectrom.* **2010,** *24* (3), 355-364.

42. Heeren, R. M. A.; Smith, D. F.; Stauber, J.; Kükrer-Kaletas, B.; MacAleese, L., Imaging Mass Spectrometry: Hype or Hope? *J. Am. Soc. Mass. Spectrom.* **2009,** *20* (6), 1006-1014.

43. Chaurand, P.; Schriver, K. E.; Caprioli, R. M., Instrument design and characterization for high resolution MALDI-MS imaging of tissue sections. *J. Mass Spectrom.* **2007,** *42* (4), 476-489.

44. Spengler, B.; Hubert, M., Scanning microprobe matrix-assisted laser desorption ionization (SMALDI) mass spectrometry: instrumentation for sub-micrometer resolved LDI and MALDI surface analysis. *J. Am. Soc. Mass. Spectrom.* **2002,** *13* (6), 735-748.

45. Römpp, A.; Spengler, B., Mass spectrometry imaging with high resolution in mass and space. *Histochem Cell Biol* **2013,** *139* (6), 759-783.

46. Jurchen, J. C.; Rubakhin, S. S.; Sweedler, J. V., MALDI-MS imaging of features smaller than the size of the laser beam. *J. Am. Soc. Mass. Spectrom.* **2005,** *16* (10), 1654-1659.

47. Snel, M. F.; Fuller, M., High-Spatial Resolution Matrix-Assisted Laser Desorption Ionization Imaging Analysis of Glucosylceramide in Spleen Sections from a Mouse Model of Gaucher Disease. *Anal. Chem.* **2010,** *82* (9), 3664-3670.

48. Altelaar, A. F. M.; Luxemourg, S. L.; McDonnell, L. A.; Piersma, S. R.; Heeren, R. M. A., Imaging Mass Spectrometry at Cellular Length Scales. *Nature Protocols* **2007,** *2* (3), 1185-1196.

49. Luxembourg, S. L.; Mize, T. H.; McDonnell, L. A.; Heeren, R. M. A., High-Spatial Resolution Mass Spectrometric Imaging of Peptide and Protein Distributions on a Surface. *Anal. Chem.* **2004,** *76* (18), 5339-5344.

50. Dole, M.; Mack, L. L.; Hines, R. L.; Mobley, R. C.; Ferguson, L. D.; Alice, M. B., Molecular Beams of Macroions. *The Journal of Chemical Physics* **1968,** *49* (5), 2240-2249.

51. Horning, E. C.; Carroll, D. I.; Dzidic, I.; Haegele, K. D.; Horning, M. G.; Stillwell, R. N., Atmospheric Pressure Ionization (API) Mass Spectrometry. Solvent-Mediated Ionization of Samples Introduced in Solution and in a Liquid Chromatograph Effluent Stream. *J. Chromatogr. Sci.* **1974,** *12* (11), 725-729.

52. Whitehouse, C. M.; Dreyer, R. N.; Yamashita, M.; Fenn, J. B., Electrospray interface for liquid chromatographs and mass spectrometers. *Anal. Chem.* **1985,** *57* (3), 675-679.

53. Fenn, J.; Mann, M.; Meng, C.; Wong, S.; Whitehouse, C., Electrospray ionization for mass spectrometry of large biomolecules. *Science* **1989,** *246* (4926), 64-71.

54. Nefliu, M.; Smith, J. N.; Venter, A.; Cooks, R. G., Internal Energy Distributions in Desorption Electrospray Ionization (DESI). *J. Am. Soc. Mass. Spectrom.* **2008,** *19* (3), 420-427.

55. Luo, G.; Marginean, I.; Vertes, A., Internal Energy of Ions Generated by Matrix-Assisted Laser Desorption/Ionization. *Anal. Chem.* **2002,** *74* (24), 6185-6190.

56. Kebarle, P.; Verkerk, U. H., Electrospray: From ions in solution to ions in the gas phase, what we know now. *Mass Spectrom. Rev.* **2009,** *28* (6), 898-917.

57. Yamashita, M.; Fenn, J. B., Electrospray ion source. Another variation on the free-jet theme. *J. Phys. Chem.* **1984,** *88* (20), 4451-4459.

58. Konermann, L.; Ahadi, E.; Rodriguez, A. D.; Vahidi, S., Unraveling the Mechanism of Electrospray Ionization. *Anal. Chem.* **2012,** *85* (1), 2-9.

59. Iribarne, J. V.; Thomson, B. A., On the evaporation of small ions from charged droplets. *J. Chem. Phys.* **1976,** *64* (6), 2287-2294.

60. Thomson, B. A.; Iribarne, J. V., Field induced ion evaporation from liquid surfaces at atmospheric pressure. *J. Chem. Phys.* **1979,** *71* (11), 4451-4463.

61. Bruins, A. P.; Covey, T. R.; Henion, J. D., Ion spray interface for combined liquid chromatography/atmospheric pressure ionization mass spectrometry. *Anal. Chem.* **1987,** *59* (22), 2642-2646.

62. Wilm, M. S.; Mann, M., Electrospray and Taylor-Cone theory, Dole's beam of macromolecules at last? *Int. J. Mass Spectrom. Ion Processes* **1994,** *136* (2–3), 167-180.

63. Takáts, Z.; Wiseman, J. M.; Gologan, B.; Cooks, R. G., Mass Spectrometry Sampling Under Ambient Conditions with Desorption Electrospray Ionization. *Science* **2004,** *306* (5695), 471-473.

64. Cody, R. B.; Laramée, J. A.; Durst, H. D., Versatile New Ion Source for the Analysis of Materials in Open Air under Ambient Conditions. *Anal. Chem.* **2005,** *77* (8), 2297-2302.

65. Harris, G. A.; Galhena, A. S.; Fernández, F. M., Ambient Sampling/Ionization Mass Spectrometry: Applications and Current Trends. *Anal. Chem.* **2011,** *83* (12), 4508-4538.

66. Van Berkel, G. J.; Pasilis, S. P.; Ovchinnikova, O., Established and emerging atmospheric pressure surface sampling/ionization techniques for mass spectrometry. *J. Mass Spectrom.* **2008,** *43* (9), 1161-1180.

67. Monge, M. E.; Harris, G. A.; Dwivedi, P.; Fernández, F. M., Mass Spectrometry: Recent Advances in Direct Open Air Surface Sampling/Ionization. *Chem. Rev.* **2013,** *113* (4), 2269-2308.

68. Haddad, R.; Sparrapan, R.; Eberlin, M. N., Desorption sonic spray ionization for (high) voltage-free ambient mass spectrometry. *Rapid Commun. Mass Spectrom.* **2006,** *20* (19), 2901-2905.

69. Van Berkel, G. J.; Sanchez, A. D.; Quirke, J. M. E., Thin-Layer Chromatography and Electrospray Mass Spectrometry Coupled Using a Surface Sampling Probe. *Anal. Chem.* **2002,** *74* (24), 6216-6223.

70. Andrade, F. J.; Shelley, J. T.; Wetzel, W. C.; Webb, M. R.; Gamez, G.; Ray, S. J.; Hieftje, G. M., Atmospheric Pressure Chemical Ionization Source. 1. Ionization of Compounds in the Gas Phase. *Anal. Chem.* **2008,** *80* (8), 2646-2653.

71. Andrade, F. J.; Shelley, J. T.; Wetzel, W. C.; Webb, M. R.; Gamez, G.; Ray, S. J.; Hieftje, G. M., Atmospheric Pressure Chemical Ionization Source. 2. Desorption−Ionization for the Direct Analysis of Solid Compounds. *Anal. Chem.* **2008,** *80* (8), 2654-2663.

72. Foest, R.; Schmidt, M.; Becker, K., Microplasmas, an emerging field of low-temperature plasma science and technology. *Int. J. Mass spectrom.* **2006,** *248* (3), 87-102.

73. Nemes, P.; Vertes, A., Laser Ablation Electrospray Ionization for Atmospheric Pressure, in Vivo, and Imaging Mass Spectrometry. *Anal. Chem.* **2007,** *79* (21), 8098-8106.

74. Shelley, J. T.; Ray, S. J.; Hieftje, G. M., Laser Ablation Coupled to a Flowing Atmospheric Pressure Afterglow for Ambient Mass Spectral Imaging. *Anal. Chem.* **2008,** *80* (21), 8308-8313.

75. Galhena, A. S.; Harris, G. A.; Nyadong, L.; Murray, K. K.; Fernández, F. M., Small Molecule Ambient Mass Spectrometry Imaging by Infrared Laser Ablation Metastable-Induced Chemical Ionization. *Anal. Chem.* **2010,** *82* (6), 2178-2181.

76. Cotte-Rodríguez, I.; Takáts, Z.; Talaty, N.; Chen, H.; Cooks, R. G., Desorption Electrospray Ionization of Explosives on Surfaces: Sensitivity and Selectivity Enhancement by Reactive Desorption Electrospray Ionization. *Anal. Chem.* **2005,** *77* (21), 6755-6764.

77. Ifa, D. R.; Manicke, N. E.; Dill, A. L.; Cooks, R. G., Latent Fingerprint Chemical Imaging by Mass Spectrometry. *Science* **2008,** *321* (5890), 805.

78. Nyadong, L.; Green, M. D.; De Jesus, V. R.; Newton, P. N.; Fernández, F. M., Reactive Desorption Electrospray Ionization Linear Ion Trap Mass Spectrometry of Latest-Generation Counterfeit Antimalarials via Noncovalent Complex Formation. *Anal. Chem.* **2007,** *79* (5), 2150-2157.

79. Fernández, F. M.; Cody, R. B.; Green, M. D.; Hampton, C. Y.; McGready, R.; Sengaloundeth, S.; White, N. J.; Newton, P. N., Characterization of Solid Counterfeit Drug Samples by Desorption Electrospray Ionization and Direct-analysis-in-real-time Coupled to Time-of-flight Mass Spectrometry. *ChemMedChem* **2006,** *1* (7), 702-705.

80. Wiseman, J. M.; Ifa, D. R.; Song, Q.; Cooks, R. G., Tissue Imaging at Atmospheric Pressure Using Desorption Electrospray Ionization (DESI) Mass Spectrometry. *Angew. Chem. Int. Ed.* **2006,** *45* (43), 7188-7192.

81. Eberlin, L. S.; Ifa, D. R.; Wu, C.; Cooks, R. G., Three-Dimensional Vizualization of Mouse Brain by Lipid Analysis Using Ambient Ionization Mass Spectrometry. *Angew. Chem. Int. Ed.* **2010,** *49* (5), 873-876.

82. Dill, A.; Eberlin, L.; Costa, A.; Ifa, D.; Cooks, R., Data quality in tissue analysis using desorption electrospray ionization. *Anal. Bioanal. Chem.* **2011,** *401* (6), 1949-1961.

83. Eberlin, L. S.; Ferreira, C. R.; Dill, A. L.; Ifa, D. R.; Cheng, L.; Cooks, R. G., Nondestructive, Histologically Compatible Tissue Imaging by Desorption Electrospray Ionization Mass Spectrometry. *ChemBioChem* **2011,** *12* (14), 2129-2132.

84. Eberlin, L. S.; Liu, X.; Ferreira, C. R.; Santagata, S.; Agar, N. Y. R.; Cooks, R. G., Desorption Electrospray Ionization then MALDI Mass Spectrometry Imaging of Lipid and Protein Distributions in Single Tissue Sections. *Anal. Chem.* **2011,** *83* (22), 8366-8371.

85. Eberlin, L. S.; Ferreira, C. R.; Dill, A. L.; Ifa, D. R.; Cooks, R. G., Desorption electrospray ionization mass spectrometry for lipid characterization and biological tissue imaging. *Biochim. Biophys. Acta* **2011,** *1811* (11), 946-960.

86. Eberlin, L. S.; Norton, I.; Dill, A. L.; Golby, A. J.; Ligon, K. L.; Santagata, S.; Cooks, R. G.; Agar, N. Y. R., Classifying Human Brain Tumors by Lipid Imaging with Mass Spectrometry. *Cancer Res.* **2012,** *72* (3), 645-654.

87. Eberlin, L. S.; Norton, I.; Orringer, D.; Dunn, I. F.; Liu, X.; Ide, J. L.; Jarmusch, A. K.; Ligon, K. L.; Jolesz, F. A.; Golby, A. J.; Santagata, S.; Agar, N. Y. R.; Cooks, R. G., Ambient mass spectrometry for the intraoperative molecular diagnosis of human brain tumors. *Proc. Natl. Acad. Sci.* **2013,** *110* (5), 1611-1616.

88. Ifa, D. R.; Wiseman, J. M.; Song, Q.; Cooks, R. G., Development of capabilities for imaging mass spectrometry under ambient conditions with desorption electrospray ionization (DESI). *Int. J. Mass spectrom.* **2007,** *259* (1–3), 8-15.

89. Van Berkel, G. J.; Kertesz, V., Automated Sampling and Imaging of Analytes Separated on Thin-Layer Chromatography Plates Using Desorption Electrospray Ionization Mass Spectrometry. *Anal. Chem.* **2006,** *78* (14), 4938-4944.

90. Takáts, Z.; Wiseman, J. M.; Cooks, R. G., Ambient mass spectrometry using desorption electrospray ionization (DESI): instrumentation, mechanisms and applications in forensics, chemistry, and biology. *J. Mass Spectrom.* **2005,** *40* (10), 1261-1275.

91. Venter, A.; Sojka, P. E.; Cooks, R. G., Droplet Dynamics and Ionization Mechanisms in Desorption Electrospray Ionization Mass Spectrometry. *Anal. Chem.* **2006,** *78* (24), 8549-8555.

92. Bereman, M. S.; Muddiman, D. C., Detection of Attomole Amounts of Analyte by Desorption Electrospray Ionization Mass Spectrometry (DESI-MS) Determined Using Fluorescence Spectroscopy. *J. Am. Soc. Mass. Spectrom.* **2007,** *18* (6), 1093-1096.

93. Costa, A. B.; Cooks, R. G., Simulation of atmospheric transport and droplet-thin film collisions in desorption electrospray ionization. *Chem. Commun.* **2007,** (38), 3915-3917.

94. Costa, A. B.; Graham Cooks, R., Simulated splashes: Elucidating the mechanism of desorption electrospray ionization mass spectrometry. *Chem. Phys. Lett.* **2008,** *464* (1–3), 1-8.

95. Green, F. M.; Stokes, P.; Hopley, C.; Seah, M. P.; Gilmore, I. S.; O'Connor, G., Developing Repeatable Measurements for Reliable Analysis of Molecules at Surfaces Using Desorption Electrospray Ionization. *Anal. Chem.* **2009,** *81* (6), 2286-2293.

96. Gurdak, E.; Green, F. M.; Rakowska, P. D.; Seah, M. P.; Salter, T. L.; Gilmore, I. S., VAMAS Interlaboratory Study for Desorption Electrospray Ionization Mass Spectrometry (DESI MS) Intensity Repeatability and Constancy. *Anal. Chem.* **2014,** *86* (19), 9603-9611.

97. Green, F. M.; Salter, T. L.; Gilmore, I. S.; Stokes, P.; O'Connor, G., The effect of electrospray solvent composition on desorption electrospray ionisation (DESI) efficiency and spatial resolution. *Analyst* **2010,** *135* (4), 731-737.

98. Badu-Tawiah, A.; Bland, C.; Campbell, D. I.; Cooks, R. G., Non-Aqueous Spray Solvents and Solubility Effects in Desorption Electrospray Ionization. *J. Am. Soc. Mass. Spectrom.* **2010,** *21* (4), 572-579.

99. Badu-Tawiah, A.; Cooks, R. G., Enhanced Ion Signals in Desorption Electrospray Ionization Using Surfactant Spray Solutions. *J. Am. Soc. Mass. Spectrom.* **2010,** *21* (8), 1423-1431.

100. Nyadong, L.; Hohenstein, E.; Galhena, A.; Lane, A.; Kubanek, J.; Sherrill, C.; Fernández, F., Reactive desorption electrospray ionization mass spectrometry (DESI-MS) of natural products of a marine alga. *Anal. Bioanal. Chem.* **2009,** *394* (1), 245-254.

101. Chen, H.; Cotte-Rodriguez, I.; Cooks, R. G., cis-Diol functional group recognition by reactive desorption electrospray ionization (DESI). *Chem. Commun.* **2006,** (6), 597-599.

102. Cotte-Rodriguez, I.; Chen, H.; Cooks, R. G., Rapid trace detection of triacetone triperoxide (TATP) by complexation reactions during desorption electrospray ionization. *Chem. Commun.* **2006,** (9), 953-955.

103. Wu, C.; Ifa, D. R.; Manicke, N. E.; Cooks, R. G., Rapid, Direct Analysis of Cholesterol by Charge Labeling in Reactive Desorption Electrospray Ionization. *Anal. Chem.* **2009,** *81* (18), 7618-7624.

104. Nefliu, M.; Cooks, R. G.; Moore, C., Enhanced desorption ionization using oxidizing electrosprays. *J. Am. Soc. Mass. Spectrom.* **2006,** *17* (8), 1091-1095.

105. Pasilis, S. P.; Kertesz, V.; Van Berkel, G. J., Surface Scanning Analysis of Planar Arrays of Analytes with Desorption Electrospray Ionization-Mass Spectrometry. *Anal. Chem.* **2007,** *79* (15), 5956-5962.

106. Douglass, K.; Jain, S.; Brandt, W.; Venter, A., Deconstructing Desorption Electrospray Ionization: Independent Optimization of Desorption and Ionization by Spray Desorption Collection. *J. Am. Soc. Mass. Spectrom.* **2012,** *23* (11), 1896-1902.

107. Kertesz, V.; Van Berkel, G. J., Scanning and Surface Alignment Considerations in Chemical Imaging with Desorption Electrospray Mass Spectrometry. *Anal. Chem.* **2008,** *80* (4), 1027-1032.

108. Campbell, D.; Ferreira, C.; Eberlin, L.; Cooks, R., Improved spatial resolution in the imaging of biological tissue using desorption electrospray ionization. *Anal. Bioanal. Chem.* **2012,** *404* (2), 389-398.

109. Kertesz, V.; Van Berkel, G. J., Improved imaging resolution in desorption electrospray ionization mass spectrometry. *Rapid Commun. Mass Spectrom.* **2008,** *22* (17), 2639-2644.

110. Haddad, R.; Milagre, H. M. S.; Catharino, R. R.; Eberlin, M. N., Easy Ambient Sonic-Spray Ionization Mass Spectrometry Combined with Thin-Layer Chromatography. *Anal. Chem.* **2008,** *80* (8), 2744-2750.

111. Haddad, R.; Sparrapan, R.; Kotiaho, T.; Eberlin, M. N., Easy Ambient Sonic-Spray Ionization-Membrane Interface Mass Spectrometry for Direct Analysis of Solution Constituents. *Anal. Chem.* **2008,** *80* (3), 898-903.

112. Roach, P. J.; Laskin, J.; Laskin, A., Nanospray desorption electrospray ionization: an ambient method for liquid-extraction surface sampling in mass spectrometry. *Analyst* **2010,** *135* (9), 2233-2236.

113. Laskin, J.; Heath, B. S.; Roach, P. J.; Cazares, L.; Semmes, O. J., Tissue Imaging Using Nanospray Desorption Electrospray Ionization Mass Spectrometry. *Anal. Chem.* **2011,** *84* (1), 141-148.

114. Lanekoff, I.; Thomas, M.; Carson, J. P.; Smith, J. N.; Timchalk, C.; Laskin, J., Imaging Nicotine in Rat Brain Tissue by Use of Nanospray Desorption Electrospray Ionization Mass Spectrometry. *Anal. Chem.* **2012,** *85* (2), 882-889.

115. Lanekoff, I.; Stevens, S. L.; Stenzel-Poore, M. P.; Laskin, J., Matrix effects in biological mass spectrometry imaging: identification and compensation. *Analyst* **2014,** *139* (14), 3528-3532.

116. Kertesz, V.; Ford, M. J.; Van Berkel, G. J., Automation of a Surface Sampling Probe/Electrospray Mass Spectrometry System. *Anal. Chem.* **2005,** *77* (22), 7183-7189.

117. Van Berkel, G. J.; Kertesz, V.; Koeplinger, K. A.; Vavrek, M.; Kong, A.-N. T., Liquid microjunction surface sampling probe electrospray mass spectrometry for detection of drugs and metabolites in thin tissue sections. *J. Mass Spectrom.* **2008,** *43* (4), 500-508.

118. Günther, D.; Hattendorf, B., Solid sample analysis using laser ablation inductively coupled plasma mass spectrometry. *TrAC, Trends Anal. Chem.* **2005,** *24* (3), 255-265.

119. Kolaitis, L.; Lubman, D. M., Atmospheric pressure ionization mass spectrometry with laser-produced ions. *Anal. Chem.* **1986,** *58* (9), 1993-2001.

120. Coon, J. J.; McHale, K. J.; Harrison, W. W., Atmospheric pressure laser desorption/chemical ionization mass spectrometry: a new ionization method based on existing themes. *Rapid Commun. Mass Spectrom.* **2002,** *16* (7), 681-685.

121. Herdering, C.; Reifschneider, O.; Wehe, C. A.; Sperling, M.; Karst, U., Ambient molecular imaging by laser ablation atmospheric pressure chemical ionization mass spectrometry. *Rapid Commun. Mass Spectrom.* **2013,** *27* (23), 2595-2600.

122. Shiea, J.; Huang, M.-Z.; Hsu, H.-J.; Lee, C.-Y.; Yuan, C.-H.; Beech, I.; Sunner, J., Electrospray-assisted laser desorption/ionization mass spectrometry for direct ambient analysis of solids. *Rapid Commun. Mass Spectrom.* **2005,** *19* (24), 3701-3704.

123. Vertes, A.; Nemes, P.; Shrestha, B.; Barton, A.; Chen, Z.; Li, Y., Molecular imaging by Mid-IR laser ablation mass spectrometry. *Appl. Phys. A: Mater. Sci. Process.* **2008,** *93* (4), 885-891.

124. Nemes, P.; Vertes, A., Atmospheric-pressure Molecular Imaging of Biological Tissues and Biofilms by LAESI Mass Spectrometry. *J. Vis. Exp.* **2010,** (43), e2097.

125. Laiko, V. V.; Baldwin, M. A.; Burlingame, A. L., Atmospheric Pressure Matrix-Assisted Laser Desorption/Ionization Mass Spectrometry. *Anal. Chem.* **2000,** *72* (4), 652-657.

126. Sampson, J. S.; Hawkridge, A. M.; Muddiman, D. C., Generation and Detection of Multiply-Charged Peptides and Proteins by Matrix-Assisted Laser Desorption Electrospray Ionization (MALDESI) Fourier Transform Ion Cyclotron Resonance Mass Spectrometry. *J. Am. Soc. Mass. Spectrom.* **2006,** *17* (12), 1712-1716.

127. Dill, A. L.; Eberlin, L. S.; Ifa, D. R.; Cooks, R. G., Perspectives in imaging using mass spectrometry. *Chem. Commun.* **2011,** *47* (10), 2741-2746.

128. Seeley, E. H.; Schwamborn, K.; Caprioli, R. M., Imaging of Intact Tissue Sections: Moving beyond the Microscope. *J. Biol. Chem.* **2011,** *286* (29), 25459-25466.

129. Chaurand, P., Imaging mass spectrometry of thin tissue sections: A decade of collective efforts. *J. Proteomics* **2012,** *75* (16), 4883-4892.

130. Chughtai, K.; Jiang, L.; Post, H.; Winnard, P., Jr.; Greenwood, T.; Raman, V.; Bhujwalla, Z.; Heeren, R. A.; Glunde, K., Mass Spectrometric Imaging of Red Fluorescent Protein in Breast Tumor Xenografts. *J. Am. Soc. Mass. Spectrom.* **2013,** *24* (5), 711-717.

131. Altelaar, A. F. M.; Taban, I. M.; McDonnell, L. A.; Verhaert, P. D. E. M.; de Lange, R. P. J.; Adan, R. A. H.; Mooi, W. J.; Heeren, R. M. A.; Piersma, S. R., High-resolution MALDI imaging mass spectrometry allows localization of peptide distributions at cellular length scales in pituitary tissue sections. *Int. J. Mass spectrom.* **2007,** *260* (2–3), 203-211.

132. Jackson, S. N.; Ugarov, M.; Egan, T.; Post, J. D.; Langlais, D.; Albert Schultz, J.; Woods, A. S., MALDI-ion mobility-TOFMS imaging of lipids in rat brain tissue. *J. Mass Spectrom.* **2007,** *42* (8), 1093-1098.

133. Dill, A. L.; Ifa, D. R.; Manicke, N. E.; Ouyang, Z.; Cooks, R. G., Mass spectrometric imaging of lipids using desorption electrospray ionization. *J. Chromatogr. B* **2009,** *877* (26), 2883-2889.

134. Murphy, R. C.; Hankin, J. A.; Barkley, R. M., Imaging of lipid species by MALDI mass spectrometry. *J. Lipid Res.* **2009,** *50* (Supplement), S317-S322.

135. Wiseman, J. M.; Ifa, D. R.; Zhu, Y.; Kissinger, C. B.; Manicke, N. E.; Kissinger, P. T.; Cooks, R. G., Desorption electrospray ionization mass spectrometry: Imaging drugs and metabolites in tissues. *Proc. Natl. Acad. Sci.* **2008,** *105* (47), 18120-18125.

136. Vismeh, R.; Waldon, D. J.; Teffera, Y.; Zhao, Z., Localization and Quantification of Drugs in Animal Tissues by Use of Desorption Electrospray Ionization Mass Spectrometry Imaging. *Anal. Chem.* **2012,** *84* (12), 5439-5445.

137. Lietz, C. B.; Gemperline, E.; Li, L., Qualitative and quantitative mass spectrometry imaging of drugs and metabolites. *Advanced Drug Delivery Reviews* **2013,** *65* (8), 1074-1085.

138. Ellis, S. R.; Wu, C.; Deeley, J. M.; Zhu, X.; Truscott, R. J. W.; Panhuis, M. i. h.; Cooks, R. G.; Mitchell, T. W.; Blanksby, S. J., Imaging of Human Lens Lipids by Desorption Electrospray Ionization Mass Spectrometry. *J. Am. Soc. Mass. Spectrom.* **2010,** *21* (12), 2095-2104.

139. Wu, C.; Ifa, D. R.; Manicke, N. E.; Cooks, R. G., Molecular imaging of adrenal gland by desorption electrospray ionization mass spectrometry. *Analyst* **2010,** *135* (1), 28-32.

140. Berry, K. A. Z.; Hankin, J. A.; Barkley, R. M.; Spraggins, J. M.; Caprioli, R. M.; Murphy, R. C., MALDI Imaging of Lipid Biochemistry in Tissues by Mass Spectrometry. *Chem. Rev.* **2011,** *111*, 6491-6512.

141. Siegel, G. J.; Agranoff, B. W., *Basic Neurochemistry: Molecular, Cellular, and Medical Aspects*. Lippincott Williams & Wilkins: 1999.

142. Murphy, E. J.; Schapiro, M. B.; Rapoport, S. I.; Shetty, H. U., Phospholipid composition and levels are altered in down syndrome brain. *Brain Res.* **2000,** *867* (1–2), 9-18.

143. Han, X.; Rozen, S.; Boyle, S. H.; Hellegers, C.; Cheng, H.; Burke, J. R.; Welsh-Bohmer, K. A.; Doraiswamy, P. M.; Kaddurah-Daouk, R., Metabolomics in Early Alzheimer's Disease: Identification of Altered Plasma Sphingolipidome Using Shotgun Lipidomics. *PLoS ONE* **2011,** *6* (7), e21643.

144. Sparvero, L. J.; Amoscato, A. A.; Kochanek, P. M.; Pitt, B. R.; Kagan, V. E.; Bayır, H., Mass-spectrometry based oxidative lipidomics and lipid imaging: applications in traumatic brain injury. *J. Neurochem.* **2010,** *115* (6), 1322-1336.

145. Ji, J.; Kline, A. E.; Amoscato, A.; Samhan-Arias, A. K.; Sparvero, L. J.; Tyurin, V. A.; Tyurina, Y. Y.; Fink, B.; Manole, M. D.; Puccio, A. M.; Okonkwo, D. O.; Cheng, J. P.; Alexander, H.; Clark, R. S. B.; Kochanek, P. M.; Wipf, P.; Kagan, V. E.; Bayir, H., Lipidomics identifies cardiolipin oxidation as a mitochondrial target for redox therapy of brain injury. *Nature Neuroschience* **2012,** *15* (10), 1407-1413.

146. Chughtai, K.; Jiang, L.; Greenwood, T. R.; Glunde, K.; Heeren, R. M. A., Mass spectrometry images acylcarnitines, phosphatidylcholines, and sphingomyelin in MDA-MB-231 breast tumor models. *J. Lipid Res.* **2013,** *54* (2), 333-344.

147. Schiller, J.; Süß, R.; Arnhold, J.; Fuchs, B.; Leßig, J.; Müller, M.; Petković, M.; Spalteholz, H.; Zschörnig, O.; Arnold, K., Matrix-assisted laser desorption and ionization time-of-flight (MALDI-TOF) mass spectrometry in lipid and phospholipid research. *Prog. Lipid Res.* **2004,** *43* (5), 449-488.

148. Jackson, S. N.; Wang, H.-Y. J.; Woods, A. S., Direct Profiling of Lipid Distribution in Brain Tissue Using MALDI-TOFMS. *Anal. Chem.* **2005,** *77* (14), 4523-4527.

149. Woods, A.; Jackson, S., Brain tissue lipidomics: Direct probing using matrix-assisted laser desorption/ionization mass spectrometry. *AAPS J* **2006,** *8* (2), E391-E395.

150. Jackson, S. N.; Wang, H.-Y. J.; Woods, A. S., In Situ Structural Characterization of Glycerophospholipids and Sulfatides in Brain Tissue Using MALDI-MS/MS. *J. Am. Soc. Mass. Spectrom.* **2007,** *18* (1), 17-26.

151. Jackson, S. N.; Woods, A. S., Direct profiling of tissue lipids by MALDI-TOFMS. *J. Chromatogr. B* **2009,** *877* (26), 2822-2829.

152. Chen, R.; Hui, L.; Sturm, R. M.; Li, L., Three Dimensional Mapping of Neuropeptides and Lipids in Crustacean Brain by Mass Spectral Imaging. *J. Am. Soc. Mass. Spectrom.* **2009,** *20* (6), 1068-1077.

153. Stoeckli, M.; Staab, D.; Schweitzer, A., Compound and metabolite distribution measured by MALDI mass spectrometric imaging in whole-body tissue sections. *Int. J. Mass spectrom.* **2007,** *260* (2–3), 195-202.

154. Seeley, E. H.; Oppenheimer, S. R.; Mi, D.; Chaurand, P.; Caprioli, R. M., Enhancement of Protein Sensitivity for MALDI Imaging Mass Spectrometry After Chemical Treatment of Tissue Sections. *J. Am. Soc. Mass. Spectrom.* **2008,** *19* (8), 1069-1077.

155. Angel, P. M.; Spraggins, J. M.; Baldwin, H. S.; Caprioli, R., Enhanced Sensitivity for High Spatial Resolution Lipid Analysis by Negative Ion Mode Matrix Assisted Laser Desorption Ionization Imaging Mass Spectrometry. *Anal. Chem.* **2012,** *84* (3), 1557-1564.

156. Girod, M.; Shi, Y.; Cheng, J.-X.; Cooks, R. G., Mapping Lipid Alterations in Traumatically Injured Rat Spinal Cord by Desorption Electrospray Ionization Imaging Mass Spectrometry. *Anal. Chem.* **2011,** *83* (1), 207-215.

157. Thomas, A.; Charbonneau, J. L.; Fournaise, E.; Chaurand, P., Sublimation of New Matrix Candidates for High Spatial Resolution Imaging Mass Spectrometry of Lipids: Enhanced Information in Both Positive and Negative Polarities after 1,5-Diaminonapthalene Deposition. *Anal. Chem.* **2012,** *84* (4), 2048-2054.

158. Vermillion-Salsbury, R. L.; Hercules, D. M., 9-Aminoacridine as a matrix for negative mode matrix-assisted laser desorption/ionization. *Rapid Commun. Mass Spectrom.* **2002,** *16* (16), 1575-1581.

159. Cheng, H.; Sun, G.; Yang, K.; Gross, R. W.; Han, X., Selective desorption/ionization of sulfatides by MALDI-MS facilitated using 9-aminoacridine as matrix. *J. Lipid Res.* **2010,** *51* (6), 1599-1609.

160. Kim, Y.; Shanta, S. R.; Zhou, L.-H.; Kim, K. P., Mass spectrometry based cellular phosphoinositides profiling and phospholipid analysis: A brief review. *Exp. Mol. Med.* **2010,** *42*, 1-11.

161. Liu, Y.; Chen, Y.; Momin, A.; Shaner, R.; Wang, E.; Bowen, N. J.; Matyunina, L. V.; Walker, L. D.; McDonald, J. F.; Sullards, M. C.; Merrill Jr, A. H., Elevation of sulfatides in ovarian cancer: An integrated transcriptomic and lipidomic analysis including tissue-imaging mass spectrometry. *Mol. Cancer* **2010,** *9* (186).

162. Adibhatla, R. M.; Hatcher, J. F.; Dempsey, R. J., Lipids and lipidomics in brain injury and diseases. *AAPS J* **2006,** *8* (2), E314-E321.

163. Giza, C. C.; Kutcher, J. S.; Ashwal, S.; Barth, J.; Getchius, T. S. D.; Gioia, G. A.; Gronseth, G. S.; Guskiewicz, K.; Mandel, S.; Manley, G.; McKeag, D. B.; Thurman, D. J.; Zafonte, R., Summary of evidence-based guideline update: Evaluation and management of concussion in sports: Report of the Guideline Development Subcommittee of the American Academy of Neurology. *Neurology* **2013,** *80* (24), 2250-2257.

164. Hall, E. D.; Vaishnav, R. A.; Mustafa, A. G., Antioxidant therapies for traumatic brain injury. *Neurotherapeutics* **2010,** *7* (1), 51-61.

165. Wang, H.-Y. J.; Liu, C. B.; Wu, H.-W., A simple desalting method for direct MALDI mass spectrometry profiling of tissue lipids. *J. Lipid Res.* **2011,** *52* (4), 840-849.

166. Wang, H.-Y. J.; Liu, C. B.; Wu, H.-W.; Kuo, J. S., Direct profiling of phospholipids and lysophospholipids in rat brain sections after ischemic stroke. *Rapid Commun. Mass Spectrom.* **2010,** *24* (14), 2057-2064.

167. Koizumi, S.; Yamamoto, S.; Hayasaka, T.; Konishi, Y.; Yamaguchi-Okada, M.; Goto-Inoue, N.; Sugiura, Y.; Setou, M.; Namba, H., Imaging mass spectrometry revealed the production of lyso-phosphatidylcholine in the injured ischemic rat brain. *Neuroscience* **2010,** *168* (1), 219-225.

168. Hankin, J.; Farias, S.; Barkley, R.; Heidenreich, K.; Frey, L.; Hamazaki, K.; Kim, H.-Y.; Murphy, R., MALDI Mass Spectrometric Imaging of Lipids in Rat Brain Injury Models. *J. Am. Soc. Mass. Spectrom.* **2011,** *22* (6), 1014-1021.

169. Bayir, H.; Tyurin, V. A.; Tyurina, Y. Y.; Viner, R.; Ritov, V.; Amoscato, A. A.; Zhao, Q.; Zhang, X. J.; Janesko-Feldman, K. L.; Alexander, H.; Basova, L. V.; Clark, R. S. B.; Kochanek, P. M.; Kagan, V. E., Selective early cardiolipin peroxidation after traumatic brain injury: an oxidative lipidomics analysis. *Ann. Neurol.* **2007,** *62* (2), 154-169.

170. Whitehead, S. N.; Chan, K. H. N.; Gangaraju, S.; Slinn, J.; Li, J.; Hou, S. T., Imaging Mass Spectrometry Detection of Gangliosides Species in the Mouse Brain following Transient Focal Cerebral Ischemia and Long-Term Recovery. *PLoS ONE* **2011,** *6* (6), e20808.

171. Parry, R. M.; Galhena, A. S.; Gamage, C. M.; Bennett, R. V.; Wang, M. D.; Fernandez, F. M., OmniSpect: An Open Matlab-based Tool for Visualization and Analysis of Matrix-assisted Laser Desorption/Ionization and Desorption Electrospray Ionization Mass Spectrometry Images. *J. Am. Soc. Mass Spectrom.* **2013,** (24), 646-649.

172. Bennett, R. V.; Gamage, C. M.; Galhena, A. S.; Fernández, F. M., Contrast-Enhanced Differential Mobility-Desorption Electrospray Ionization-Mass Spectrometry Imaging of Biological Tissues. *Anal. Chem.* **2014,** *86* (8), 3756-3763.

173. Jain, A. K., *Fundamentals of Digital Image Processing*. Prentice Hall International, Inc: Englewood Cliffs, NJ, 1989.

174. Keller, B. O.; Sui, J.; Young, A. B.; Whittal, R. M., Interferences and contaminants encountered in modern mass spectrometry. *Anal. Chim. Acta* **2008,** *627* (1), 71-81.

175. Heeren, R. M. A.; Kükrer-Kaletaş, B.; Taban, I. M.; MacAleese, L.; McDonnell, L. A., Quality of surface: The influence of sample preparation on MS-based biomolecular tissue imaging with MALDI-MS and (ME-)SIMS. *Appl. Surf. Sci.* **2008,** *255* (4), 1289-1297.

176. Chavko, M.; Nemoto, E.; Melick, J., Regional lipid composition in the rat brain. *Mol. Chem. Neuropathol.* **1993,** *18* (1-2), 123-131.

177. Mendes Arent, A.; #xe9; Souza, L. F. d.; Walz, R.; Dafre, A. L., Perspectives on Molecular Biomarkers of Oxidative Stress and Antioxidant Strategies in Traumatic Brain Injury. *BioMed Research International* **2014,** *2014*, 18.

178. Pleasant, J. M.; Carlson, S. W.; Mao, H.; Scheff, S. W.; Yang, K. H.; Saatman, K. E., Rate of Neurodegeneration in the Mouse Controlled Cortical Impact Model Is Influenced by Impactor Tip Shape: Implications for Mechanistic and Therapeutic Studies. *J. Neurotrauma* **2011,** *28* (11), 2245-2262.

179. Wang, H.-Y.; Wu, H.-W.; Tsai, P.-J.; Liu, C., MALDI-mass spectrometry imaging of desalted rat brain sections reveals ischemia-mediated changes of lipids. *Anal. Bioanal. Chem.* **2012,** *404* (1), 113-124.

180. Kertesz, V.; Van Berkel, G. J.; Vavrek, M.; Koeplinger, K. A.; Schneider, B. B.; Covey, T. R., Comparison of Drug Distribution Images from Whole-Body Thin Tissue Sections Obtained Using Desorption Electrospray Ionization Tandem Mass Spectrometry and Autoradiography. *Anal. Chem.* **2008,** *80* (13), 5168-5177.

181. Manicke, N. E.; Nefliu, M.; Wu, C.; Woods, J. W.; Reiser, V.; Hendrickson, R. C.; Cooks, R. G., Imaging of Lipids in Atheroma by Desorption Electrospray Ionization Mass Spectrometry. *Anal. Chem.* **2009,** *81* (21), 8702-8707.

182. Valentine, S. J.; Kulchania, M.; Barnes, C. A. S.; Clemmer, D. E., Multidimensional separations of complex peptide mixtures: a combined high-performance liquid chromatography/ion mobility/time-of-flight mass spectrometry approach. *Int. J. Mass spectrom.* **2001,** *212* (1–3), 97-109.

183. Giles, K.; Pringle, S. D.; Worthington, K. R.; Little, D.; Wildgoose, J. L.; Bateman, R. H., Applications of a travelling wave-based radio-frequency-only stacked ring ion guide. *Rapid Commun. Mass Spectrom.* **2004,** *18* (20), 2401-2414.

184. Stauber, J.; MacAleese, L.; Franck, J.; Claude, E.; Snel, M.; Kaletas, B. K.; Wiel, I. M. V. D.; Wisztorski, M.; Fournier, I.; Heeren, R. M. A., On-Tissue Protein Identification and Imaging by MALDI-Ion Mobility Mass Spectrometry. *J. Am. Soc. Mass. Spectrom.* **2010,** *21* (3), 338-347.

185. Djidja, M.-C.; Claude, E.; Snel, M. F.; Scriven, P.; Francese, S.; Carolan, V.; Clench, M. R., MALDI-Ion Mobility Separation-Mass Spectrometry Imaging of Glucose-Regulated Protein 78 kDa (Grp78) in Human Formalin-Fixed, Paraffin-Embedded Pancreatic Adenocarcinoma Tissue Sections. *J. Proteome Res.* **2009,** *8* (10), 4876-4884.

186. McLean, J. A.; Ridenour, W. B.; Caprioli, R. M., Profiling and imaging of tissues by imaging ion mobility-mass spectrometry. *J. Mass Spectrom.* **2007,** *42* (8), 1099-1105.

187. Trim, P. J.; Henson, C. M.; Avery, J. L.; McEwen, A.; Snel, M. F.; Claude, E.; Marshall, P. S.; West, A.; Princivalle, A. P.; Clench, M. R., Matrix-Assisted Laser Desorption/Ionization-Ion Mobility Separation-Mass Spectrometry Imaging of Vinblastine in Whole Body Tissue Sections. *Anal. Chem.* **2008,** *80* (22), 8628-8634.

188. Buryakov, I. A.; Krylov, E. V.; Nazarov, E. G.; Rasulev, U. K., A new method of separation of multi-atomic ions by mobility at atmospheric pressure using a high-frequency amplitude-asymmetric strong electric field. *Int. J. Mass Spectrom. Ion Processes* **1993,** *128* (3), 143-148.

189. Purves, R. W.; Guevremont, R.; Day, S.; Pipich, C. W.; Matyjaszczyk, M. S., Mass spectrometric characterization of a high-field asymmetric waveform ion mobility spectrometer. *Rev. Sci. Instrum.* **1998,** *69* (12), 4094-4105.

190. Guevremont, R., High-field asymmetric waveform ion mobility spectrometry: A new tool for mass spectrometry. *J. Chromatogr. A* **2004,** *1058* (1–2), 3-19.

191. Krylov, E. V.; Nazarov, E. G.; Miller, R. A., Differential mobility spectrometer: Model of operation. *Int. J. Mass spectrom.* **2007,** *266* (1–3), 76-85.

192. Kanu, A. B.; Dwivedi, P.; Tam, M.; Matz, L.; Hill, H. H., Ion mobility–mass spectrometry. *J. Mass Spectrom.* **2008,** *43* (1), 1-22.

193. Tang, K.; Li, F.; Shvartsburg, A. A.; Strittmatter, E. F.; Smith, R. D., Two-Dimensional Gas-Phase Separations Coupled to Mass Spectrometry for Analysis of Complex Mixtures. *Anal. Chem.* **2005,** *77* (19), 6381-6388.

194. Krylov, E. V.; Nazarov, E. G., Electric field dependence of the ion mobility. *Int. J. Mass spectrom.* **2009,** *285* (3), 149-156.

195. Schneider, B.; Covey, T.; Coy, S.; Krylov, E.; Nazarov, E., Control of chemical effects in the separation process of a differential mobility mass spectrometer system. *Eur. J. Mass Spectrom.* **2010,** *16* (1), 57-71.

196. Shvartsburg, A. A.; Danielson, W. F.; Smith, R. D., High-Resolution Differential Ion Mobility Separations Using Helium-Rich Gases. *Anal. Chem.* **2010,** *82* (6), 2456-2462.

197. Shvartsburg, A.; Isaac, G.; Leveque, N.; Smith, R.; Metz, T., Separation and Classification of Lipids Using Differential Ion Mobility Spectrometry. *J. Am. Soc. Mass. Spectrom.* **2011,** *22* (7), 1146-1155.

198. Shvartsburg, A.; Ibrahim, Y.; Smith, R., Differential Ion Mobility Separations in up to 100 % Helium Using Microchips. *J. Am. Soc. Mass. Spectrom.* **2014,** *25* (3), 480-489.

199. Schneider, B. B.; Covey, T. R.; Coy, S. L.; Krylov, E. V.; Nazarov, E. G., Chemical Effects in the Separation Process of a Differential Mobility/Mass Spectrometer System. *Anal. Chem.* **2010,** *82* (5), 1867-1880.

200. Schneider, B.; Nazarov, E.; Covey, T., Peak capacity in differential mobility spectrometry: effects of transport gas and gas modifiers. *Int. J. Ion Mobil. Spec.* **2012,** *15* (3), 141-150.

201. Venne, K.; Bonneil, E.; Eng, K.; Thibault, P., Improvement in Peptide Detection for Proteomics Analyses Using NanoLC−MS and High-Field Asymmetry Waveform Ion Mobility Mass Spectrometry. *Anal. Chem.* **2005,** *77* (7), 2176-2186.

202. Galhena, A. S.; Harris, G. A.; Kwasnik, M.; Fernández, F. M., Enhanced Direct Ambient Analysis by Differential Mobility-Filtered Desorption Electrospray Ionization-Mass Spectrometry. *Anal. Chem.* **2010,** *82* (22), 9159-9163.

203. Rorrer III, L. C.; Yost, R. A., Solvent vapor effects on planar high-field asymmetric waveform ion mobility spectrometry. *Int. J. Mass spectrom.* **2011,** *300* (2–3), 173-181.

204. Kolakowski, B. M.; Mester, Z., Review of applications of high-field asymmetric waveform ion mobility spectrometry (FAIMS) and differential mobility spectrometry (DMS). *Analyst* **2007,** *132* (9), 842-864.

205. Barnett, D. A.; Purves, R. W.; Guevremont, R., Isotope separation using high–field asymmetric waveform ion mobility spectrometry. *Nucl. Instrum. Methods Phys. Res., Sect. A* **2000,** *450* (1), 179-185.

206. Nazarov, E. G.; Miller, R. A.; Eiceman, G. A.; Stone, J. A., Miniature Differential Mobility Spectrometry Using Atmospheric Pressure Photoionization. *Anal. Chem.* **2006,** *78* (13), 4553-4563.

207. Fink, P., Ecological functions of volatile organic compounds in aquatic systems. *Mar. Freshwater Behav. Physiol.* **2007,** *40* (3), 155-168.

208. Hay, M. E.; Rasher, D. B., Personal Communications, unpublished data. e-mail, 2013.

209. Cummins, S. F.; Bowie, J. H., Pheromones, attractants and other chemical cues of aquatic organisms and amphibians. *Nat. Prod. Rep.* **2012,** *29* (6), 642-658.

210. Lane, A. L.; Nyadong, L.; Galhena, A. S.; Shearer, T. L.; Stout, E. P.; Parry, R. M.; Kwasnik, M.; Wang, M. D.; Hay, M. E.; Fernandez, F. M.; Kubanek, J., Desorption electrospray ionization mass spectrometry reveals surface-mediated antifungal chemical defense of a tropical seaweed. *Proc. Natl. Acad. Sci.* **2009,** *106* (18), 7314-7319.

211. Andras, T.; Alexander, T.; Gahlena, A.; Parry, R. M.; Fernandez, F.; Kubanek, J.; Wang, M.; Hay, M., Seaweed Allelopathy Against Coral: Surface Distribution of a Seaweed Secondary Metabolite by Imaging Mass Spectrometry. *J. Chem. Ecol.* **2012,** *38* (10), 1203-1214.

212. Roetering, S.; Nazarov, E.; Borsdorf, H.; Weickhardt, C., Effect of dopants on the analysis of pesticides by means of differential mobility spectrometry with atmospheric pressure photoionization. *Int. J. Ion Mobil. Spec.* **2010,** *13* (2), 47-54.

213. Krylov, E. V., A method of reducing diffusion losses in a drift spectrometer. *Tech. Phys.* **1999,** *44* (1), 113-116.

214. Schneider, B. B.; Covey, T. R.; Coy, S. L.; Krylov, E. V.; Nazarov, E. G., Planar differential mobility spectrometer as a pre-filter for atmospheric pressure ionization mass spectrometry. *Int. J. Mass spectrom.* **2010,** *298* (1–3), 45-54.

215. Miller, R. A.; Eiceman, G. A.; Nazarov, E. G.; King, A. T., A novel micromachined high-field asymmetric waveform-ion mobility spectrometer. *Sens. Actuators, B* **2000,** *67* (3), 300-306.

216. Visintin, I.; Feng, Z.; Longton, G.; Ward, D. C.; Alvero, A. B.; Lai, Y.; Tenthorey, J.; Leiser, A.; Flores-Saaib, R.; Yu, H.; Azori, M.; Rutherford, T.; Schwartz, P. E.; Mor, G., Diagnostic Markers for Early Detection of Ovarian Cancer. *Clinical Cancer Research* **2008,** *14* (4), 1065-1072.

217. Cooks, R. G.; Manicke, N. E.; Dill, A. L.; Ifa, D. R.; Eberlin, L. S.; Costa, A. B.; Wang, H.; Huang, G.; Ouyang, Z., New ionization methods and miniature mass spectrometers for biomedicine: DESI imaging for cancer diagnostics and paper spray ionization for therapeutic drug monitoring. *Faraday Discuss.* **2011,** *149* (0), 247-267.

218. Lintonen, T. P. I.; Baker, P. R. S.; Suoniemi, M.; Ubhi, B. K.; Koistinen, K. M.; Duchoslav, E.; Campbell, J. L.; Ekroos, K., Differential Mobility Spectrometry-Driven Shotgun Lipidomics. *Anal. Chem.* **2014,** *86* (19), 9662-9669.

219. Wiseman, J. M.; Ifa, D. R.; Venter, A.; Cooks, R. G., Ambient molecular imaging by desorption electrospray ionization mass spectrometry. *Nat. Protocols* **2008,** *3* (3), 517-524.

220. Van Berkel, G. J.; Ford, M. J.; Deibel, M. A., Thin-Layer Chromatography and Mass Spectrometry Coupled Using Desorption Electrospray Ionization. *Anal. Chem.* **2005,** *77* (5), 1207-1215.

221. Harada, K., Formation of Amino-acids by Thermal Decomposition of Formamide--Oligomerization of Hydrogen Cyanide. *Nature* **1967,** *214* (5087), 479-480.

222. Bredereck, H.; Effenberger, F.; Simchen, G., Reaktionsfähige Säureamid-Dimethylsulfat-Komplexe. *Angew. Chem.* **1961,** *73* (14), 493-493.

223. Saladino, R.; Crestini, C.; Costanzo, G.; Negri, R.; Di Mauro, E., A possible prebiotic synthesis of purine, adenine, cytosine, and 4(3H)-pyrimidinone from formamide: implications for the origin of life. *Biorg. Med. Chem.* **2001,** *9* (5), 1249-1253.

224. Miyakawa, S.; James Cleaves, H.; Miller, S., The Cold Origin of Life: A. Implications Based On The Hydrolytic Stabilities Of Hydrogen Cyanide And Formamide. *Origins Life Evol. Biosphere* **2002,** *32* (3), 195-208.

225. Tian, F.; Kasting, J. F.; Zahnle, K., Revisiting HCN formation in Earth's early atmosphere. *Earth. Planet. Sci. Lett.* **2011,** *308* (3–4), 417-423.

226. Miyakawa, S.; Cleaves, H. J.; Miller, S. L., The cold origin of life: A. Implications based on the hydrolytic stabilities of hydrogen cyanide and formamide. *Orig. Life Evol. Biosph.* **2002,** *32* (3), 195-208.

227. Hudson, J. S.; Eberle, J. F.; Vachhani, R. H.; Rogers, L. C.; Wade, J. H.; Krishnamurthy, R.; Springsteen, G., A Unified Mechanism for Abiotic Adenine and Purine Synthesis in Formamide. *Angew. Chem. Int. Ed.* **2012,** *51* (21), 5134-5137.

228. Saladino, R.; Claudia, C.; Giovanna, C.; Ernesto, D., Advances in the Prebiotic Synthesis of Nucleic Acids Bases: Implications for the Origin of Life. *Curr. Org. Chem.* **2004,** *8* (15), 1425-1443.

229. Barks , H. L.; Buckley , R.; Grieves, G. A.; Di Mauro, E.; Hud, N. V.; Orlando, T. M., Guanine, Adenine, and Hypoxanthine Production in UV-Irradiated Formamide Solutions: Relaxation of the Requirements for Prebiotic Purine Nucleobase Formation. *ChemBioChem* **2010,** *11* (9), 1240-1243.

230. Saladino, R.; Crestini, C.; Ciciriello, F.; Costanzo, G.; Di Mauro, E., Formamide Chemistry and the Origin of Informational Polymers. *Chemistry & Biodiversity* **2007,** *4* (4), 694-720.

231. Saladino, R.; Crestini, C.; Pino, S.; Costanzo, G.; Di Mauro, E., Formamide and the origin of life. *Phys. Life. Rev.* **2012,** *9* (1), 84-104.

232. Saladino, R.; Crestini, C.; Cossetti, C.; Di Mauro, E.; Deamer, D., Catalytic effects of Murchison Material: Prebiotic Synthesis and Degradation of RNA Precursors. *Origins of Life and Evolution of Biospheres* **2011,** *41* (5), 437-451.

233. Hazen, R. M.; Papineau, D.; Bleeker, W.; Downs, R. T.; Ferry, J. M.; McCoy, T. J.; Sverjensky, D. A.; Yang, H., Mineral evolution. *Am. Mineral.* **2008,** *93* (11-12), 1693-1720.

234. Bada, J. L., How life began on Earth: a status report. *Earth. Planet. Sci. Lett.* **2004,** *226* (1–2), 1-15.

235. Carpenter, D.; Taylor, M., *Adv. X-Ray Anal.* **1991,** *34*, 217-223.

236. Kotula, P. G.; Keenan, M. R.; Michael, J. R., Automated Analysis of SEM X-Ray Spectral Images: A Powerful New Microanalysis Tool. *Microsc. Microanal.* **2003,** *9* (01), 1-17.

237. Downs, R. T. In *The RRUFF Project: an integrated study of the chemistry, crystallography, Raman and infrared spectroscopy of minerals.*, 19th General Meeting of the International Mineralogical Association, Kobe, Japan, Kobe, Japan, 2006; pp O13-013.

238. Qiu, B.; Luo, H., Desorption electrospray ionization mass spectrometry of DNA nucleobases: implications for a liquid film model. *J. Mass Spectrom.* **2009,** *44* (5), 772-779.

239. Nemes, P.; Barton, A. A.; Li, Y.; Vertes, A., Ambient Molecular Imaging and Depth Profiling of Live Tissue by Infrared Laser Ablation Electrospray Ionization Mass Spectrometry. *Anal. Chem.* **2008,** *80* (12), 4575-4582.

240. Wu, C.; Dill, A. L.; Eberlin, L. S.; Cooks, R. G.; Ifa, D. R., Mass spectrometry imaging under ambient conditions. *Mass Spectrom. Rev.* **2013,** *32* (3), 218-243.

241. Hiraoka, K.; Nishidate, K.; Mori, K.; Asakawa, D.; Suzuki, S., Development of probe electrospray using a solid needle. *Rapid Commun. Mass Spectrom.* **2007,** *21* (18), 3139-3144.

242. Chen, L. C.; Yoshimura, K.; Yu, Z.; Iwata, R.; Ito, H.; Suzuki, H.; Mori, K.; Ariyada, O.; Takeda, S.; Kubota, T.; Hiraoka, K., Ambient imaging mass spectrometry by electrospray ionization using solid needle as sampling probe. *J. Mass Spectrom.* **2009,** *44* (10), 1469-1477.

243. Seeley, E. H.; Caprioli, R. M., 3D Imaging by Mass Spectrometry: A New Frontier. *Anal. Chem.* **2012,** *84* (5), 2105-2110.

244. Crecelius, A. C.; Cornett, D. S.; Caprioli, R. M.; Williams, B.; Dawant, B. M.; Bodenheimer, B., Three-Dimensional Visualization of Protein Expression in Mouse Brain Structures Using Imaging Mass Spectrometry. *J. Am. Soc. Mass Spectrom.* **2005,** *16*, 1093–1099.

245. Fletcher, J. S.; Lockyer, N. P.; Vaidyanathan, S.; Vickerman, J. C., TOF-SIMS 3D Biomolecular Imaging of Xenopus laevis Oocytes Using Buckminsterfullerene (C60) Primary Ions. *Anal. Chem.* **2007,** *79* (6), 2199-2206.

246. Nemes, P.; Barton, A. A.; Vertes, A., Three-Dimensional Imaging of Metabolites in Tissues under Ambient Conditions by Laser Ablation Electrospray Ionization Mass Spectrometry. *Anal. Chem.* **2009,** *81* (16), 6668-6675.

247. Cody, R. B., Observation of Molecular Ions and Analysis of Nonpolar Compounds with the Direct Analysis in Real Time Ion Source. *Anal. Chem.* **2009,** *81* (3), 1101-1107.

248. Harris, G. A.; Fernández, F. M., Simulations and Experimental Investigation of Atmospheric Transport in an Ambient Metastable-Induced Chemical Ionization Source. *Anal. Chem.* **2009,** *81* (1), 322-329.

249. Nicol, G.; Sunner, J.; Kebarle, P., Kinetics and thermodynamics of protonation reactions: H3O+ (H2O)h + B = BH+ (H2O)b + (h − b + 1) H2O, where B is a nitrogen, oxygen or carbon base. *Int. J. Mass Spectrom. Ion Processes* **1988,** *84* (1–2), 135-155.

250. Sunner, J.; Nicol, G.; Kebarle, P., Factors determining relative sensitivity of analytes in positive mode atmospheric pressure ionization mass spectrometry. *Anal. Chem.* **1988,** *60* (13), 1300-1307.

251. Hiraoka, K.; Fujimaki, S.; Kambara, S.; Furuya, H.; Okazaki, S., Atmospheric-pressure Penning ionization mass spectrometry. *Rapid Commun. Mass Spectrom.* **2004,** *18* (19), 2323-2330.

252. Harris, G. A.; Falcone, C. E.; Fernández, F. M., Sensitivity "Hot Spots" in the Direct Analysis in Real Time Mass Spectrometry of Nerve Agent Simulants. *J. Am. Soc. Mass. Spectrom.* **2012,** *23* (1), 153-161.

253. *CRC Handbook of Chemistry and Physics*. 62nd ed.; CRC Press, Inc.: Boca Raton, FL, 1981.

254. Chen, H.; Venter, A.; Cooks, R. G., Extractive electrospray ionization for direct analysis of undiluted urine, milk and other complex mixtures without sample preparation. *Chem. Commun.* **2006,** (19), 2042-2044.

255. Chen, H.; Yang, S.; Wortmann, A.; Zenobi, R., Neutral Desorption Sampling of Living Objects for Rapid Analysis by Extractive Electrospray Ionization Mass Spectrometry. *Angew. Chem.* **2007,** *119* (40), 7735-7738.

256. Weber, A. L., Sugar-Driven Prebiotic Synthesis of 3,5(6)-Dimethylpyrazin-2-one: A Possible Nucleobase of a Primitive Replication Process. *Origins of Life and Evolution of Biospheres* **2008,** *38* (4), 279-292.

257. F.Poole, C.; Poole, S. K., Instrumental Thin-Layer Chromatography. *Anal. Chem.* **1994,** *66* (1), 27A-37A.

258. Sherma, J., Planar Chromatography. *Anal. Chem.* **1998,** *70* (12), 7-26.

259. Busch, K. L., Mass spectrometric detection for thin-layer chromatographic separations. *TrAC, Trends Anal. Chem.* **1992,** *11* (9), 314-324.

260. Unger, S. E.; Vincze, A.; Cooks, R. G.; Chrisman, R.; Rothman, L. D., Identification of quaternary alkaloids in mushroom by chromatography/secondary ion mass spectrometry. *Anal. Chem.* **1981,** *53* (7), 976-981.

261. Cheng, S.-C.; Huang, M.-Z.; Shiea, J., Thin layer chromatography/mass spectrometry. *J. Chromatogr. A* **2011,** *1218* (19), 2700-2711.

262. Morlock, G.; Schwack, W., Coupling of planar chromatography to mass spectrometry. *TrAC, Trends Anal. Chem.* **2010,** *29* (10), 1157-1171.

263. Gusev, A. I.; Vasseur, O. J.; Proctor, A.; Sharkey, A. G.; Hercules, D. M., Imaging of thin-layer chromatograms using matrix-assisted laser desorption/ionization mass spectrometry. *Anal. Chem.* **1995,** *67* (24), 4565-4570.

264. Zhang, J.; Zhou, Z.; Yang, J.; Zhang, W.; Bai, Y.; Liu, H., Thin Layer Chromatography/Plasma Assisted Multiwavelength Laser Desorption Ionization Mass Spectrometry for Facile Separation and Selective Identification of Low Molecular Weight Compounds. *Anal. Chem.* **2011,** *84* (3), 1496-1503.

265. Eijkel, G. B.; Kükrer Kaletaş, B.; van der Wiel, I. M.; Kros, J. M.; Luider, T. M.; Heeren, R. M. A., Correlating MALDI and SIMS imaging mass spectrometric datasets of biological tissue surfaces. *Surf. Interface Anal.* **2009,** *41* (8), 675-685.

266. Alexandrov, T.; Chernyavsky, I.; Becker, M.; von Eggeling, F.; Nikolenko, S., Analysis and Interpretation of Imaging Mass Spectrometry Data by Clustering Mass-to-Charge Images According to Their Spatial Similarity. *Anal. Chem.* **2013**.

267. Huang, T.; Yang, G.; Tang, G., A fast two-dimensional median filtering algorithm. *Acoustics, Speech and Signal Processing, IEEE Transactions on* **1979,** *27* (1), 13-18.

268. Otsu, N., A Threshold Selection Method from Gray-Level Histograms. *Systems, Man and Cybernetics, IEEE Transactions on* **1979,** *9* (1), 62-66.

269. Gonzalez, R. C.; Woods, R. E., *Digital Image Processing*. 2nd ed.; Prentice Hall: Upper Sadle River, NJ, 2002.

270. Urban, J.; Afseth, N. K.; Štys, D., Fundamental definitions and confusions in mass spectrometry about mass assignment, centroiding and resolution. *TrAC, Trends Anal. Chem.* **2014,** *53* (0), 126.

271. Plumb, R. S.; Johnson, K. A.; Rainville, P.; Smith, B. W.; Wilson, I. D.; Castro-Perez, J. M.; Nicholson, J. K., UPLC/MSE; a new approach for generating molecular fragment information for biomarker structure elucidation. *Rapid Commun. Mass Spectrom.* **2006,** *20* (13), 1989-1994.

272. Kaddi, C.; Parry, R. M.; Wang, M. D. In *Hypergeometric Similarity Measure for Spatial Analysis in Tissue Imaging Mass Spectrometry*, Bioinformatics and Biomedicine (BIBM), 2011 IEEE International Conference on, 12-15 Nov. 2011; 2011; pp 604-607.

273. Kaddi, C. D.; Parry, R. M.; Wang, M. D., Multivariate hypergeometric similarity measure. *IEEE/ACM transactions on computational biology and bioinformatics / IEEE, ACM* **2013,** *10* (6), 1505-16.

VITA

RACHEL BENNETT STRYFFELER

Rachel Bennett Stryffeler was born in Tulsa, OK. She attended Booker T. Washington High School. Rachel pursued her undergraduate studies at The College of Wooster in Wooster, OH, where she earned her B.A. degree in Chemistry with Honors for her Independent Study Thesis in 2010. At Wooster, Rachel was a member of the Varsity Swim Team and she also studied abroad in the Fall of 2008 at the Universidad de Córdoba, Facultad de Filosofía y Letras. In August of 2010, Rachel moved to Atlanta, GA to pursue her PhD in Chemistry at Georgia Institute of Technology under the supervision of Facundo Fernández.